

**THE UNIVERSITY OF HULL**

**TLM MODELS OF DEFORMATION AND THEIR  
APPLICATION TO VITREOUS CHINA WARE DURING  
FIRING**

**being a Thesis submitted for the Degree of  
Doctor of Philosophy  
in the University of Hull**

**by**

**Helen Ruth Newton Bsc (Hons).**

**August 1994**

## ABSTRACT

In the sanitary ware industry the time associated with designing new geometries of ware is considerably long. This is due to the process of trial and error presently carried out to determine the mould shape necessary to produce the desired finished articles. Large articles such as wash basins, toilet pedestals and bidets may deform significantly under their own weight during firing. The method of support is limited as these articles are fired only once and in their glazed state, so that the ware stands on its unglazed surface as it passes through the kiln. Kiln cars carry the ware through the kiln so that articles on the top of the car experience a different temperature profile from those situated near the car base. This difference in thermal experience may result in a difference in the amount of deformation experienced by the ware, higher temperatures result in lower parameter values of viscosity and elasticity and therefore yield increased deformation. Although accumulated experience of working with such articles reduces the duration of the design process to an extent, it is still undesirably and uneconomically long. The need for a model which predicts the deformation during firing of a variety of ware geometries and that incorporates the material parameters and also the method of support is clearly evident.

A model has been developed that predicts the viscoelastic deformation of a range of vitreous china testpieces during the firing process. The model constitutes a novel application of the transmission line modelling technique to viscoelastic deformation. The applicability of the model to the sanitary ware industry is addressed.

# CONTENTS

<b>Contents .....</b>	<b>i</b>
<b>Abstract.....</b>	<b>viii</b>
<b>Acknowledgements .....</b>	<b>ix</b>
<b>Chapter 1 Introduction .....</b>	<b>1</b>
1.1 Aim of Research.....	1
1.2 Thesis Overview.....	1
<b>Chapter 2 Background to Deformation .....</b>	<b>3</b>
2.1 Fluid Motion .....	4
2.1.1 Definition of a fluid.....	4
2.1.2 Continuum hypothesis .....	5
2.1.3 Lagrangian coordinate system .....	5
2.1.4 Acceleration of a fluid particle.....	5
2.1.5 Local fluid motion .....	6
2.1.6 Continuity .....	6
2.2 Viscous Flow .....	8
2.2.1 Viscosity.....	8

2.2.2	Navier-Stokes equations.....	10
2.3	Rigid Body Motion.....	13
2.3.1	Definition of a rigid body.....	13
2.3.2	Theorems of motion .....	13
2.3.3	Moment of inertia.....	14
2.3.4	Area moment of inertia.....	14
2.3.5	Radius of gyration .....	16
2.3.6	Angular momentum.....	16
2.4	Elastic Theory .....	17
2.4.1	Relationship between stress and strain .....	17
2.4.2	Bending beam theory .....	19
2.4.3	Bending in two perpendicular directions.....	25
2.5	Viscoelasticity .....	31
2.5.1	Maxwell model .....	32
2.5.3	Kelvin model.....	34
2.5.3	Three component models .....	36
2.5.4	Four component models.....	38
2.6	References.....	40
 <b>Chapter 3 Background to TLM.....</b>		<b>42</b>
3.1	Introduction to TLM.....	43
3.2	Applications of the TLM Technique.....	44

3.3 TLM Theory .....	44
3.4 Fundamentals of TLM.....	47
3.5 Initialisation of Pulses .....	56
3.6 Generation of Current and Current Loss.....	56
3.7 Variation of Parameters in a Diffusion Network .....	58
3.7.1 Variation in resistance.....	58
3.7.2 Variation in capacitance.....	60
3.8 Variation of Parameters in a Wave Network.....	63
3.9 References.....	65
<b>Chapter 4 Firing of Vitreous Clays .....</b>	<b>71</b>
4.1 Introduction .....	72
4.2 Whiteware Systems .....	72
4.2.1 Clay .....	73
4.2.2 Flux .....	74
4.2.3 Filler .....	75
4.3 The Firing Process .....	75
4.3.1 Smoking .....	76
4.3.2 Pre-heating .....	76

4.3.3	Full fire stage.....	77
4.3.4	Finishing stage.....	77
4.3.5	Cooling stage .....	77
4.4	Changes of State.....	78
4.4.1	Sintering.....	78
4.4.2	Vitrification .....	79
4.4.3	Fusion.....	79
4.5	Physical Changes During Firing .....	80
4.5.1	Volume .....	80
4.5.2	Porosity.....	82
4.5.3	Weight loss.....	82
4.5.4	Specific gravity .....	83
4.5.5	Strength.....	84
4.6	Effects of Excessive Heating .....	86
4.7	References.....	88
 <b>Chapter 5 TLM Models .....</b>		<b>90</b>
5.1	Trouton's Descending Fluid .....	91
5.2	Formulation of an Elongational Viscous Model .....	92
5.2.1	Boundary conditions .....	97
5.2.2	Results of elongational model .....	99

5.3	Formulation of a Bending Viscous Model .....	104
5.3.1	Boundary conditions .....	112
5.3.2	PID control and tuning .....	115
5.4	Temporal and Spatial Convergence.....	118
5.5	Comparison with Finite Difference.....	120
5.6	Rotation under Constant Stress.....	124
5.7	Coupled Viscous Model .....	131
5.8	Meshing and Beams of Initial Curvature.....	132
5.9	Incorporation of Elasticity .....	135
5.9.1	Elasticity in series.....	135
5.9.2	Elasticity in parallel.....	136
5.9.3	Combinations of series and parallel elasticity.....	140
5.10	Viscous Deformation in Two Dimensions.....	142
5.11	Formulation of an Elastic Bending Model .....	145
5.12	References .....	149
 <b>Chapter 6 Application of TLM Models to Ceramics .....</b>		<b>151</b>
6.1	Existing Deformation Models .....	152

6.2	Viscoelastic Behaviour at High Temperatures.....	153
6.3	Applicability of Deformation Models During Firing Cycle.....	156
6.4	Variation of Viscosity and Elasticity During Firing.....	156
6.5	Firing Shrinkage.....	168
6.6	Analytical Elastic Solutions for Test Pieces .....	170
6.6.1	Hoop .....	170
6.6.2	Mushroom Shell.....	177
6.7	Comparison of TLM with Experimental Results .....	181
6.7.1	Details of testpieces.....	181
6.7.2	Results .....	185
6.8	References.....	194
 <b>Chapter 7 Discussion.....</b>		<b>197</b>
7.1	Summary of Thesis.....	198
7.2	Important Features of Deformation Models .....	199
7.3	General Applicability of Models .....	202
7.4	Conclusion .....	206

<b>Appendix I .....</b>	<b>207</b>
-------------------------	------------

## **ABSTRACT**

During firing, the deformation of ceramic articles under their own weight may be problematic particularly in the sanitary ware industry where articles are large. A model has been developed that predicts the viscoelastic deformation of a range of vitreous china testpieces during the firing process. The model constitutes a novel application of the transmission line modelling technique to viscoelastic deformation. The applicability of the model to the sanitary ware industry is addressed.

## ACKNOWLEDGEMENTS

I would like to express my sincere gratitude to my supervisor, Dr Sue Pulko, for the opportunity to carry out this research and for all her guidance in helping me become an engineer.

I would like to thank both Sue and Dr Tony Wilkinson for their insight and thoughts on various aspects of the work in the thesis and I hope that they received as much enjoyment as I from our discussions.

Many thanks are owed to Dr Bob Wallis of the EDM department, without whose help I would still be struggling with the understanding of the advanced theory of elasticity.

Finally, and by no means less importantly, I would like to acknowledge the support of my family and my friends. I would especially like to thank my Mum for both her financial and emotional support, particularly in this last year. I would also like to thank Andy Wright for believing in my ability to succeed when the going got tough and I was highly tempted to opt for an easier life.

Thanks again for all your encouragement.

# CHAPTER 1

## INTRODUCTION

### 1.1 Aim of Research

In the sanitary ware industry the time associated with designing new geometries of ware is considerably long. This is due to the process of trial and error presently carried out to determine the mould shape necessary to produce the desired finished articles. Large articles such as wash basins, toilet pedestals and bidets may deform significantly under their own weight during firing. The method of support is limited as these articles are fired only once and in their glazed state, so that the ware stands on its unglazed surface as it passes through the kiln. Kiln cars carry the ware through the kiln so that articles on the top of the car experience a different temperature profile from those situated near the car base. This difference in thermal experience may result in a difference in the amount of deformation experienced by the ware, higher temperatures result in lower parameter values of viscosity and elasticity and therefore yield increased deformation. Although accumulated experience of working with such articles reduces the duration of the design process to an extent, it is still undesirably and uneconomically long. The need for a model which predicts the deformation during firing of a variety of ware geometries and that incorporates the material parameters and also the method of support is clearly evident.

### 1.2 Thesis Overview

This thesis introduces a novel application of the transmission line modelling (TLM) technique to the deformation of bodies exhibiting either viscous, elastic or viscoelastic behaviour. The modelling concepts are applied

initially to elongating columns of viscous fluid, deforming under their own weight. Most of the work thereafter, however, concentrates upon bending under gravity where it is assumed that in plane shearing effects are negligible so that the deformation may be considered to be pure bending. The incorporation of classical elastic small strain theory is shown to lead to the development of viscoelastic models for bodies of various geometries.

The preliminary chapters provide the reader with background information regarding deformation theory of viscous fluids and elastic bodies, and also provide a basic introduction to the modelling technique employed. The object of the work was to develop models of deformation which could be applied successfully to the deformation of vitreous china ware during the firing process. Chapters documenting the compositional and physical characteristics of this particular material during firing and its behaviour at high temperatures are, therefore, included. Original work is discussed in chapter 5 where details of the deformation models developed using the TLM technique are provided. The applicability of the models to the sanitary ware industry is discussed in the following chapter accompanied by the comparison of simulated and experimental results for a variety of ceramic test pieces. The geometries of the test pieces comprise cantilevers, hoops and a three dimensional mushroom shaped shell having rotational symmetry. A chapter discussing the work and its general applicability concludes the thesis.

## **CHAPTER 2**

### **BACKGROUND TO DEFORMATION**

The concepts of fluid flow are revised and shown to lead to the formulation of equations describing the flow of viscous fluids. Details of rigid body motion are also revised and lay the foundations for the classical bending theory as applied to elastic beams and plates for small strain. Traditional mechanical models describing the viscoelastic behaviour of materials conclude this chapter.

## **2.1 Fluid Motion**

### **2.1.1 Definition of a fluid**

A fluid is a substance, either liquid or gas, which has the ability to flow. Fluids differ from solids in their molecular structure; the molecular movement in solids being smaller and the intermolecular forces of attraction being much greater than in fluids. As a result, if a solid rigid body is considered to be made up of a collection of particles then all the particles within the body are held together rigidly and move with a common velocity, namely that of the centre of mass of the body. The same is not true of particles in a fluid, where positions of particles are interchangeable. If a constant shearing force is exerted upon a solid body which is at rest then, in general, it will resist movement. A body which is elastic will deform instantaneously; a larger value of Young's Modulus yielding an increase in the resistance to deformation. However, if the solid body is plastic in nature then the initial deformation may be elastic with plastic flow occurring when the force exceeds a particular value. A state of equilibrium is attained with the internal resistive forces so that further deformation arises purely as a result of an applied force of increasing magnitude. If a fluid experiences a constant shearing force, flow will commence immediately and will continue for as long as the force is applied. When a variation in velocity exists between different layers within the fluid equilibrium cannot be reached. Returning to the plastic body, the existence of the resistive forces is such that upon removal of the force the body may regain its original shape provided that the force is removed prior to the onset of plastic flow so that the body is behaving elastically. If the removal of the force occurs during plastic flow then the body will be permanently set. The fluid, however, will always retain its new shape once the force has been removed, since in the absence of flow any internal resistance ceases [1].

### 2.1.2 Continuum hypothesis

The physical properties of a fluid are dependent upon its molecular structure and so it would seem that a microscopic view is necessary when considering fluids in motion. This viewpoint, however, is not consistent with the measurement of material parameters, which are usually obtained from the bulk material. The continuum hypothesis offers a macroscopic view where fluids are considered continuous in so much that their properties are uniform over small volumes, each volume containing many molecules, and that changes in these material properties, from volume to volume, remain smooth. It is now not unreasonable to represent a fluid particle by such a volume assigned with local parameter values.

### 2.1.3 Lagrangian coordinate system

The position of each point in a fluid can be determined if the velocity of the corresponding fluid particle is known for a given time interval. In this way the position vector of a particle is a function of time and contributes to the time history of each point in the fluid [2]. The concept of the Lagrangian coordinate system is also used when considering the motion of rigid bodies, which can be either translational or rotational.

### 2.1.4 Acceleration of a fluid particle

The position vector of a particle is a function of both time and space, that is  $\mathbf{r}=\mathbf{r}(t)$ . If the velocity in the  $x$  direction at  $\mathbf{r}$  is denoted by  $v$  then it also follows that  $v=v(t)$ . Thus, the derivative with respect to time will consist of partial time and space derivatives. The acceleration of the particle in one dimension is, therefore, given by

$$\frac{Dv}{Dt} = \frac{\partial v}{\partial t} + v \frac{\partial v}{\partial x} \quad (2.1)$$

where the first term on the right is the local acceleration of the particle and the second term is the accumulative, or convective, acceleration due to the rest of the fluid. Thus, each fluid particle has an acceleration consisting of two components; one component forcing the particle to move with the bulk of the fluid and the other component allowing the particle some independent motion. The substantial derivative  $\frac{D}{Dt}$  is itself Lagrangian in nature; the movement of a fluid particle being monitored over time so that (2.1) may be determined.

### 2.1.5 Local fluid motion

The local motion of a fluid does bare some resemblance to the local deformation of a solid elastic body in so much that a fluid element may translate, rotate and, if compressible, increase its volume by a pure straining motion. If the flow is incompressible then the motion may be considered solely as a superposition of rigid body translation and rigid body rotation [3]. The acceleration of the fluid associated with each type of motion takes the form of equation (2.1), where in the case of rotational motion the velocity  $v$  will be replaced by angular velocity  $\omega$ .

### 2.1.6 Continuity

The equation of continuity results from the consideration of mass conservation as a fluid flows through a fixed region in space [4]. The conservation of mass ensures that matter can be neither created nor destroyed. Considering the mass flow per unit area, or the mass flux, in the x-direction through the differential control volume in figure 2.1, the net mass flow is given by

$$\frac{\partial m_x}{\partial t} - \frac{\partial m_{x+dx}}{\partial t} = - \frac{\partial(\rho u \, dy \, dz)}{\partial x} dx = - \frac{\partial(\rho u)}{\partial x} dx \, dy \, dz \quad (2.2)$$

where  $m_x$  is the mass at position  $x$ .

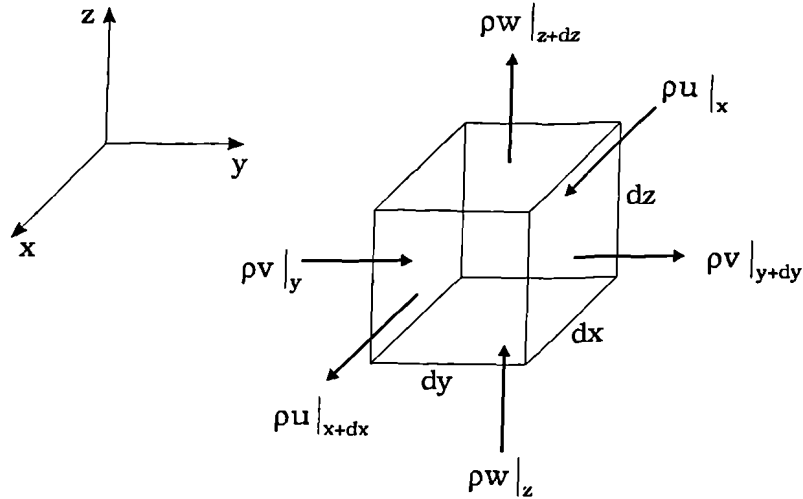


Figure 2.1 Mass flux through a differential control volume.

The net mass flow in the other two directions can be obtained in a similar manner, which leads to the following expression for the total mass entering the control volume

$$- \left( \frac{\partial(\rho u)}{\partial x} + \frac{\partial(\rho v)}{\partial y} + \frac{\partial(\rho w)}{\partial z} \right) dx dy dz \quad (2.3)$$

where u, v and w are the components of the velocity of flow in the x, y and z directions respectively.

The change in mass entering the control volume over a given time period must be equivalent to the above expression, from the conservation of mass. Thus,

$$\frac{\partial(\rho dx dy dz)}{\partial t} = - \left( \frac{\partial(\rho u)}{\partial x} + \frac{\partial(\rho v)}{\partial y} + \frac{\partial(\rho w)}{\partial z} \right) dx dy dz$$

which leads to

$$\frac{\partial \rho}{\partial t} + \frac{\partial(\rho u)}{\partial x} + \frac{\partial(\rho v)}{\partial y} + \frac{\partial(\rho w)}{\partial z} = 0 \quad (2.4).$$

In the case of an incompressible fluid, where the density does not change with time nor with direction, the continuity equation (2.4) simplifies to

$$\frac{\partial u}{\partial x} + \frac{\partial v}{\partial y} + \frac{\partial w}{\partial z} = 0 \quad (2.5).$$

## 2.2 Viscous Flow

### 2.2.1 Viscosity

The viscosity of a fluid is a measure of the resistance to motion of adjacent layers within the fluid. Shearing forces, arising from a moving plate acting on a fluid which is in contact with a solid boundary as in figure 2.2, set up an increasing velocity gradient in a direction perpendicular to the boundary such that the first layer of fluid particles is at rest with respect to the boundary.

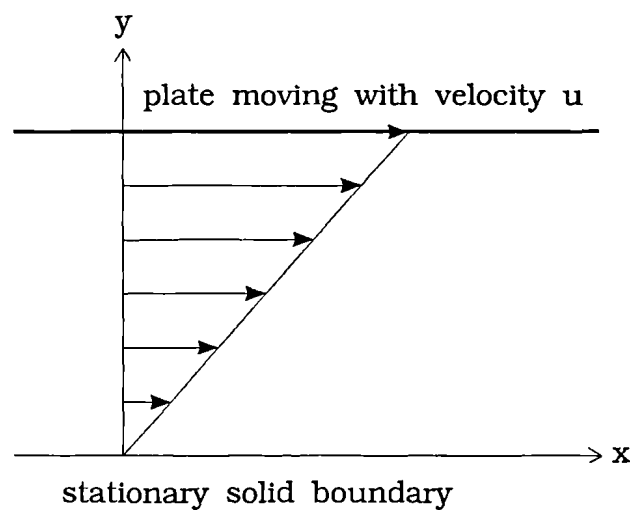


Figure 2.2 Moving plate in contact with viscous fluid setting up a velocity gradient.

It is this no-slip condition which gives the impression of the ability of a viscous fluid to stick to the walls of the vessel in which it is contained. The condition fails when the fluid can no longer be treated as a continuum. The shearing stresses oppose relative motion of the fluid layers. The stress in the x-direction is given by

$$\tau_x = \eta \frac{du}{dy} \quad (2.6)$$

where,  $u$  is the velocity in the  $x$  direction and  $\eta$  is the coefficient of dynamic viscosity. Thus, the coefficient of dynamic viscosity is defined as the shear force per unit area necessary to cause relative movement of unit velocity

between layers unit distance apart within the fluid. The SI units of dynamic viscosity are, therefore,  $\text{kgm}^{-1}\text{s}^{-1}$  [5]. The shearing stress can also be shown to be related to the rate of change of shearing strain  $\gamma$ . Since,

$$du = \frac{dx}{dt} \quad (2.7)$$

then,

$$\frac{du}{dy} = \frac{dx/dt}{dy} \quad (2.8).$$

Now,

$$\frac{dx}{dy} = \gamma \quad (2.9)$$

thus, substituting (2.9) into (2.8) gives

$$\frac{du}{dy} = \frac{d\gamma}{dt} \quad (2.10)$$

which, when substituted back into (2.6), leads to

$$\tau_x = \eta \frac{d\gamma}{dt} \quad (2.11).$$

When the above relationship holds the fluid is termed Newtonian. Thus, for a Newtonian fluid under constant stress, flow continues at a constant rate.

Many fluids do not exhibit a linear stress/strain rate relationship and are termed non-Newtonian. The types of flows in this case may be either time independent, time dependent or viscoelastic.

(i) Time independent flow

The shear strain rate is a single valued, non-linear function of the shear stress. This behaviour is demonstrated by a Bingham plastic body which behaves as a solid until a particular stress, termed the yield stress, is reached whereupon the body behaves as a Newtonian viscous fluid.

(ii) Time dependent flow

The shearing rate is not a single valued function of the shear stress and may be dependent upon the past shear history of the fluid. The shear stress/strain rate curve may also form an hysteresis loop. Examples of fluids

exhibiting time dependency include thixotropic fluids, for which the shear stress decreases with time and displays hysteresis behaviour, and rheopectic fluids, for which the shear stress increases with time.

(iii) Viscoelastic flows

Here both the shear strain and the shear strain rate are related to the shear stress. There are several classifications of viscoelastic flow, each combining the elements of viscosity and elasticity, and are treated in greater detail towards the end of this chapter in section 2.5.

**2.2.2 Navier-Stokes equations**

The distribution of normal and shear stresses over an infinitesimal volume of fluid is depicted in figure 2.3. The components are shown acting on only three faces of the element for simplicity; components on the remaining faces act in opposition to those already specified.

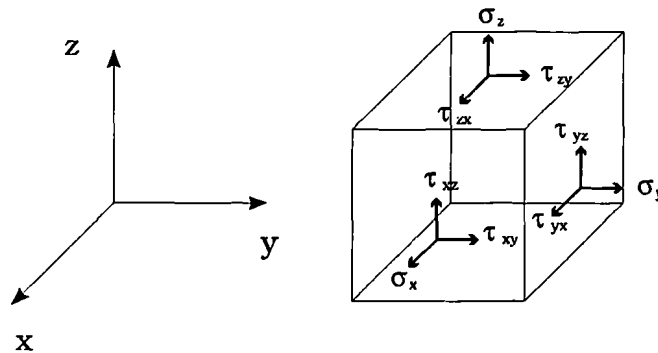


Figure 2.3 Normal and shear stress components acting on a volume element.

Taking moments about the x axis leads to the further simplification that

$$\tau_{yz} = \tau_{zy} \quad (2.12).$$

Taking moments about the y axis similarly leads to

$$\tau_{zx} = \tau_{xz} \quad (2.13)$$

and taking moments about the z axis leads to

$$\tau_{xy} = \tau_{yx} \quad (2.14) .$$

The Navier-Stokes equations arise from the consideration of Newton's second law of motion when applied to a differential control volume [6,7].

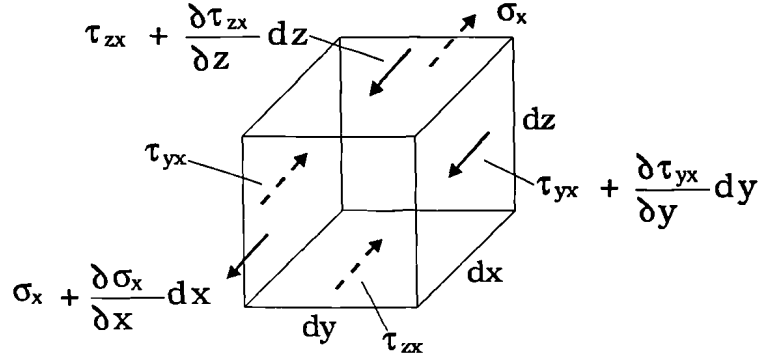


Figure 2.4 Stresses acting on a differential control volume.

Considering figure 2.4, the net stress across the volume in the x-direction is thus given by

$$\frac{\partial \sigma_x}{\partial x} dx + \frac{\partial \tau_{yx}}{\partial y} dy + \frac{\partial \tau_{zx}}{\partial z} dz \quad (2.15)$$

From equation (2.6) it was shown that

$$\tau_x = \eta \frac{du}{dy} \quad (2.16).$$

For the above control volume the shear stress  $\tau_{yx}$  is given by

$$\tau_{yx} = \eta \left( \frac{\partial u}{\partial y} + \frac{\partial v}{\partial x} \right) \quad (2.17)$$

and, similarly,

$$\tau_{zx} = \eta \left( \frac{\partial u}{\partial z} + \frac{\partial w}{\partial x} \right) \quad (2.18).$$

For normal stress the following equation holds [6]:

$$\sigma_x = -p + 2\eta \frac{\partial u}{\partial x} \quad (2.19)$$

where p is the externally applied pressure acting on the fluid.

Thus, the net force per unit mass in the x direction,  $F_x$ , can now be written as

$$F_x = \frac{1}{\rho} \left( \frac{\partial}{\partial x} \left( -p + 2 \eta \frac{\partial u}{\partial x} \right) + \eta \frac{\partial}{\partial y} \left( \frac{\partial v}{\partial x} + \frac{\partial u}{\partial y} \right) + \eta \frac{\partial}{\partial z} \left( \frac{\partial u}{\partial z} + \frac{\partial w}{\partial x} \right) \right) \quad (2.20)$$

However, from the continuity equation (2.5) for an incompressible fluid,

$$\frac{\eta}{\rho} \frac{\partial}{\partial x} \left( \frac{\partial u}{\partial x} + \frac{\partial v}{\partial y} + \frac{\partial w}{\partial z} \right) = 0$$

so, the equation for the net force per unit mass reduces to

$$F_x = - \frac{1}{\rho} \frac{\partial p}{\partial x} + \frac{\eta}{\rho} \left( \frac{\partial^2 u}{\partial x^2} + \frac{\partial^2 u}{\partial y^2} + \frac{\partial^2 u}{\partial z^2} \right) \quad (2.21)$$

Gravity also acts on the volume of fluid to produce an additional force, so that the total force per unit mass becomes

$$- \frac{1}{\rho} \frac{\partial p}{\partial x} + \frac{\eta}{\rho} \left( \frac{\partial^2 u}{\partial x^2} + \frac{\partial^2 u}{\partial y^2} + \frac{\partial^2 u}{\partial z^2} \right) + g_x \quad (2.22)$$

Similar expressions can be obtained in each of the other two directions.

From Newton's Second Law of Motion, the acceleration of a body is proportional to the sum of external forces acting upon it. Thus,

$$\begin{aligned} \frac{Du}{Dt} &= - \frac{1}{\rho} \frac{\partial p}{\partial x} + \frac{\eta}{\rho} \left( \frac{\partial^2 u}{\partial x^2} + \frac{\partial^2 u}{\partial y^2} + \frac{\partial^2 u}{\partial z^2} \right) + g_x \\ \frac{Dv}{Dt} &= - \frac{1}{\rho} \frac{\partial p}{\partial y} + \frac{\eta}{\rho} \left( \frac{\partial^2 v}{\partial x^2} + \frac{\partial^2 v}{\partial y^2} + \frac{\partial^2 v}{\partial z^2} \right) + g_y \\ \frac{Dw}{Dt} &= - \frac{1}{\rho} \frac{\partial p}{\partial z} + \frac{\eta}{\rho} \left( \frac{\partial^2 w}{\partial x^2} + \frac{\partial^2 w}{\partial y^2} + \frac{\partial^2 w}{\partial z^2} \right) + g_z \end{aligned} \quad (2.23)$$

where, as in equation (2.1),

$$\begin{aligned}\frac{Du}{Dt} &= \frac{\partial u}{\partial t} + u \frac{\partial u}{\partial x} \\ \frac{Dv}{Dt} &= \frac{\partial v}{\partial t} + v \frac{\partial v}{\partial y} \\ \frac{Dw}{Dt} &= \frac{\partial w}{\partial t} + w \frac{\partial w}{\partial z}\end{aligned}\tag{2.24}.$$

## 2.3 Rigid Body Motion

### 2.3.1 Definition of a rigid body

A solid body in which any two particles remain a fixed distance apart regardless of the forces acting upon the body is defined as rigid [8].

### 2.3.2 Theorems of motion

Euler's theorem states that for a rigid body rotating about a point its motion is equivalent to rotation about a line passing through the given point.

Chasle's theorem states that rigid body motion is described by the translation and rotation of a certain point in the body. The point of motion commonly being the centre of mass of the body.

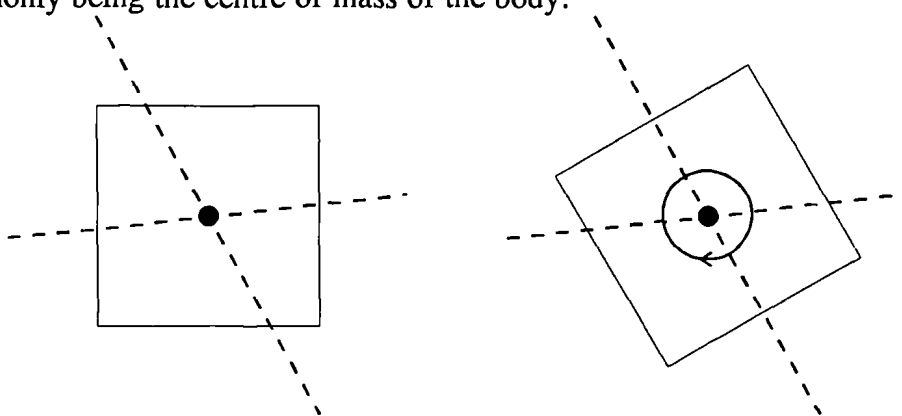


Figure 2.5 Translation and rotation of a rigid body about its centre of mass.

### 2.3.3 Moment of inertia

The kinetic energy, KE, of a body of mass  $m$  and translational velocity  $v$  is given by

$$KE = \frac{1}{2} m v^2 \quad (2.25).$$

However, if the same body is rotating about an axis with angular velocity  $\omega$  then the corresponding kinetic energy becomes

$$KE = \frac{1}{2} I \omega^2 \quad (2.26)$$

where  $I$  is the moment of inertia of the body.

Thus, if the body is a distance  $r$  from the axis then

$$v = r \omega \quad (2.27).$$

Substituting now for  $v$  into equation (2.25) and comparing with equation (2.26) yields

$$I = m r^2 \quad (2.28).$$

### 2.3.4 Area moment of inertia

The moment of inertia of a plane area is calculated with respect to an axis lying in that plane. Referring to figure 2.6 and taking the  $z$  axis to be the axis of rotation then the area moment of inertia,  $I_z$ , is given by

$$I_z = \int_A y^2 dA \quad (2.29).$$

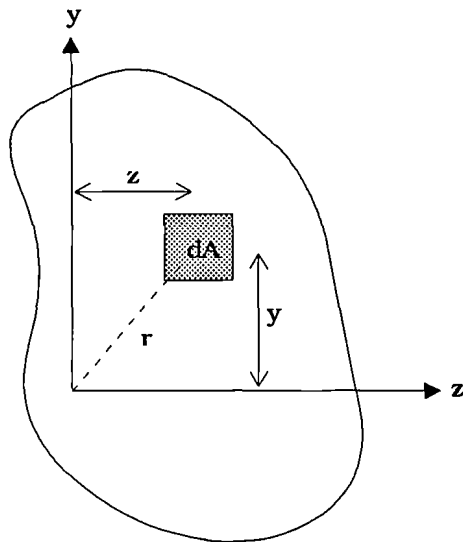


Figure 2.6 Element of area  $dA$  within a body.

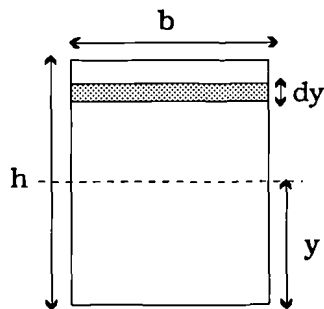


Figure 2.7 Rectangular area of cross section with central axis at  $y=0$ .

Applying the above integral of equation (2.29) to a rectangle which consists of small elements of area  $b dy$ , as depicted in figure 2.7, yields

$$I_z = 2 \int_0^{h/2} y^2 b dy \quad (2.30)$$

$$= \frac{b h^3}{12} \quad (2.31).$$

Similarly, the calculation of  $I_y$  yields

$$I_y = \frac{h b^3}{12} \quad (2.32).$$

### 2.3.5 Radius of gyration

The radius of gyration with respect to an axis is equal to the square root of the area moment of inertia about that axis divided by the area. Thus, the radius of gyration of the rectangle with respect to the z axis,  $k_z$ , is given by

$$k_z = \sqrt{\frac{I_z}{A}} \quad (2.33)$$

$$= \frac{h}{\sqrt{12}} \quad (2.34)$$

and similarly,

$$k_y = \sqrt{\frac{I_y}{A}} \quad (2.35)$$

$$= \frac{b}{\sqrt{12}} \quad (2.36).$$

### 2.3.6 Angular momentum

The rate of change of angular momentum is equal to the sum of the moments of the external forces acting on a body. Thus, if  $\mathbf{r}_i$  denotes the position vector of the force  $\mathbf{F}_i$  then the rate of change of angular momentum,  $\mathbf{J}$ , is given by

$$\frac{d\mathbf{J}}{dt} = \sum_i \mathbf{r}_i \times \mathbf{F}_i \quad (2.37)$$

where  $\mathbf{J}$  is related to the angular velocity,  $\boldsymbol{\omega}$ , by

$$\mathbf{J} = I \boldsymbol{\omega} \quad (2.38)$$

with the moment of inertia,  $I$ , as defined in equation 2.28.

## 2.4 Elastic Theory

### 2.4.1 Relationship between stress and strain

The components of stress acting on a solid body are identical to those shown in figures 2.3 and 2.4 acting on a fluid volume but differ in their relationship to the associated components of strain. When an elastic body whose material properties are isotropic is subjected to a normally applied tensile (or compressive) force the corresponding stress in the body produces elongation of the material, in the direction of the applied force. The amount of elongation per unit stress varies from material to material and thus the proportionality factor relating stress to strain is material dependent. The proportionality factor is Young's modulus of elasticity,  $E$ , and is defined by the following equation [9]

$$E = \frac{\sigma_x}{\varepsilon_x} \quad (2.39)$$

which is also known as Hooke's Law. In equation (2.39)  $\sigma_x$  and  $\varepsilon_x$  are the tensile (or compressive) stress and strain in the  $x$  direction, respectively. Thus, for an elastic solid the strain associated with a constant stress is itself constant. The elongation of the material is accompanied by contraction in the lateral plane, the magnitude of which being determined by the value of Poisson's ratio,  $\nu$ , for that particular material so that

$$\nu = \frac{\text{lateral strain}}{\text{longitudinal strain}} \quad (2.40).$$

In terms of the tensile stress

$$\varepsilon_y = -\nu \frac{\sigma_x}{E} \quad (2.41)$$

and,

$$\varepsilon_z = -\nu \frac{\sigma_x}{E} \quad (2.42)$$

the negative sign denoting compression.

Clearly, then, for a three dimensional body it follows that the full form of the stress-strain relations is

$$\varepsilon_x = \frac{1}{E} (\sigma_x - \nu (\sigma_y + \sigma_z)) \quad (2.43)$$

$$\varepsilon_y = \frac{1}{E} (\sigma_y - \nu (\sigma_z + \sigma_x)) \quad (2.44)$$

$$\varepsilon_z = \frac{1}{E} (\sigma_z - \nu (\sigma_x + \sigma_y)) \quad (2.45).$$

In the case of a shear stress,  $\tau_{xy}$ , acting on the body in the y direction and in the plane normal to the x axis, the following relationship holds

$$\tau_{xy} = G \gamma_{xy} \quad (2.46)$$

where,  $\gamma_{xy}$  is the shear strain and  $G$  is the shear modulus or the modulus of rigidity.

Similarly,

$$\tau_{yz} = G \gamma_{yz} \quad (2.47)$$

and

$$\tau_{zx} = G \gamma_{zx} \quad (2.48).$$

Although the normal and shear stresses are independent of one another, the shear modulus is related to Young's Modulus according to

$$G = \frac{E}{2(1 + \nu)} \quad (2.49).$$

If, under stretching, the volume of a body does not change then  $\nu = 0.5$  and, therefore,  $G = \frac{E}{3}$ , so that the effect of Young's modulus is divided equally

between each of the three shearing stresses.

### 2.4.2 Bending beam theory

Pure bending of a beam results from the application of equal and opposite moments to the ends of an initially straight beam, so that the final deformation represents a symmetric curve [10]. The theory is built upon the following assumptions:

- (i) the material is homogeneous and isotropic;
- (ii) the beam is long in comparison to its depth, so that the effect of shear is negligible;
- (iii) the width of the beam is not so great that the beam may be considered as a thin plate;
- (iv) cross-sections of the beam remain plane and perpendicular to longitudinal fibres.

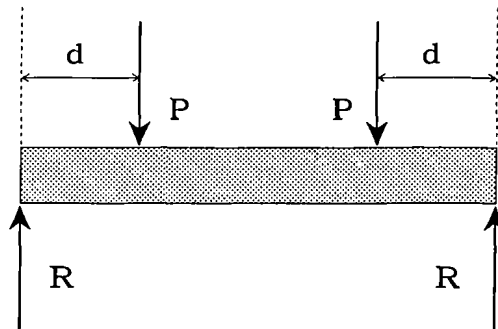


Figure 2.8 Simply supported beam subject to two equal forces.

Consider an elastic beam subject to two equal forces of magnitude,  $P$ , acting at a distance  $d$  from each end of the beam, as depicted in figure 2.8. Then, for equilibrium the reactions,  $R$ , at each end are equal to  $P$ . In order to determine the distribution of stress within the beam, a typical cross-section  $ab$  is examined. The beam is fictitiously divided at the cross-section as shown in figure 2.9a.

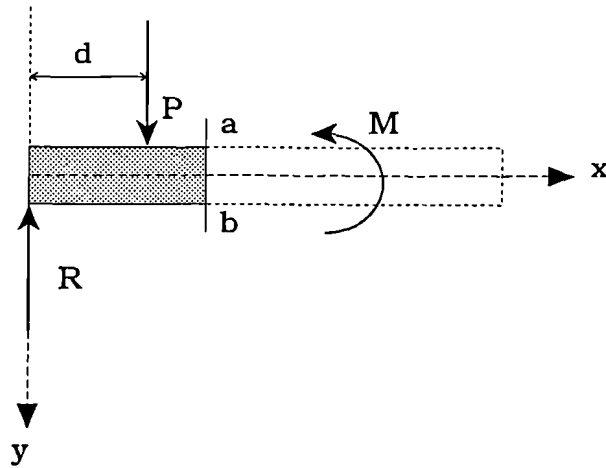


Figure 2.9a Fictitious division of beam at ab.

The effect of the remainder of the bar to the right of the cross-section is replaced by a bending moment,  $M$ , acting on  $ab$  such that

$$M = P d \quad (2.50).$$

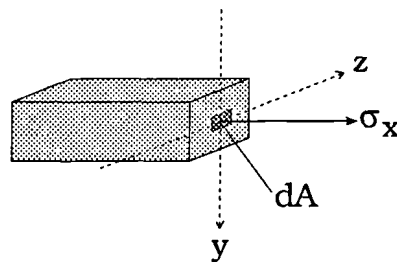


Figure 2.9b Normal stress acting on an elemental area  $dA$  at cross-section  $ab$ .

Looking at the cross-section itself, shown in figure 2.9b, then for equilibrium the sum of the moments of the internal forces will be equivalent to the resistive couple  $M$ . That is,

$$\sum F_x y = M \quad (2.51)$$

which leads to

$$\int_A \sigma_x dA y = M \quad (2.52).$$

Applying Hooke's Law gives

$$\int_A E \epsilon_x dA y = M \quad (2.53).$$

Close examination of a section of beam which has been subject to pure bending as in figure 2.10, allows the determination of the strain  $\epsilon_x$ . Elongation occurs along the lower length of the beam with an associated contraction along the upper length. As in the case of the action of tensile or compressive forces, lateral changes in dimension accompany longitudinal changes. Along the lower convex length fibres in the lateral plane contract and those in the plane normal to the upper concave length expand according to

$$\epsilon_z = -\nu \epsilon_x = -\nu \frac{\delta l}{l} = -\nu \frac{y}{r} \quad (2.54).$$

The lateral plane along mn, through which the neutral axis passes, contains fibres which do not experience any change in length during bending and thus

$$\epsilon_x = \epsilon_z = 0 \quad (2.55).$$

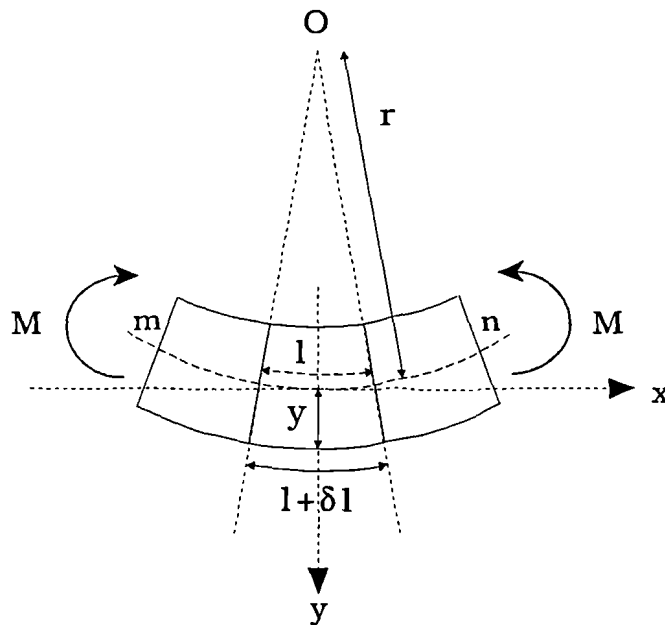


Figure 2.10 Section of beam after pure bending with radius of curvature,  $r$ .

Fibres along the sides of the beam remain normal to those in the longitudinal direction, so that the section acquires a new shape. The area of the section, however, remains constant since any elongation below the neutral axis is

balanced by an equivalent contraction located at the same distance above the neutral axis. Substituting for  $\epsilon_x = \frac{y}{r}$  in equation (2.53) leads to

$$M = \int_A \frac{E}{r} y^2 dA = \frac{E}{r} I_z \quad (2.56)$$

where, from equation (2.29),

$$I_z = \int_A y^2 dA .$$

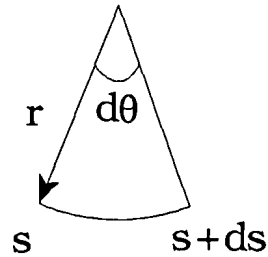


Figure 2.11 Section of the neutral axis from s to s+ds.

The angular deformation of each point along the beam can be determined from consideration of figure 2.11, which depicts the deflection of the neutral axis in the beam section. An element of length ds has a radius of curvature r such that two points m and n situated at s and s+ds, respectively, along the axis have an angular separation dθ. If the path is traced from point m to n, then as the position along the neutral axis increases the angular separation decreases. Thus,  $ds = -rd\theta$  and substitution for r leads to

$$\theta = - \int \frac{M}{E I_z} ds \quad (2.57)$$

For small deflections of the beam the following approximations hold:

$$dx = ds \text{ and } \tan\theta = \theta = \frac{dy}{dx} \quad (2.58)$$

which enables a solution for the deflection y of the beam, namely

$$y = - \int \left( \int \frac{M}{E I_z} dx \right) dx \quad (2.59).$$

Thus, if the form of the bending moment, M, is known then the deflection at each point along the bar can be determined.

The following examples illustrate the application of the above theory firstly to a simply supported beam and secondly to a cantilever. In both cases the load represents the weight and is distributed uniformly along the length of the beam.

Example 1 Simply supported beam

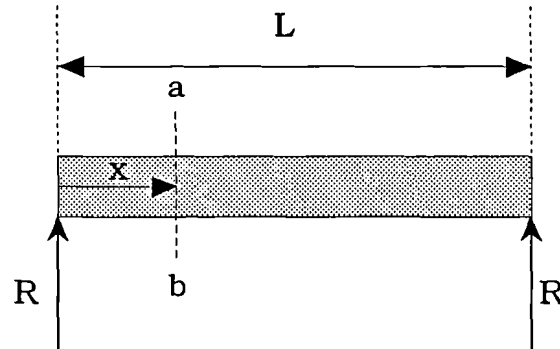


Figure 2.12 Simply supported beam of uniform load  $w$  per unit length.

Considering a cross-section  $ab$  situated a distance  $x$  along the beam of total length  $L$ , as in figure 2.12, then resolving forces to the left of  $ab$  yields;

$$R - wx = V \quad (2.60)$$

where  $w$  is the weight per unit length of the beam;

$R = \frac{wL}{2}$  is the vertical reaction at each support;

and  $V$  is the total shearing force acting at the cross section which is related to the bending moment,  $M$ , by

$$V = \frac{dM}{dx} \quad (2.61).$$

Thus,

$$M = \frac{wLx}{2} - \frac{wx^2}{2} \quad (2.62)$$

which leads to

$$\frac{dy}{dx} = - \int \frac{wx(L-x)}{2EI_z} dx \quad (2.63).$$

The following boundary conditions also apply:

the midpoint of the beam,  $x = \frac{L}{2}$ , is a point of inflection so that  $\frac{dy}{dx} = 0$ ;

the deflection at the two ends of the beam is equal to zero so that  $y=0$  at  $x=0$  and  $x=L$ .

By use of (2.58), the first boundary condition yields a solution for  $\theta$ ;

$$\theta = \frac{w}{2EI_z} \left( \frac{x^3}{3} - \frac{x^2L}{2} + \frac{L^3}{12} \right) \quad (2.64)$$

The remaining boundary conditions yield a solution is for the deflection  $y$ ;

$$y = \frac{w}{24 E I_z} (L^3x - 2Lx^3 + x^4) \quad (2.65).$$

### Example 2 Cantilever beam

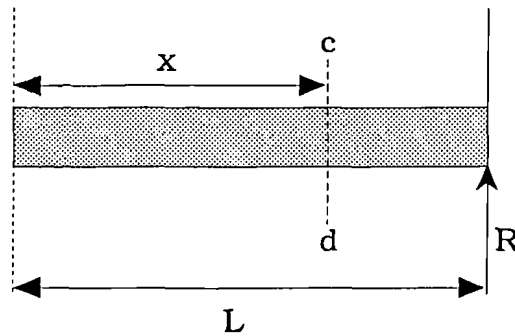


Figure 2.13 Cantilever beam subject to uniform load  $w$  per unit length.

Consider a beam supported at one end, as in figure 2.13. The reaction at the support is equivalent to the whole weight of the beam. Taking a cross-section  $cd$  through the beam and looking at forces acting on the left hand side leads to

$$V = 0 - wx \quad (2.66)$$

and

$$M = - \frac{wx^2}{2} \quad (2.67)$$

thus,

$$\frac{dy}{dx} = - \int \frac{wx^2}{2 E I_z} dx \quad (2.68).$$

The boundary conditions which apply here are:

the gradient at the supported end of the beam is zero, so that at  $x = L$  ,  
 $\frac{dy}{dx} = 0$  ;

and the deflection is zero at the support, so that at  $x = L$  ,  $y = 0$ .

The following solutions for  $\theta$  and  $y$  can now be obtained;

$$\theta = \frac{w}{2 E I_z} \left( \frac{x^3}{3} - \frac{L^3}{3} \right) \quad (2.69).$$

$$y = \frac{w}{24 E I_z} (3L^4 - 4L^3x + x^4) \quad (2.70).$$

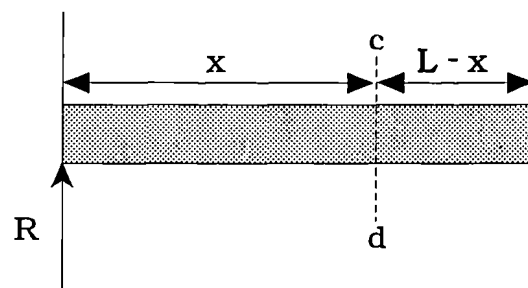


Figure 2.14 Beam supported on the left.

If, however, the beam is instead supported on the right, as in figure 2.14, then substituting  $L-x$  for  $x$  in the above equations yields the following solutions for  $\theta$  and  $y$ ;

$$\theta = \frac{w}{2 E I_z} \left( L^2x - Lx^2 + \frac{x^3}{3} \right) \quad (2.71)$$

$$y = \frac{w}{24 E I_z} (6L^2x^2 - 4Lx^3 + x^4) \quad (2.72).$$

### 2.4.3 Bending in two perpendicular directions

The deformation of a rectangular plate lying in the  $xy$  plane subject to the normal stresses  $\sigma_x$  and  $\sigma_y$  may be determined by consideration of a narrow strip along the length of the plate [11], as depicted in figure 2.15a.

The plate is of depth  $h$  and the strip has a width of unit length so that the strip resembles a beam of length  $L$  as described in the previous section.

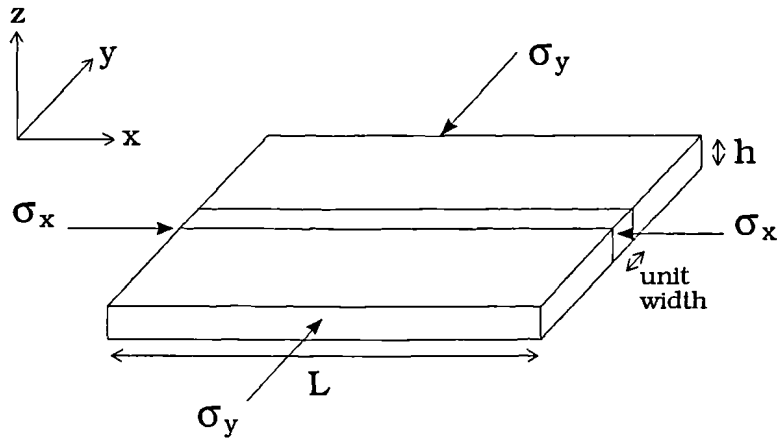


Figure 2.15a Rectangular plate containing a strip of unit width and subjected to stresses in two perpendicular directions.

As in bending beam theory the cross-sections remain plane so that in each of the two directions the only form of deformation is rotation about the neutral axes. The equations governing the stress/strain relationships in the two perpendicular directions result from equations (2.43) and (2.44) with  $\sigma_z=0$ , that is

$$\epsilon_x = \frac{1}{E} (\sigma_x - \nu \sigma_y) \quad (2.73)$$

$$\epsilon_y = \frac{1}{E} (\sigma_y - \nu \sigma_x) \quad (2.74).$$

If the plate is subject only to a load in the  $x$  direction then the strain in the  $y$  direction is zero so that equation (2.74) yields

$$\sigma_y = \nu \sigma_x \quad (2.75).$$

It then follows from equation (2.73) that

$$\sigma_x = \frac{\epsilon_x E}{(1 - \nu^2)} \quad (2.76).$$

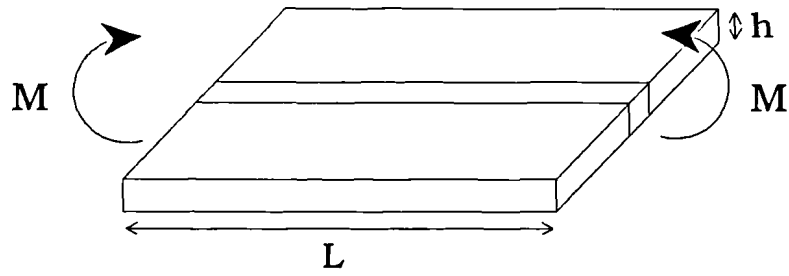


Figure 2.15b Pure bending of rectangular plate in one direction only.

Bending of the plate, resulting from the application of the bending moment depicted in figure 2.15b, yields a vertical deflection  $w$  which is related to the radius of curvature  $r$  by

$$\frac{1}{r} = -\frac{d^2w}{dx^2} \quad (2.77)$$

so that the strain  $\epsilon_x$  may now be expressed as

$$\epsilon_x = \frac{z}{r} = -z \frac{d^2w}{dx^2} \quad (2.78).$$

The bending moment is related to the stress by

$$M = \int_{-h/2}^{h/2} \sigma_x z dz \quad (2.79)$$

which, upon substitution for  $\sigma_x$  and  $\epsilon_x$  yields

$$M = \frac{-E h^3}{12 (1-\nu^2)} \frac{d^2w}{dx^2} \quad (2.80)$$

or, alternatively,

$$M = \frac{-E h^3}{12 (1-\nu^2)} \frac{d\theta}{ds} = -D \frac{d\theta}{ds} \quad (2.81)$$

where  $D = \frac{E h^3}{12 (1-\nu^2)}$  is the rigidity of the plate and replaces  $EI_z$  in equation (2.57) for the bending of beams.

Consider now a plate which is subjected to bending moments  $M_x$  and  $M_y$ , as shown in figure 2.16, such that the radii of curvature in the two perpendicular directions are respectively  $r_x$  and  $r_y$ .

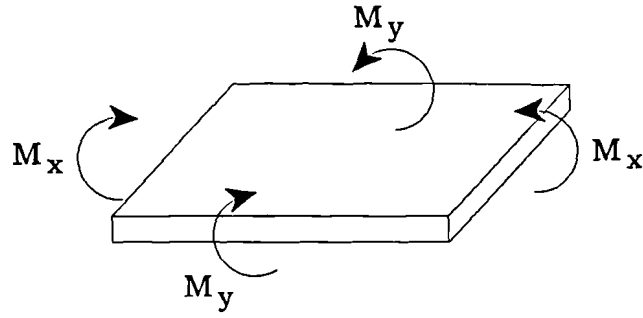


Figure 2.16 Rectangular plate subjected to bending in two perpendicular directions.

The perpendicular strains are therefore [12],

$$\varepsilon_x = \frac{z}{r_x} \quad (2.82)$$

$$\varepsilon_y = \frac{z}{r_y} \quad (2.83)$$

so that, from equations (2.73) and (2.74), the perpendicular stresses may be expressed as

$$\sigma_x = \frac{E z}{(1-\nu^2)} \left( \frac{1}{r_x} + \frac{\nu}{r_y} \right) \quad (2.84)$$

$$\sigma_y = \frac{E z}{(1-\nu^2)} \left( \frac{1}{r_y} + \frac{\nu}{r_x} \right) \quad (2.85).$$

Since, from equation (2.79)

$$M_x = \int_{-h/2}^{h/2} \sigma_x z \, dz$$

and, similarly,

$$M_y = \int_{-h/2}^{h/2} \sigma_y z \, dz$$

then substitution of equations (2.84) and (2.85) leads to

$$M_x = D \left( \frac{1}{r_x} + \frac{\nu}{r_y} \right) \quad (2.86)$$

and

$$M_y = D \left( \frac{1}{r_y} + \frac{\nu}{r_x} \right) \quad (2.87).$$

Application of equation (2.77) in each of the two directions finally yields

$$M_x = -D \left( \frac{d^2w}{dx^2} + \nu \frac{d^2w}{dy^2} \right) \quad (2.88)$$

and

$$M_y = -D \left( \frac{d^2w}{dy^2} + \nu \frac{d^2w}{dx^2} \right) \quad (2.89).$$

Consider now a circular plate [13], a segment of which is shown in figure 2.17. The section shown in the plate of sides  $aa'$  and  $bb'$  has a radial length  $dr$  and is subtended by the angle  $d\theta$ . The shearing force  $Q$  per unit length acts on the side  $aa'$  of the section at a radial distance  $r$  so that under conditions of equilibrium an opposing force per unit length acts on  $bb'$  of magnitude  $Q + \frac{dQ}{dr}dr$ . The moment per unit length  $M_r$  acting on  $aa'$  is balanced by the opposing moment per unit length  $M_r + \frac{dM_r}{dr}dr$  on  $bb'$ . Due to symmetry there is no change in the shearing force along the circumferential axis and therefore the moments  $M_t$  per unit length, causing rotation about this axis, balance one another.

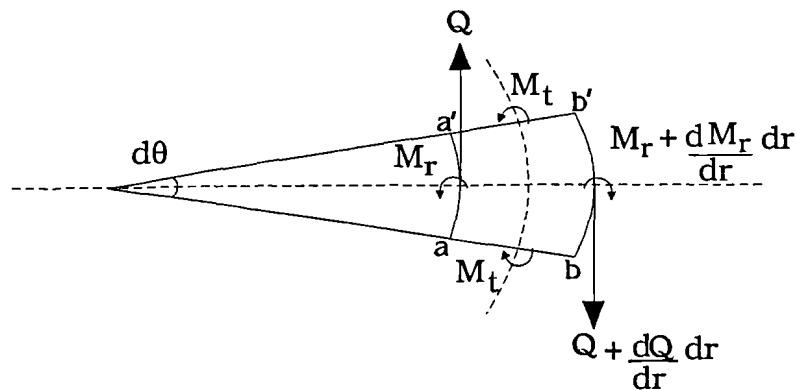


Figure 2.17 Segment of a 2-d circular plate.

Assuming  $M_r$  yields a positive rotation then  $M_t$ , acting on side  $a'b'$ , may be written in component form as follows;

$$M_t = M_t \cos\left(\frac{d\theta}{2}\right) \theta + M_t \sin\left(\frac{d\theta}{2}\right) \mathbf{r} \quad (2.90)$$

Similarly,  $M_t$  acting on side ab, may be expressed as;

$$M_t = -M_t \cos\left(\frac{d\theta}{2}\right) \theta + M_t \sin\left(\frac{d\theta}{2}\right) \mathbf{r} \quad (2.91)$$

so that, for small angles, the resultant component of  $M_t$  in the radial direction is given by  $M_t d\theta$ .

The moment equation of equilibrium for the section in figure 2.17 is, therefore, given by

$$\begin{aligned} & \left(M_r + \frac{dM_r}{dr} dr\right)(r+dr)d\theta - M_r r d\theta - M_t dr d\theta + \\ & (r+dr)\left(Q + \frac{dQ}{dr} dr\right)(r+dr)d\theta - rQr d\theta = 0 \end{aligned} \quad (2.92).$$

Neglecting small terms this reduces to

$$M_r + \frac{dM_r}{dr} r - M_t + Qr = 0 \quad (2.93)$$

where, from equations (2.86) and (2.87),

$$M_r = D \left( \frac{1}{r_r} + \frac{\nu}{r_t} \right) \quad (2.94)$$

$$M_t = D \left( \frac{1}{r_t} + \frac{\nu}{r_r} \right) \quad (2.95).$$

Consideration of figure 2.18 allows the determination of  $M_r$  and  $M_t$  in terms of the vertical displacement,  $w$ , of the plate.

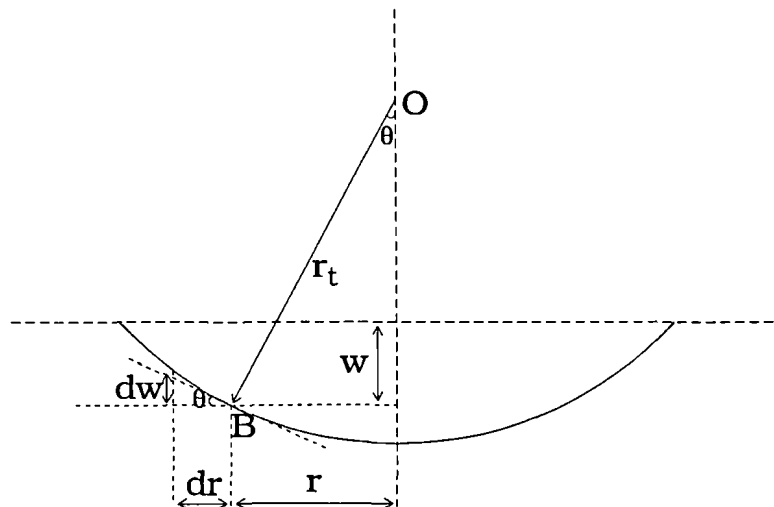


Figure 2.18 Radial curvature of circular 2-d plate.

The downward vertical displacement at a radial distance  $r$  from the centre of the plate is  $w$ , so that the tangent at  $r$  is given by  $\tan\theta = -\frac{dw}{dr}$ . For small deflections the radius of curvature  $r_r$  which lies along OB may, therefore, be determined according to

$$\frac{1}{r_r} = \frac{d\theta}{ds} = -\frac{d^2w}{dr^2} \quad (2.96).$$

The radius of curvature  $r_t$  swings out and back into the plane of the paper describing a cone of radius  $r$  at its base. From figure 2.18,

$$\frac{r}{r_t} = \sin\theta \quad (2.97)$$

and for small angles the approximation that  $\sin\theta = \tan\theta$  holds, yielding the following expression;

$$\frac{1}{r_t} = -\frac{1}{r} \frac{dw}{dr} \quad (2.98).$$

Equation (2.93) may now be written in terms of  $w$ , giving

$$\frac{d^3w}{dr^3} + \frac{1}{r} \frac{d^2w}{dr^2} - \frac{1}{r^2} \frac{dw}{dr} = -\frac{Q}{D} \quad (2.99)$$

which simplifies to

$$\frac{d}{dr} \left( \frac{1}{r} \frac{d}{dr} \left( r \frac{dw}{dr} \right) \right) = -\frac{Q}{D} \quad (2.100).$$

## 2.5 Viscoelasticity

Some materials are fairly complex in their behaviour and not only respond elastically under stress but also respond viscously [14]. These materials of dual behaviour are termed viscoelastic. It is not always apparent whether a viscoelastic material is essentially solid or liquid in character and thus it is necessary to bring to light the main distinguishing features. A viscoelastic liquid flows viscously and extends elastically, and is, therefore, non-Newtonian. A viscoelastic solid exhibits delayed and retarded elasticity under the action of a force, so that only at steady state does Hooke's Law hold.

Mechanical models, comprising springs and dashpots, are used to represent the viscoelastic behaviour in each case.

### 2.5.1 Maxwell model

This model consists of an elastic and viscous component forming a series combination to represent a viscoelastic (or Maxwell) liquid. The combination is depicted in figure 2.19, where the spring of shear modulus  $G$  obeys Hooke's Law and the dashpot of shear viscosity  $\eta$  is Newtonian.

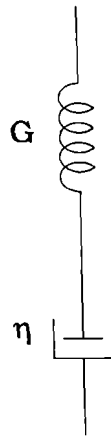


Figure 2.19 Series combination of spring and dashpot.

Thus, the following relationships hold

$$\tau_e = G \gamma_e \quad (2.101)$$

where  $\tau_e$  is the elastic shear stress and  $\gamma_e$  is the shear elastic strain,

and

$$\tau_v = \eta \frac{d\gamma_v}{dt} \quad (2.102)$$

where  $\tau_v$  is the viscous shear stress and  $\frac{d\gamma_v}{dt}$  is the shear viscous strain rate.

Applying a shearing force  $F$  to the body results in a distribution of shear stress  $\tau$  which is experienced by each component. Therefore, in the Maxwell model, the stress-strain relationships become

$$\gamma_e = \frac{\tau}{G} \quad (2.103)$$

and

$$\frac{d\gamma_v}{dt} = \frac{\tau}{\eta} \quad (2.104).$$

The strain resulting from each component is additive and thus the total strain,  $\gamma_t$ , experienced by the viscoelastic liquid is simply the sum of the individual strains.

Therefore,

$$\gamma_t = \gamma_e + \gamma_v \quad (2.105)$$

which yields

$$\gamma_t = \frac{\tau}{G} + \int \frac{\tau}{\eta} dt \quad (2.106).$$

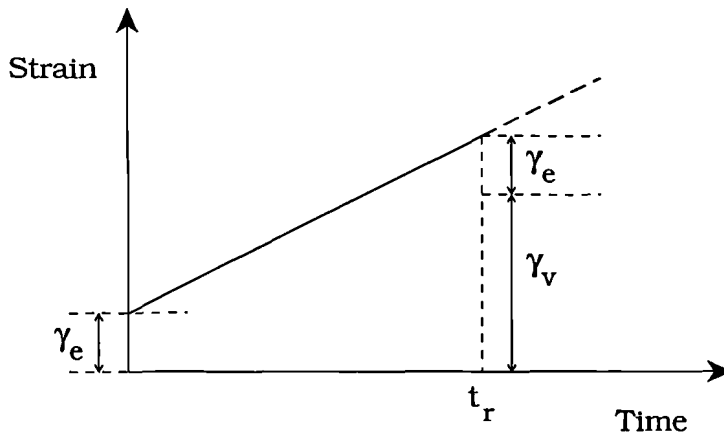


Figure 2.20 Strain versus time for a viscoelastic liquid under constant stress.

The variation of total strain with time under a constantly applied load is depicted in the graph of figure 2.20. The body experiences an initial elastic strain,  $\gamma_e$ , after which flow continues at a constant rate,  $\frac{d\gamma_v}{dt}$ . Any inertia effects have been neglected so that the viscous flow does not accelerate but is instantaneously constant. If the load is removed from the body at any time  $t=t_r$ , such that  $\tau=0$ , then there will be no elastic contribution to the total

strain. In other words, the elastic strain is recoverable upon removal of the load. The instantaneous viscous contribution to the total strain will also be of zero magnitude.

Differentiating the total strain equation (2.106) and multiplying through by  $\eta$  leads to

$$\tau + \frac{\eta}{G} \frac{d\tau}{dt} = \eta \frac{d\gamma_t}{dt} \quad (2.107).$$

If the body is held at constant strain then  $\frac{d\gamma_t}{dt} = 0$  and the solution becomes

$$\tau = \tau_0 e^{\left(-\frac{G t}{\eta}\right)} \quad (2.108)$$

for  $\tau = \tau_0$  at  $t = 0$ .

Thus, it can be seen that the stress in the body relaxes with time; decreasing to zero as  $t$  tends to infinity. Under constant stress  $\frac{d\tau}{dt} = 0$  and, returning to equation (2.107), the material behaves as a Newtonian viscous liquid.

### 2.5.2 Kelvin model

Arranging the spring and dashpot in a parallel combination forms a mechanical representation of a viscoelastic, or Kelvin, solid.

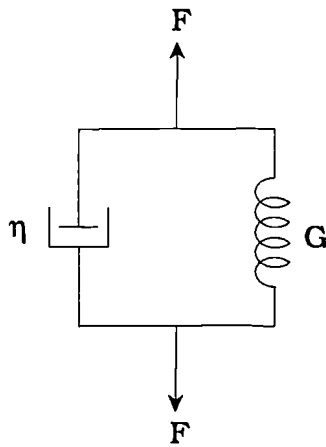


Figure 2.21 Parallel combination of spring and dashpot.

Referring to figure 2.21, the force  $F$  acting on the body causes equal strain in each of the components so that the total stress is the sum of the individual stresses. Thus,

$$\tau_t = \tau_e + \tau_v \quad (2.109)$$

which leads to

$$\tau_t = G\gamma + \eta \frac{d\gamma}{dt} \quad (2.110).$$

Solving for  $\gamma$  gives

$$\gamma = \frac{\tau_t}{G} \left( 1 - e^{-\left(\frac{Gt}{\eta}\right)} \right) \quad (2.111).$$

Under constant stress,  $\tau_o$ , the strain-time diagram is as depicted in figure 2.22, showing a time delay before the elastic strain is reached. Upon removal of the load at  $t=t_r$  the stress equation becomes

$$G\gamma + \eta \frac{d\gamma}{dt} = 0 \quad (2.112)$$

the solution taking the following form

$$\gamma = \gamma_o e^{-\left(\frac{Gt}{\eta}\right)} \quad (2.113)$$

where  $\gamma_o$  is the strain when  $t=0$ .

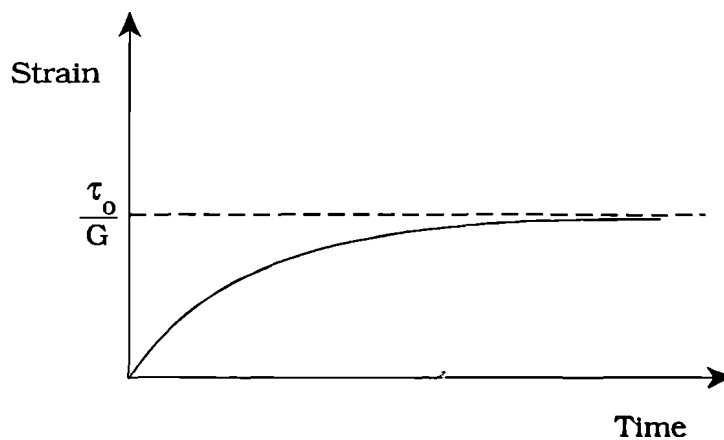


Figure 2.22 Strain versus time for a viscoelastic solid under constant stress.

Hence, the strain does not decrease to zero instantaneously. Instead, the body exhibits a retarded response to the removal of the load, resulting in an exponential decay of the strain as illustrated in figure 2.23.

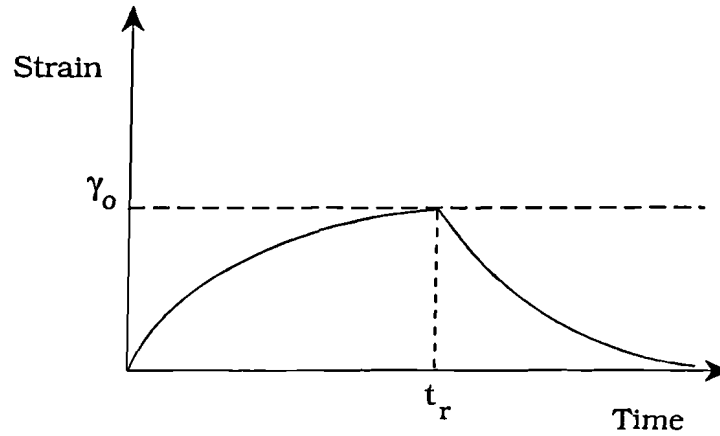


Figure 2.23 Strain of a viscoelastic solid when the load is removed at time =  $t_r$ .

Having established the two most basic viscoelastic representations, models of greater complexity may be created. The components are simply put together like building blocks so that their combination describes the behaviour of a particular viscoelastic material.

### 2.5.3 Three component models

Three component models consist of a parallel combination (Kelvin model) in series with either an elastic spring or a viscous dashpot. The models are portrayed in figures 2.24a and b, respectively. The corresponding strain-time diagrams are represented by figures 2.25a and b, showing in each case the response of the system to the application and removal of a constant load. The total strain is the sum of the strain associated with the elastic/viscous series component and the resultant strain of the parallel combination.

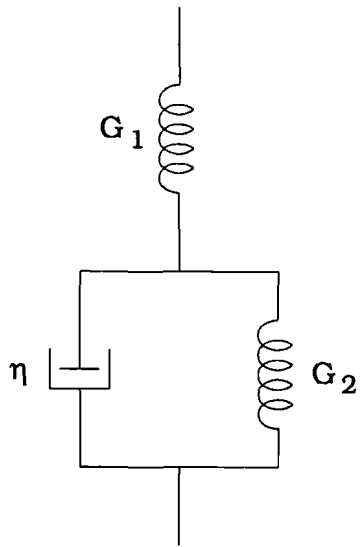


Figure 2.24a

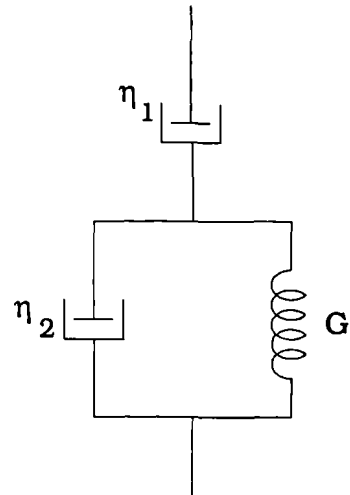


Figure 2.24b

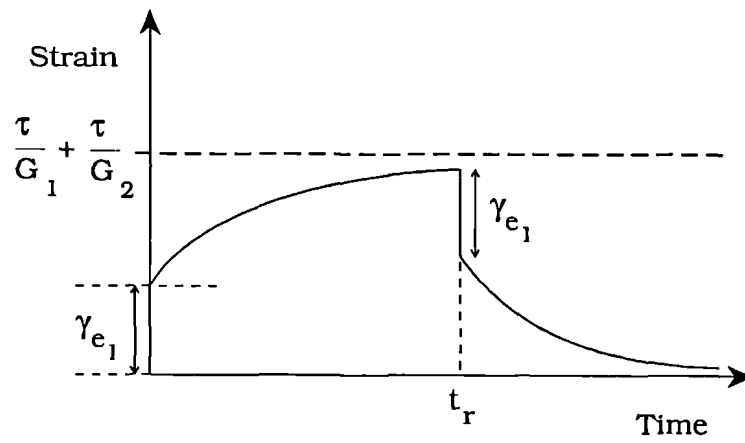


Figure 2.25a Strain versus time for the 3-component model in figure 2.24a.

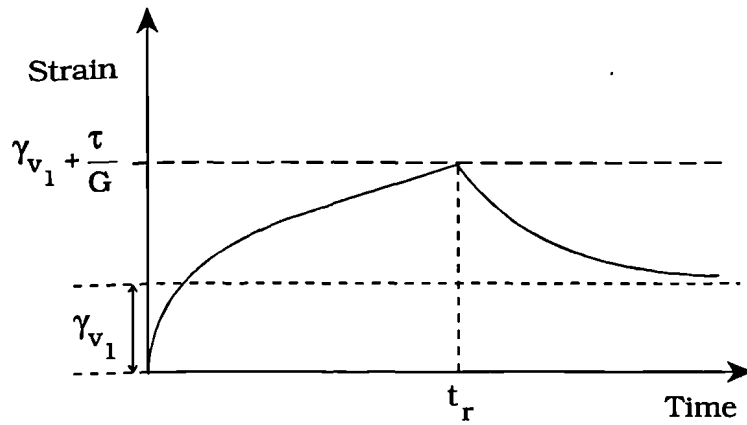


Figure 2.25b Strain versus time for the 3-component model in figure 2.24b.

#### 2.5.4 Four component model

Placing a Maxwell model in series with a Kelvin model constitutes a four component model, as in figure 2.26. Strains are again additive, the stress-time diagram of figure 2.27 depicting the behaviour under a constant load.

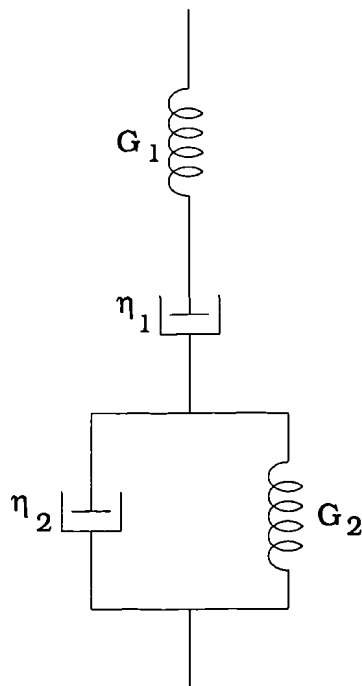


Figure 2.26 A four component model.

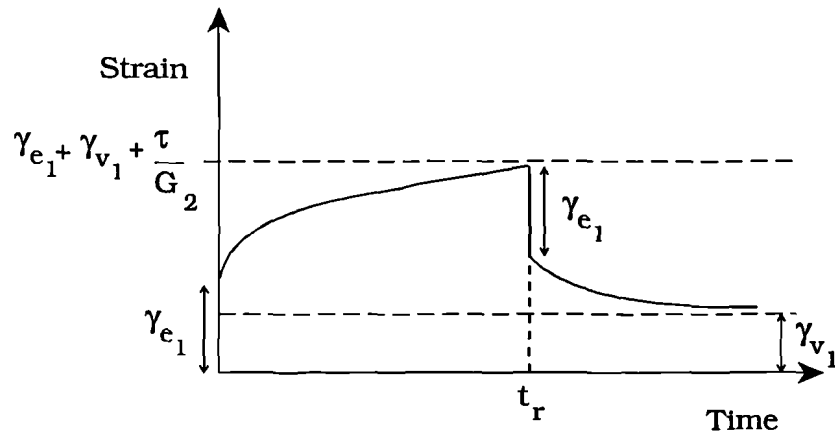


Figure 2.27 Strain versus time for the 4-component model in figure 2.26.

Upon removal of the load in each of the cases illustrated above, only when there exists a series viscous component does the material result in a permanent state of deformation, all forms of elastic strain being recoverable.

## 2.6 References

- [1] B S Massey, *Mechanics of Fluids*, chapter 1, fourth edition, Van Nostrand Reinhold Company, 1979.
- [2] M E O'Neill and F Chorlton, *Ideal and Incompressible Fluid Dynamics*, pp 100, Ellis Horwood Ltd, John Wiley & Sons, 1986.
- [3] M E O'Neill and F Chorlton, *Ideal and Incompressible Fluid Dynamics*, pp 125-130, Ellis Horwood Ltd, John Wiley & Sons, 1986.
- [4] J R Welty, C E Wicks and R E Wilson, *Fundamentals of Momentum, Heat, and Mass Transfer*, pp 121, third edition, John Wiley & Sons, 1984.
- [5] B S Massey, *Mechanics of Fluids*, pp 17, fourth edition, Van Nostrand Reinhold Company, 1979.
- [6] D N Roy, *Applied Fluid Mechanics*, pp 373-375, Ellis Horwood Ltd, John Wiley & Sons, 1988.
- [7] J R Welty, C E Wicks and R E Wilson, *Fundamentals of Momentum, Heat, and Mass Transfer*, pp 123-128, third edition, John Wiley & Sons, 1984.
- [8] M R Spiegel, *Theoretical Mechanics*, Schaum's Outline Series in Science, SI (metric) edition, chapter 9, McGraw-Hill Book Company, 1967.

- [9] S Timoshenko, Strength of Materials, Part I, Elementary Theory and Problems, pp 1-4, third edition, Robert E. Krieger Publishing Company, New York, 1976.
- [10] R J Roarke, Formulas for Stress and Strain, pp 92-97, third edition, McGraw Hill Book Company, Inc, 1954.
- [11] S Timoshenko, Strength of Materials, Part II, Elementary Theory and Problems, pp 76-78, third edition, Robert E. Krieger Publishing Company, New York, 1976.
- [12] S Timoshenko, Strength of Materials, Part II, Elementary Theory and Problems, pp 86-88, third edition, Robert E Krieger Publishing Company, New York, 1976.
- [13] S Timoshenko and S Woinowsky-Krieger, Theory of Plates and Shells, chapter 3, second edition, McGraw-Hill Book Company Inc, 1959.
- [14] Z D Jastrzebski, Nature and Properties of Engineering Materials, pp 184-189, third edition, John Wiley & Sons Inc, 1959.

## **CHAPTER 3**

### **BACKGROUND TO TLM**

The basic concepts of the TLM modelling technique are introduced and discussed with application to both wave and diffusion based problems.

### 3.1 Introduction to TLM

The transmission line matrix (TLM) method is a transient numerical modelling technique which solves problems described by the wave or diffusion equation.

TLM routines are explicit in nature [1] facilitating the incorporation of non linear parameters [2]. The explicitness of the technique easily accommodates boundary conditions whether constant or varying throughout the modelling period [3-6]. Although equations constituting the routines may be expressed in matrix form, there is no lengthy matrix manipulation as found in other modelling techniques. Routines are one step such that calculations only depend upon values stored at the previous time step, or iteration, the iterations themselves requiring very little processing time.

One of the greatest advantages of the technique is that the routines involved are numerically very simple and thus modification of a particular routine does not require great mathematical skill. As a result, development of programs is usually straightforward compared with the initial conceptual interpretation of the problem. Comparison with other techniques readily highlights the simplicity of structure and in particular the simple meshing of a TLM network. This does not mean, however, that bodies of complex geometry pose a challenge for the technique. In fact, TLM has been applied successfully to many different body shapes, up to and including those of three dimensions [2,7-9]. Substructuring in time and space [10,11] allows both accurate modelling of rapidly changing parameters and focussed attention in localised areas respectively. Each is achieved through the explicit nature of the technique and leads to optimum modelling efficiency.

The technique, therefore, is extremely flexible within the confines of its modelling applications.

### 3.2 Applications of the TLM Technique

The basis of the TLM technique was conceived by P B Johns and R L Beurle with their first work being published in 1971 [12,13]. Originally applied to the propagation of electric and magnetic fields the technique provided solutions such as those for waveguide problems in the form of field patterns and determination of resonant frequencies [14,15]. Development of the technique proceeded resulting in the modelling of problems involving inhomogeneous dielectrics and those requiring a three dimensional treatment [14,16,17].

Success in the modelling of wave propagation led to investigation of the applicability of TLM to diffusion problems. A substantial amount of work has been carried out on thermal diffusion, covering a wide variety of problems including heat flow in semi conductor devices and heat transfer in foodstuffs [18-20]. Increased success and knowledge of the method led to more diverse applications such as acoustic wave propagation [21,22], electron diffusion in solar cells [23,24], the soaking behaviour of white rice [25] and fluid network dynamics [26,27]. The theoretical aspects of the TLM technique including accuracy, meshing and stability have been thoroughly addressed [28-32].

### 3.3 TLM Theory

The TLM technique provides a solution for the Telegrapher's equation which takes the following form in two dimensional space [1]:

$$\frac{\partial^2 \Phi}{\partial x^2} + \frac{\partial^2 \Phi}{\partial y^2} = 4 R_d C_d \frac{\partial \Phi}{\partial t} + 2 L_d C_d \frac{\partial^2 \Phi}{\partial t^2} \quad (3.1)$$

where  $\Phi$  represents the potential of the network;

$R_d$  represents the distributed value of resistance;

$C_d$  represents the distributed value of capacitance;

$L_d$  represents the distributed value of inductance.

Clearly, (3.1) models the potential in an electric circuit as a function of both time and space. At first sight the question posed is, "how does this circuit relate to problems in the physical world?". The types of problems appropriate to TLM are those which may be expressed either in the full form of the Telegrapher's equation or in a reduced form. By suitable choice of circuit parameters and magnitude of timestep one or other of the time derivative terms may be assumed negligible, thus reducing the form of the full equation which itself represents a damped wave equation. A circuit with no resistance is modelled by

$$\frac{\partial^2 \Phi}{\partial x^2} + \frac{\partial^2 \Phi}{\partial y^2} = 2 L_d C_d \frac{\partial^2 \Phi}{\partial t^2} \quad (3.2)$$

and is the wave equation.

Choosing the modelling timestep sufficiently small so that  $\frac{\partial^2 \Phi}{\partial t^2} \ll \frac{\partial \Phi}{\partial t}$  yields the diffusion equation [28]:

$$\frac{\partial^2 \Phi}{\partial x^2} + \frac{\partial^2 \Phi}{\partial y^2} = 4 R_d C_d \frac{\partial \Phi}{\partial t} \quad (3.3).$$

Having introduced the switch mechanism to transform the behaviour of the circuit so that either diffusion or wave propagation results, analogies between the circuit and the physical problems can now be established. The diffusion or wave parameters are represented by the electrical components of the relevant circuit so that the potential represents the scalar or field quantity to be determined. Maxwell's equations in two dimensions yield the following equation for the propagation of electromagnetic waves in a medium,

$$\frac{\partial^2 E_z}{\partial x^2} + \frac{\partial^2 E_z}{\partial y^2} = \mu\epsilon \frac{\partial^2 E_z}{\partial t^2} \quad (3.4)$$

where,  $\mu$  is the permeability;

$\epsilon$  is the permittivity;

$E$  denotes the electric field;

and  $E_x = E_y = 0$ .

Comparing equations (3.2) and (3.4) lead to the following equivalences;

$E_z$  and  $\Phi_z$

$\mu$  and  $L_d$

$\epsilon$  and  $2C_d$

(3.5).

From equation (3.4) the wave speed is  $\frac{1}{\sqrt{\mu\epsilon}}$  which is equal to the speed of light,  $c$ , for  $\mu_r = \epsilon_r = 1$  since  $\frac{1}{c^2} = \mu\epsilon = \mu_0\mu_r\epsilon_0\epsilon_r$ . However, the corresponding velocity of propagation in the TLM mesh, from equation (3.2), is  $\frac{1}{\sqrt{2L_dC_d}}$ , where  $L_d$  and  $C_d$  are the inductance and capacitance per unit length respectively. The mesh velocity is, therefore, equal to  $\frac{c}{\sqrt{2}}$  due to the transmission line network representing a medium which has a relative permittivity of twice the free space value [33].

As an example of a diffusion application the thermal diffusion equation is considered, which in two dimensions is given by

$$\frac{\partial^2 T}{\partial x^2} + \frac{\partial^2 T}{\partial y^2} = \frac{\rho C_p}{k_T} \frac{\partial T}{\partial t} \quad (3.6)$$

where,  $T$  is the temperature;

$\rho$  is the density;

$k_T$  is the thermal conductivity;

and  $C_p$  is the specific heat capacity.

Upon comparison with equation (3.3) of the transmission line network the temperature is represented by the network potential and heat flow is modelled by the current. The distributed network and material parameters may be related as follows,

$$\begin{aligned}R_d &= \frac{1}{4k_T} \\C_d &= \rho C_p\end{aligned}\tag{3.7}.$$

It now suffices to reveal the fundamentals of the technique which ultimately provide the solution of the Telegrapher's equation.

### **3.4 Fundamentals of TLM**

The TLM routine operates by passing pulses of information, the magnitude of which being determined by the parameters involved in the particular application. The value of the required field quantity is calculated at points within a body from the information pulses, as and when desired.

The body under consideration is divided into spatial elements such that points of calculation lie at their centres. These points are termed nodes and represent the points of connection of paths along which the information pulses are passed. It is these paths of interconnection which constitute the TLM mesh. The pulses, then, follow a structured route as defined by the mesh which spatially discretises the body. The paths of the TLM mesh are of a finite length and thus the duration of pulse travel between nodes is also finite, yielding temporal discretisation as required in a transient simulation.

The wave and diffusion equations involve the pairs of lumped circuit components L, C and R, C respectively, so that elements take the appearance of the structure in figure 3.1.

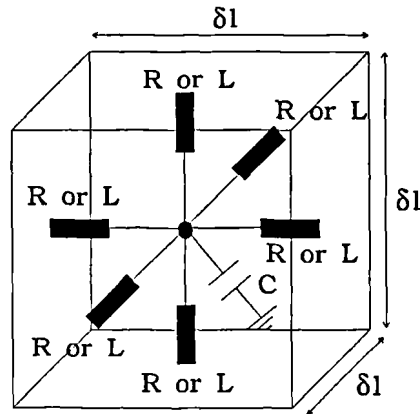


Figure 3.1 A general 3-d cubic lumped circuit element, of spatial dimension  $\delta l$ .

Arranging the components in this way clearly localises the parameter values within each element. This representation, however, effectively isolates nodes from one another in the body so that there is no apparent interconnection. The wave network parameters L and C are related to their distributed values by

$$L = L_d \delta l \text{ and } C = C_d \delta l \quad (3.8)$$

and the diffusion network parameters R and C are related to their distributed values by

$$R = R_d \frac{\delta l}{\delta l^2} \text{ and } C = C_d \delta l^3 \quad (3.9).$$

Returning to circuit theory, the capacitance of a diffusion element can be expressed in terms of impedance by

$$Z = \frac{\delta t}{C} \quad (3.10)$$

thus introducing temporal discretisation theoretically in the model. The capacitor may now be replaced by transmission lines, each of impedance  $Z$ , which in 1-d connect neighbouring nodes. In a two dimensional network each element contains two whole transmission lines so that the impedance is given by  $Z = \frac{2\delta t}{C}$ , the capacitance of the element being divided equally between the lines. Similarly, in three dimensions the impedance of each line is  $Z = \frac{3\delta t}{C}$  [2]. In wave applications the impedance is calculated from the inductance and capacitance, according to

$$Z = \sqrt{\frac{L_d}{C_d}} \quad (3.11).$$

The velocity of the wave on the mesh is given by

$$\frac{\delta l}{\delta t} = \frac{1}{\sqrt{L_d C_d}} \quad (3.12)$$

in a one-dimensional network, and

$$\frac{\delta l}{\delta t} = \frac{1}{\sqrt{2L_d C_d}} \quad (3.13)$$

in a two dimensional network [12,33].

For given values of  $\delta l$ ,  $L_d$  and  $C_d$ , the timestep  $\delta t$  must be chosen so that the velocity of the wave on the mesh is modelled correctly according to equation (3.12) or (3.13) above. When the wave propagation is one dimensional the timestep is given by

$$\delta t = \delta l \sqrt{L_d C_d} = \frac{C}{C_d} \sqrt{L_d C_d} = C Z$$

and is in agreement with equation (3.10).

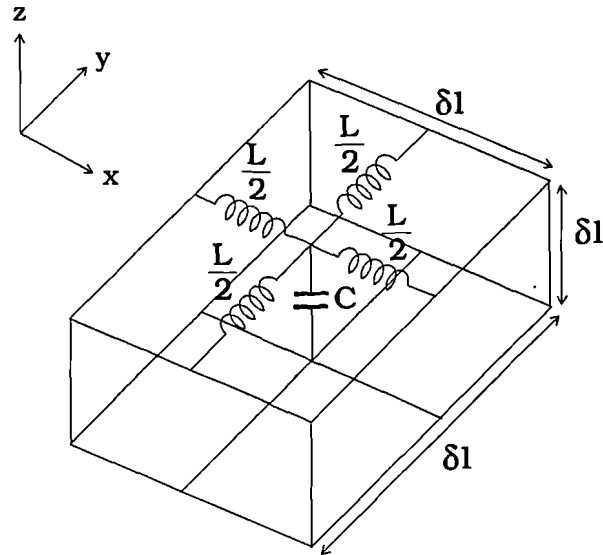


Figure 3.2 Two dimensional LC element.

The equations for the voltage and the current difference at the shunt junction depicted in figure 3.2 are

$$\frac{\partial \Phi_z}{\partial x} = -L_d \frac{\partial I_x}{\partial t}$$

and

$$\frac{\partial \Phi_z}{\partial y} = -L_d \frac{\partial I_y}{\partial t}$$

and

$$\frac{\partial I_x}{\partial x} + \frac{\partial I_y}{\partial y} = 2C_d \frac{\partial \Phi_z}{\partial t}$$

(3.14).

Maxwell's equations, in two dimensions, give

$$\frac{\partial E_z}{\partial x} = \mu \frac{\partial H_y}{\partial t}$$

and

$$\frac{\partial E_z}{\partial y} = -\mu \frac{\partial H_x}{\partial t}$$

and

$$\frac{\partial H_y}{\partial x} - \frac{\partial H_x}{\partial y} = \varepsilon \frac{\partial E_z}{\partial t}$$

where H denotes the magnetic field (3.15).

Comparison of equations (3.14) and (3.15) now yields the following remaining equivalences for equation (3.4) and that of the TLM network,

$$H_x \text{ and } I_y$$

$$H_y \text{ and } -I_x$$

(3.16).

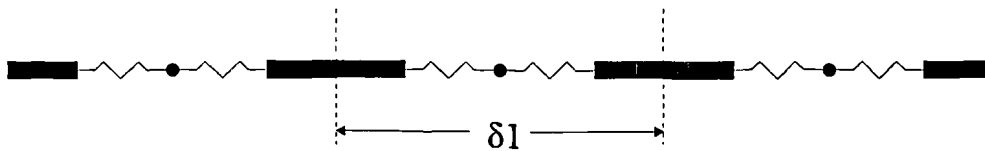


Figure 3.3 A symmetric 1-d nodal structure constituting the TLM mesh.

In figure 3.3 the nodal separation has a constant value of  $\delta l$  and is equivalent to the length of the transmission line and hence the spatial dimension of an element. The elemental boundaries straddle the transmission lines, lying midway along their length.

The paths enabling pulse travel have now been constructed and, as any efficient road network requires a highway code, rules of pulse passing need to be established. Consider a 1-d element as in figure 3.4. The transmission lines connect the element to neighbours on either side. Two pulses are considered initially incident at the node.

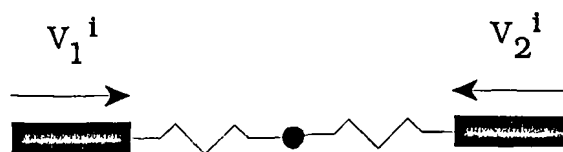


Figure 3.4 Pulses incident at a node.

The arrival of the pulses at the node gives rise to a nodal potential,  $\Phi$ , whereupon instantaneous scattering of the pulses occurs, depicted in figure 3.5, such that the modified pulse values are sent back down the transmission lines. These reflected pulses travel along the lines in one complete timestep heading now in the direction of neighbouring nodes. Once more each pulse will become incident at a node and give rise to a potential. The repeated scattering and passing of pulses in this way illustrates the propagation of pulses along the network.

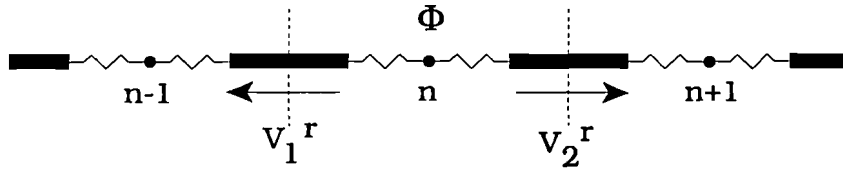


Figure 3.5 Pulses scattered instantaneously towards neighbouring nodes.

In general, all the nodes in a network will have initial incident pulses so that the above behaviour occurs in each element at the same moment in time.

The route taken by the pulses upon scattering may be illustrated by the following connection routine for 1-dimensional propagation, the subscript  $k$  denoting the  $k^{\text{th}}$  time interval.

$$\begin{aligned} {}_{k+1}V^i(n,1) &= {}_kV^r(n-1,2) \\ {}_{k+1}V^i(n,2) &= {}_kV^r(n+1,1) \end{aligned} \tag{3.17}$$

where the first entry within the parantheses denotes the node number and the second entry denotes the branch number.

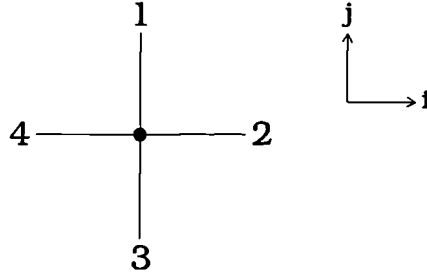


Figure 3.6 Two-dimensional configuration of node branches.

In two dimensions each node has four branches, as depicted in figure 3.6. The connection routine in this case takes the following form,

$$\begin{aligned}
 {}_{k+1}V^i(i,j,1) &= {}_kV^r(i,j+1,3) \\
 {}_{k+1}V^i(i,j,2) &= {}_kV^r(i+1,j,4) \\
 {}_{k+1}V^i(i,j,3) &= {}_kV^r(i,j-1,1) \\
 {}_{k+1}V^i(i,j,4) &= {}_kV^r(i-1,j,2)
 \end{aligned}
 \tag{3.18}$$

The value of the nodal potential and the magnitude of the reflected pulses are determined from the application of Thevenin's Theorem to a TLM node, the details of which being included in Appendix I, yielding

$$\Phi = \frac{2}{R+Z} \frac{\sum_{l=1}^{2d} V_l^i}{\sum_{l=1}^{2d} \frac{1}{R+Z}}
 \tag{3.19}$$

$$V_l^r = \frac{Z}{(R+Z)} \Phi + \frac{(R-Z)}{(R+Z)} V_l^i
 \tag{3.20}$$

where  $d$  represents the dimension of the model.

The reflected pulses may also be expressed in matrix form such that for a 2 dimensional symmetric node:

$$\begin{pmatrix} k+1V_1^r \\ k+1V_2^r \\ k+1V_3^r \\ k+1V_4^r \end{pmatrix} = \frac{1}{2(R+Z)} \begin{pmatrix} 2R-Z & Z & Z & Z \\ Z & 2R-Z & Z & Z \\ Z & Z & 2R-Z & Z \\ Z & Z & Z & 2R-Z \end{pmatrix} \begin{pmatrix} kV_1^i \\ kV_2^i \\ kV_3^i \\ kV_4^i \end{pmatrix} \quad (3.21).$$

For a 2 dimensional wave node (with R=0):

$$\begin{pmatrix} k+1V_1^r \\ k+1V_2^r \\ k+1V_3^r \\ k+1V_4^r \end{pmatrix} = \frac{1}{2} \begin{pmatrix} -1 & 1 & 1 & 1 \\ 1 & -1 & 1 & 1 \\ 1 & 1 & -1 & 1 \\ 1 & 1 & 1 & -1 \end{pmatrix} \begin{pmatrix} kV_1^i \\ kV_2^i \\ kV_3^i \\ kV_4^i \end{pmatrix} \quad (3.22).$$

Not all reflected pulse values are evaluated according to the type of matrix above, that is reflections of pulses may also occur at the boundaries of the mesh, for example, at material interfaces [19]. Consider a body placed in surroundings such that it is heated by constant sources in the ambient.

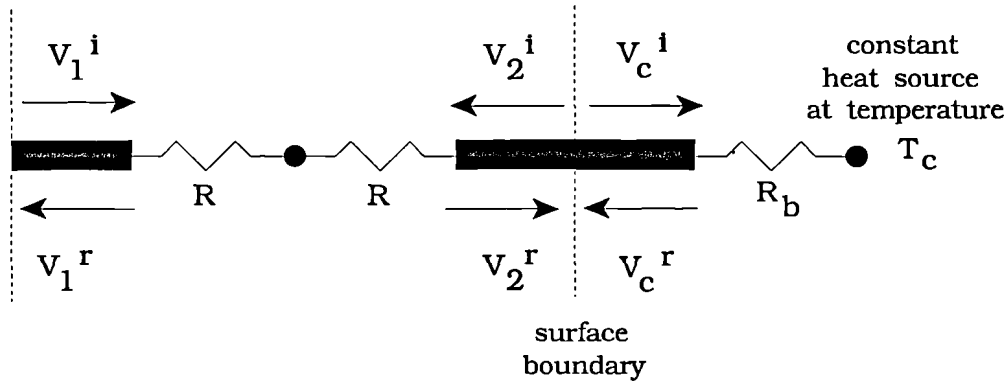


Figure 3.7 Reflected pulses at a boundary.

Figure 3.7 represents the surface boundary arrangement for elements at the surface of the body and those of the ambient. The temperature of the heat source is assumed to be unaffected by the presence of the body, so that V<sub>c</sub><sup>i</sup> does not contribute to its nodal potential. The source supplies heat to the body

at a rate determined by the boundary resistance  $R_b = \frac{1}{h\delta l^2}$  where  $h$  is the heat transfer coefficient. The following the rules of conservation of current across the boundary, as for a general node, leads to

$$V_c^r = \frac{Z}{R_b + Z} T_c + \left( \frac{R_b - Z}{R_b + Z} \right) V_c^i \quad (3.23).$$

The product of heat flow and resistance must equal the temperature drop across the resistor, that is

$$\frac{R_b}{Z} (V^i - V^r) = V^i + V^r - T_c \quad (3.24).$$

If the rate of heat transfer to the body is instantaneous, ie  $R_b = 0$ , then the reflected pulse takes a new form

$$V_c^r = T_c - V_c^i \quad (3.25).$$

If, on the other hand, a zero rate of heat transfer exists, such that the boundary resistor is infinite, then the boundary becomes insulating and the reflected pulse is now given by

$$V_c^r = V_c^i \quad (3.26)$$

denoting a perfect reflection at the boundary.

In the case of electromagnetic waves the reflection at a boundary is dependent upon the type of wall [33]. If voltage represents the electric field then a magnetic wall is represented by an open circuit resulting in total reflection of the pulse value as in equation (3.26), and an electric wall is represented by a short circuit which reflects an identical negative pulse. Conversely, when the voltage represents the magnetic field a magnetic wall is represented by a short circuit boundary and an electric wall is represented by an open circuit boundary.

### 3.5 Initialisation of Pulses

In most thermal problems not only is the body under consideration heated by its surroundings but it will also have an initial temperature which may be uniform or linear across the body. Considering, for simplicity, a uniform temperature distribution, then this can be achieved by applying adiabatic heat sources of the required temperature and heating the body until it reaches the steady state condition so that it assumes the temperature of the ambient. This, however, proves to be time consuming particularly for a 3-d problem and the same result can be achieved much more efficiently by returning to Thevenin's theory. When steady state is reached, such that a uniform potential is achieved throughout the network, the net current flow in the circuit is zero with no net current flow down each branch at every node. Thus, Kirchoff's current law now yields

$$\frac{2 V_1^i - \Phi}{R_1 + Z_1} = \frac{2 V_2^i - \Phi}{R_2 + Z_2} = \dots = \frac{2 V_m^i - \Phi}{R_m + Z_m} = 0 \quad (3.27)$$

from which it can be shown that the solution is

$$V_1^i = V_2^i = \dots = V_m^i = \frac{\Phi}{2} \quad (3.28).$$

Thus, setting all incident pulse values, including those of the stubs which will be discussed later in this chapter, to half the value of the required initial nodal potential initialises the mesh uniformly and instantaneously.

### 3.6 Generation of Current and Current Loss

In some bodies chemical reactions, or changes of state, occur which in turn affect the temperature profile by altering the rate of heat transfer within the body. These body effects actually alter the rate of heat transfer indirectly

via a direct generation of heat into the body or via a direct heat loss from the body.

In a diffusion network an increase, or surge, of current can be represented by a current generator attached to the appropriate node [34] as shown in figure 3.8.

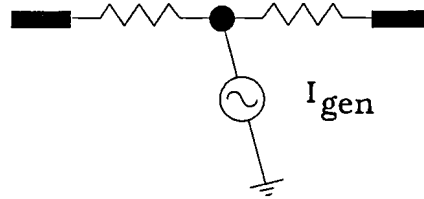


Figure 3.8 Current generator attached to TLM node.

The nodal potential equation takes the generated current into account as follows,

$$\Phi = \frac{\left( \frac{2}{R + Z} \sum_{l=1}^{2d} V_l i + I_{gen} \right)}{\sum_{l=1}^{2d} \frac{1}{R + Z}} \quad (3.29)$$

where  $d$  represents the spatial dimension of the node.

Current loss can similarly be represented by a negative current generator or, alternatively, as charge dissipated through a resistor [35] depicted in figure 3.9.

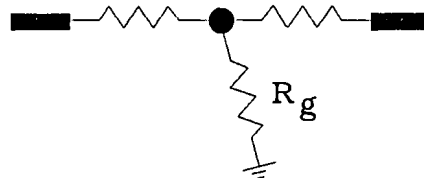


Figure 3.9 Resistor dissipates charge from node.

The additional resistance in the network affects the impedance at the node according to

$$\Phi = \frac{\frac{2}{(R + Z)} \sum_{l=1}^{2d} V_l^i}{\left( \sum_{l=1}^{2d} \frac{1}{R + Z} + \frac{1}{R_g} \right)} \quad (3.30).$$

Examples of effects modelled in this way include evaporation and recondensation of moisture which causes cooling and heating of a body respectively, and also chemical exothermic and endothermic reactions.

Losses in wave propagation, such as attenuation, are generally accounted for by use of stub transmission lines and are discussed in section 3.8.

### 3.7 Variation of Parameters in a Diffusion Network

#### 3.7.1 Variation in resistance

Thus far the TLM technique has been shown to apply only to a homogeneous and isotropic material such that the elements in the network model the same parameters and the nodes are symmetric.

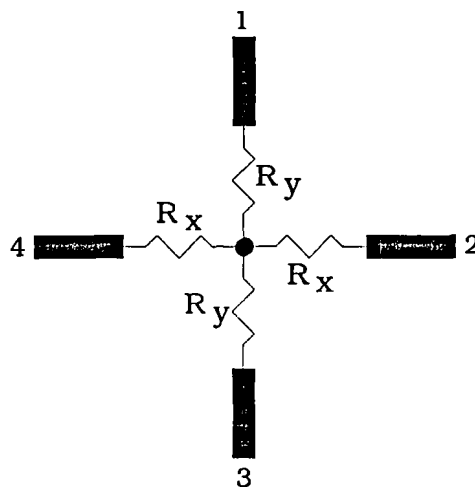


Figure 3.10 An asymmetric 2-d node representing an anisotropic material.

Consider an anisotropic material such that the parameter modelled by the resistance takes a different value in the x direction from that in the y direction. The structure of a TLM node now resembles that in figure 3.10 and the nodal potential equation becomes [36]:

$$\Phi = \left( \left( \frac{2(V_1^i + V_3^i)}{(R_y + Z)} \right) + \left( \frac{2(V_2^i + V_4^i)}{(R_x + Z)} \right) \right) \left( \frac{1}{\sum_{l=1}^d \frac{1}{R_x + Z} + \sum_{l=1}^d \frac{1}{R_y + Z}} \right) \quad (3.31).$$

Thus, a spatial variance in the resistance, either from one element to another or within the element itself, is easily accommodated.

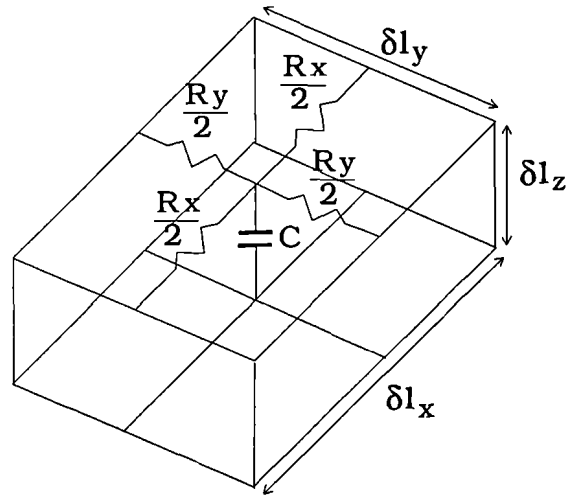


Figure 3.11 Asymmetric RC element.

Similarly, asymmetry in the dimensions of the element, as in figure 3.11, can be easily accommodated since,

$$R_x = R_{dx} \frac{\delta l_x}{\delta l_y \delta l_z} \quad \text{and} \quad R_y = R_{dy} \frac{\delta l_y}{\delta l_x \delta l_z} \quad (3.32)$$

where  $R_{dx}$  and  $R_{dy}$  are the distributed values of resistance in the x and y directions respectively. The volume modelled by the capacitance is now  $\delta l_x \delta l_y \delta l_z$ .

Temporal changes in the resistance of the network are accounted for simply by altering the value of the resistors at the appropriate iteration before the arrival of incident pulses at the node [37].

### 3.7.2 Variation in capacitance

Changes in the capacitance of the mesh occur either as a result of a varying parameter or because adjacent elements have different volumes. Consider, for example, a segment as shown in figure 3.12.

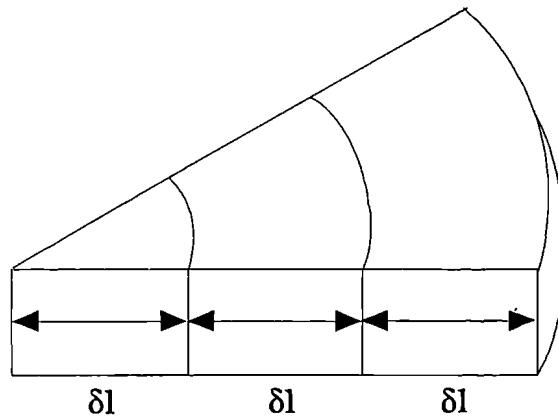


Figure 3.12 Segment consisting of elements of unequal volume.

Although the nodal separation is of a constant value throughout, the volume represented by each element increases towards the outer edge of the segment.

Local increases in capacitance may be modelled in terms of a stub transmission line placed at the relevant nodes in the network, as illustrated in figure 3.13. In this way the transmission lines linking nodes model the minimum capacitance of the network and the open circuit stub line models any additional capacitance. Thus, the total capacitance of an element is divided

into the link lines and the stub line, the link lines carrying the same characteristic impedance throughout the network [2,18,36].

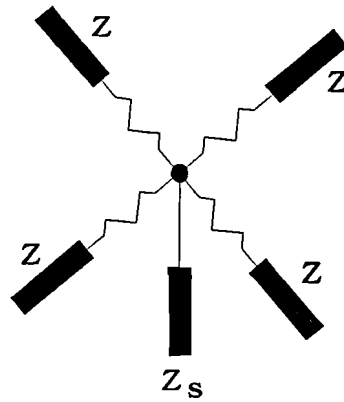


Fig 3.13 A 2-d TLM node with stub.

A voltage pulse travelling from the node along an open circuit stub transmission line will return to be incident at the same node a time interval  $\delta t$  later. Hence the impedance is given by

$$Z_s = \frac{\delta t}{2} \frac{1}{C_s} \quad (3.33)$$

where  $C_s$  is the additional capacitance modelled by the stub, such that

$$C_s = C_{\text{element}} - C_{\text{min}} \quad (3.34).$$

Clearly, from the above determination of  $Z_s$  time synchronisation of the pulse scattering is maintained. The presence of the stub is purely to provide an additional storage mechanism so that the reflected pulse returns the unmodified incident pulse. Therefore, the stub line is connected directly to the node and not via a resistor as in the case of the link lines.

The nodal potential equation for a node such as that in figure 3.13 must be modified to incorporate the stub as follows [2],

$$\Phi = \left( \frac{2}{(R+Z)} \sum_{l=1}^{2d} V_l^i + \frac{2V_s^i}{Z_s} \right) \left( \frac{1}{\sum_{l=1}^{2d} \frac{1}{R+Z} + \frac{1}{Z_s}} \right) \quad (3.35)$$

and the reflected pulse travelling along the stub is calculated according to

$$V_s^r = \Phi - V_s^i \quad (3.36).$$

Temporal changes in the capacitance and hence stub impedance must be accompanied by conservation of current flow across the stub. If the value of the stub impedance is altered before the incident pulse arrives at the node, then a new incident pulse value must be calculated so that current is conserved [22].

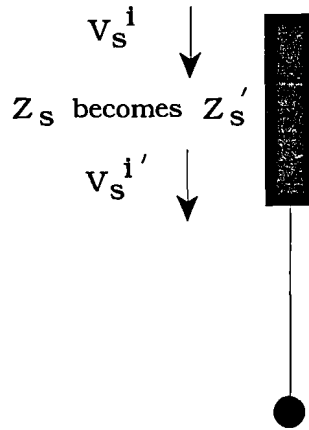


Figure 3.14 Conservation along a stub.

Thus, if in figure 3.14  $V_s^{i'}$  and  $Z_s'$  denote the values of the incident pulse along the stub and the stub impedance after a change of parameters then

$$\frac{V_s^{i'}}{Z_s'} = \frac{V_s^i}{Z_s} \quad (3.37)$$

allowing recalculation of the incident pulse  $V_s^{i'}$ .

### 3.8 Variation of Parameters in a Wave Network

From equation (3.5) a change in permittivity between materials is represented by the associated change in capacitance, and hence admittance, of the two separate networks. The velocity of an electromagnetic wave is dependent upon the permittivity so that each network models a different velocity. Modelling the two materials on one network requires that the characteristic impedance of the link lines be constant throughout. However, in order that the network reflects the difference in propagational velocity as the wave travels through the two different media, open circuit stubs must be incorporated into the part of the network yielding the slower velocity. The stubs have an admittance, which is the inverse of impedance, of  $Y_o$  such that for a two dimensional network the total shunt capacitance at each node is given by [16],

$$2C\delta l \left( 1 + \frac{Y_o}{4} \right) \quad (3.38).$$

The 2-d scattering matrix now takes the following form,

$$\begin{pmatrix} {}_{k+1}V_1^r \\ {}_{k+1}V_2^r \\ {}_{k+1}V_3^r \\ {}_{k+1}V_4^r \end{pmatrix} = \frac{1}{Y_o+4} \begin{pmatrix} -(Y_o+2) & 2 & 2 & 2Y_o \\ 2 & -(Y_o+2) & 2 & 2Y_o \\ 2 & 2 & -(Y_o+2) & 2Y_o \\ 2 & 2 & 2 & (Y_o-4) \end{pmatrix} \begin{pmatrix} {}_kV_1^i \\ {}_kV_2^i \\ {}_kV_3^i \\ {}_kV_4^i \end{pmatrix} \quad (3.39).$$

If the voltage of the wave represents the magnetic field then a change in permeability is modelled by the impedance of the stub lines. However, when the voltage represents an electric field changes in permeability modelled as admittance stubs yield an impedance mismatch [16], and must be rectified by introducing transmission and reflection coefficients at the material boundary which incorporate the ratio of the intrinsic impedances. For example, consider a medium of wave velocity  $v_1 = \frac{1}{\sqrt{\mu_o \epsilon_o}}$  and a second medium in which the

velocity is  $v_2 = \frac{1}{\sqrt{\mu\varepsilon_0}} = \frac{1}{\sqrt{\mu_0\mu_r\varepsilon_0}} = \frac{v_1}{\sqrt{\mu_r}}$ . If the potential of the

network represents the magnetic field then  $\mu_r = 1 + \frac{Z_0}{4}$  where  $Z_0$  is the

impedance of the stub, and the intrinsic impedance of the second medium is

$$Z_2 = \sqrt{\frac{L_d}{C_d}} = \sqrt{\frac{\mu_0}{\varepsilon_0}} \sqrt{\mu_r} = Z_1 \sqrt{1 + \frac{Z_0}{4}}. \quad \text{If the potential of the}$$

network represents the electric field then because the stub now models changes

in admittance it follows that  $\mu_r = 1 + \frac{Y_0}{4}$  so that the impedance of the second

$$\text{medium is } Z_2 = \frac{Z_1}{\sqrt{1 + \frac{Y_0}{4}}} \text{ which is clearly not in agreement with } Z_2$$

above. A similar problem is encountered when modelling changes in permittivity using the magnetic field representation.

Spatial variation in the dimensions of elements lead to velocity changes in the mesh which may, again, be accomplished by the use of stubs so that time synchronisation is maintained or, alternatively, by the use of discontinuous link lines, the impedance of which represents the change in element size [7,22].

Attenuation is the reduction in amplitude of a wave and is represented as a loss that is distributed continuously along the lines of the mesh [38]. A loss stub extracts energy from the node each timestep, behaving essentially the same as a resistor connected to earth in the diffusion application, and may be used to model losses in inhomogeneous materials [39].

### 3.9 References

- [1] P B Johns, "A Simple Explicit and Unconditionally Stable Numerical Routine for the Solution of the Diffusion Equation", *Int J Num Meth Engng*, vol 11, pp 1307-1328, 1977.
  
- [2] S H Pulko and P B Johns, "Modelling of Thermal Diffusion in Three Dimensions by the Transmission Line Matrix Method and the Incorporation of Non-Linear Thermal Properties", *Comms Appl Num Meths*, vol 3, pp 571-579, 1987.
  
- [3] J A Morente, J A Porti and M Khalladi, "Absorbing Boundary Conditions for the TLM Method", *IEEE Trans MTT*, vol 40, no 11, pp 2095-2099, 1992.
  
- [4] S H Pulko, W A Green and P B Johns, "An Extension of the Application of Transmission Line Modelling to Thermal Diffusion to Include Non-Infinite Heat Sources", *Int J Numer Meths in Engng*, vol 24, pp 1333-1341, 1987.
  
- [5] S H Pulko and A O Olashore, "Modelling of Heat Transfer from Fluid Sources using the TLM Technique", *Int J Mod and Sim*, vol 9, pp 96-100, 1989.
  
- [6] G Butler and P B Johns, "The Solution of Moving Boundary Heat Problems Using the Method of Numerical Analysis", in *Numerical Methods in Thermal Problems*, R W Lewis and K Morgan (Eds), Pineridge Press, Swansea, pp 189-195, 1979.

- [7] D A Al-Mukhtar and J E Sitch, "Transmission line matrix method with irregularly graded space", IEE Proc, vol 128, pt H, no 6, pp 299-305, 1981.
  
- [8] P B Johns, "Application of the Transmission Line Matrix Method to Homogeneous Waveguides of Arbitrary Cross-Section", Proc Inst Elec Eng, vol 119, no 8, pp 1086-1091, Aug, 1972.
  
- [9] D H Choi and W J R Hoefler, "The Simulation of 3-Dimensional Wave Propagation by a Scalar TLM Model", in IEEE MTT Int Microwave Symp Dig, May, 1984.
  
- [10] S H Pulko, I A Halleron and C P Phizacklea, "Substructuring of Space and Time in TLM Diffusion Applications", Int J Num Mod: Electronic Networks, Devices and Fields, vol 3, pp 1-8, 1990.
  
- [11] S H Pulko, A Mallik, R Allen and P B Johns, "Automatic Timestepping in TLM Routines for the Modelling of Thermal Diffusion Processes", Int J Num Mod: Electronic Networks, Devices and Fields, vol 3, pp 127-136, 1990.
  
- [12] P B Johns and R L Beurle, "Numerical solution of 2-dimensional scattering problems using a transmission-line matrix", Proc IEE, vol 118, no 9, pp 1203-1208, 1971.
  
- [13] P B Johns, "A New Mathematical Model to Describe the Physics of Propagation", The Radio Electronic Engineer, vol 44, no 12, pp 657-666, 1974.

- [14] S Akhtarzad and P B Johns, "Solution of Maxwell's equations in three space dimensions and time by the tlm method of numerical analysis", Proc IEE, vol 122, no 12, pp 1344-1348, 1975.
- [15] S Akhtarzad and P B Johns, "Numerical Solution of Lossy Waveguides: TLM Computer Program", Electronics Letters, vol 10, pp 309-310, 1974.
- [16] P B Johns, "The solution of inhomogeneous waveguide problems using a transmission-line matrix" , IEEE Transactions on microwave theory and techniques, vol MTT-22, no 3, pp 209-215, 1974.
- [17] S Akhtarzad and P B Johns, "Solution of 6-Component Electromagnetic Fields in 3 Space Dimensions and Time by the TLM Method", Electron Lett, vol 10, no 25/26, pp 535-537, Dec, 1974.
- [18] D de Cogan and A K Shah, "Stub TLM Modelling of Heat Flow in Semiconductor Devices", J Phys D: Appl Phys, vol 19, pp 721-725, 1986.
- [19] P B Johns and S H Pulko, "Modelling of Heat and Mass Transfer in Foodstuffs", Food Structure and Behaviour: Equilibrium and Non-equilibrium Aspects, J Blanchard and P Lillford (Eds), Academic Press, New York, 1986.
- [20] D de Cogan and M Henini, "TLM Modelling of the Thermal Behaviour of Conducting Films on Insulating Substrates", J Phys D: Appl Phys, vol 20, pp 1445-1450, 1987.

- [21] E A Orme, P B Johns and J M Arnold, "A Hybrid Modelling Technique for Underwater Acoustic Scattering", *Int J Num Mod: Electronic Networks, Devices and Fields*, vol 1, pp 189-206, 1988.
- [22] A M Saleh and P Blanchfield, "Analysis of Acoustic Radiation Patterns of Array Transducers Using the TLM Method", *Int J Num Modelling: Electronic Networks, Devices & Fields*, vol 3, pp 39-56, 1990.
- [23] S H Pulko, N M Pearsall and J Winckler, " 'First-Generation' Model of the Indium Tin Oxide-Indium Phosphide Solar Cell", *Proceedings of Optical Materials Technology for Energy Efficiency and Solar Energy Conversion VII*, vol 1016, pp 78-83, SPIE, 1988.
- [24] S H Pulko and N M Pearsall, "A Diffusion Based Model of a Solar Cell", *Proc Seventeenth IASTED Int Symp: Simulation and Modelling*, pp 230-233, June, 1989.
- [25] M Hendrickx, C Engels, P Tobback and P B Johns, "Transmission Line Modelling (TLM) of Water Diffusion in White Rice", *J Food Eng*, vol 5, pp 269-285, 1986.
- [26] R F Boucher and E E Kitsios, "Simulation of Fluid Network Dynamics by Transmission Line Modelling", *Proc Instn Mech Engrs*, vol 200, no C1, pp 21-29, 1986.
- [27] E E Kitsios and R F Boucher, "Transmission Line Modelling of a Hydraulic Piston Control System", *Proc Instn Mech Engrs*, vol 200, no B4, pp 229-236, 1986.

- [28] P Johns and G Butler, "The Consistency and Accuracy of the TLM Method for Diffusion and its Relationship to Existing Methods", *Int J Num Meths Engng*, vol 19, pp 1549-1554, 1983.
- [29] H Meliani, D de Cogan and P B Johns, "The Use of Orthogonal Curvilinear Meshes in TLM Models", *Int J Num Mod: Electronic Networks, Devices and Fields*, vol 1, pp 221-238, 1988.
- [30] J D Austin and S H Pulko, "The Use of General Curvilinear Orthogonal Meshes in TLM Heat Conduction Models", *Numerical Heat Transfer, Part B*, vol 24, pp 107-125, 1993.
- [31] X Gui, P W Webb and D de Cogan, "An Error Parameter in TLM Diffusion Modelling", *Int J Num Modelling: Electronic Networks, Devices and Fields*, vol 5, pp 129-137, 1992.
- [32] A J Wilkinson, S H Pulko and A R M Witwit, "A Discrete State Space View of TLM", *Proc Ninth IASTED Int Symp: Modelling, Identification and Control*, pp 453-456, February, 1990.
- [33] W J R Hoefler, "The Transmission-Line Matrix Method - Theory and Applications", *IEEE Transactions on Microwave Theory and Techniques*, vol MTT-33, no 10, pp 882-893, October, 1985.
- [34] A I Hurst and S H Pulko, "TLM Treatments of Changes of Phase", *Int J Num Modelling: Electronic Networks, Devices and Fields*, vol 7, pp 201-207, 1994.

- [35] X Gui, G-B Gao and H Morkoc, "Transmission-Line Matrix Method for Solving the Multidimensional Continuity Equation", *International Journal of Numerical Modelling: Electronic Networks, Devices and Fields*, vol 6, pp 233-236, 1993.
- [36] S H Pulko, A Mallik and P B Johns, "Application of Transmission Line Modelling (TLM) to Thermal Diffusion in Bodies of Complex Geometry", *Int J Num Meths Engng*, vol 23, pp 2303-2312, 1986.
- [37] S H Pulko and C P Phizacklea, " A Thermal Model for Cyclic Glass Pressing Processes using Transmission Line Modelling", *Proc Instn Mech Engrs*, vol 205, pp 187-194, 1991.
- [38] W J R Hoefler, "The Transmission Line Matrix (TLM) Method", in *Numerical Techniques for Microwaves and Millimeter Wave Passive Structures*, T Itoh (Ed), John Wiley & Sons, 1989.
- [39] S Akhtarzad and P B Johns, "Generalised Elements for TLM Method of Numerical Analysis", *Proc Inst Elec Eng*, vol 122, no 12, pp 1349-1352, Dec, 1975.

## **CHAPTER 4**

### **FIRING OF VITREOUS CLAYS**

Details of the physical and chemical properties of whiteware are reviewed in this chapter. The different stages of the firing process and their effect upon clay are also examined.

## **4.1 Introduction**

Clay has been exploited since 15000 BC to provide robust articles suitable for daily use [1]. The natural properties of wet clay allow it to be moulded easily and hence formed into complex shapes. Moreover, application of heat transforms the clay into a material which is suitable for the manufacture of a wide variety of ware. Clay exhibits a variety of physical characteristics that are dependent upon the mineralogical composition. The diverse range of mineral properties leads to high industrial demand not only in the ceramics industry but also in such areas as agriculture, medicine, plastics and rubber manufacture.

Prior to the eighteenth century, pottery was manufactured from local deposits producing red coloured articles. The discovery of china clay, yielding white coloured articles, initiated the whiteware industry. Development of porcelain, bone china and earthenware rapidly followed spawning the tableware industry. In the nineteenth century demands for improved sanitation fortuitously spurred the growth of the sanitary ware industry.

An important objective of the ceramics industry is to reproduce design ware reliably upon demand. Consequently, intimate knowledge of a particular clay body's constituents and the ensuing reactions during firing is advantageous when attempting to predict successful designs.

## **4.2 Whiteware Systems**

A whiteware body is composed of three main constituents: clay, flux and filler. A typical percentage analysis for sanitary ware is tabulated below.

Clay	Flux	Filler
china clay 23%	felspar 20%	quartz 33%
ball clay 24%		

Table 4.1 Typical sanitary ware composition [1].

#### 4.2.1 Clay

Depending upon origin, clays are generally classified as either primary or secondary. Primary clays are located within the vicinity of the original rocks from which they were formed, whilst secondary clays have been transported by rivers and deposited at locations remote from the formation site. Both types of clay were originally formed when granite rock, containing the mineral felspar, was exposed to superheated steam and hot acidic gases escaping from within the earth's crust. This process caused a partial decomposition of the felspar resulting in the formation of china clay. Normal weathering can also induce decomposition but unfortunately the presence of iron impurities accompanies this present day formation mechanism. Iron impurities are undesirable in that they lead to a colour cast, usually brown, red or pink, upon firing. However, the presence of some impurities can produce effects of significant technical importance such as resistance to stoneware corrosion and the translucency of porcelain. Lime (calcium carbonate) is a particularly important impurity as its addition to china clay causes a reduction in firing shrinkage and at the same time increases the strength of the body thereby elevating the maximum firing temperature of the ware [2].

Kaolinite exists in crystalline form and as a consequence does not exhibit plasticity [3]. Ball clays, however, exhibit a high degree of plasticity. These clays are formed from thick layer deposits of secondary china clay and contain organic material as a result of the transportation process. During firing

most of this organic material is burned out and the residual matter aids the development of plasticity. The fine grain size and the crystal layer arrangement, which entraps layers of water, further enhance plasticity. Ball clays, when added to pure china clay, impart both strength and plasticity to an article improving the shaping properties. Although originally dark in colour, ball clays 'burn' white and are therefore a particularly desirable additive to the china bodies. Furthermore, the physical and chemical properties of a clay body can be tailored by controlling the talc, feldspar and quartz mineral content. The sanitary ware industry in particular exploits these properties to produce bodies that are resistant to cracking of both the clay and glaze. In addition, fired strength, whiteness and very low porosity, in the interest of hygiene, are also highly desirable properties.

#### 4.2.2 Flux

During firing at high temperatures, clays vitrify and form a limited amount of glass which in its liquid state seals the crystalline structure. Unfortunately, typical vitrification temperatures exceed those used in practical commercial kilns. The addition of fluxing material reduces the vitrification temperature and introduces control over the formation of glass. Feldspar is an important fluxing agent as it exhibits a significant difference between its softening and melting points. Potash and soda feldspars are commonly used fluxing agents each supplying a large proportion of alkali which induces the vitrification process at a lower temperature. Nepheline syenite ( $\text{Na}_2\text{OAl}_2\text{O}_3\cdot 2\text{SiO}_2$ ) is exploited by the sanitary ware industry as it yields a significant fluxing action due to high alkali content, despite containing less silica than the feldspars.

### **4.2.3 Filler**

Fillers are employed to form a rigid skeletal structure within the ceramic body. An ideal filler remains inert at low temperatures whilst at high temperatures will produce a highly viscous liquid. A practical and cost effective filler is silica which can be found in abundance as quartz, sand or flint. Crystalline quartz is employed by the sanitary ware industry to increase thermal expansion during firing, offsetting the overall shrinkage. If the particle size is sufficiently small then silica may also be exploited as a fluxing agent.

### **4.3 The Firing Process**

The firing of clay articles is fundamental to the manufacture of ceramic ware, imparting strength and permanent shape to the bodies. A variety of commercial kilns have been designed for this process, each with unique specifications dependent upon the type of article to be fired. The simultaneous achievement of article quality and kiln efficiency is greatly beneficial to the ceramic industry. During firing thermal stresses are induced within the ware and if excessive cause cracking and possibly fracture. Consequently, kiln design must allow careful control of the heating rate if such failures are to be avoided. In addition, energy consumption is of prime importance to the manufacturer and therefore kiln efficiency must be optimised to keep costs low.

During firing the effect of heat causes physical changes in the mineralogical composition which are accompanied by chemical reactions. These result in physical and structural modifications of the clay. The chemical effects give rise to exothermic and endothermic reactions and consequently the temperature profile of the kiln must be tailored accordingly. The firing process consists of five major stages [1], each of which must be carefully

controlled to ensure completion of all chemical changes and their associated thermal reactions.

#### **4.3.1 Smoking**

Temperature range: 150°C - 300°C.

Prior to firing clay articles are left to dry by evaporation at room temperature. At such low temperatures water molecules remain trapped between the interstitial layers of the clay. If fired in this condition the clay body would crack due to the increase in internal pressure as the trapped water molecules vaporize. To prevent this cracking mechanism the clay articles are subjected to a gradual temperature increase in a well ventilated environment. This process of driving off the remaining water is termed smoking.

#### **4.3.2 Pre-heating**

Temperature range: 300°C - 800°C.

This stage is employed to initiate the decomposition of the constituent minerals which induces chemical and physical changes within the clay body. Mineral decomposition expels chemically bonded water, carbon dioxide and sulphur dioxide. It is essential that this process is completed before vitrification occurs when the surface pores become sealed. Incomplete oxidation of carbonaceous material prevents the oxidation of iron and sulphur so that the trapped gases cause bloating and discolouring of the ware. During this stage thermal expansion of the free silica occurs, at a temperature of 573°C. If the heating rate is not controlled sufficiently then the ware may be subjected to cracking or dunting as it is commonly known.

### **4.3.3 Full fire stage**

Temperature range: 800°C - max°C (in the region of 1200°C).

This process continues the reactions of the previous stage but at an increased temperature and heating rate. The maximum firing temperature dictates the quantity of silica entering the liquid phase.

### **4.3.4 Finishing stage**

Temperature range: max°C.

"Soaking" the ware at the maximum temperature for an extended duration allows all the chemical reactions and physical changes to reach completion. Overheating at this stage may lead to distortion and colour defects.

### **4.3.5 Cooling**

Temperature range: max°C - room temperature.

Articles are cooled rapidly from the maximum temperature through the crystallisation zone to 900°C. This steep temperature gradient is employed to prevent the highly vitreous materials from crystallising. Once the crystallisation zone has been transcended the ware is cooled at a slower rate to room temperature. In general, the firing process causes an increase in the amount of free silica present within the clay body and, therefore, an increased probability of dunting and crazing of the glaze. Consequently, a controlled cooling rate is essential if these effects are to be prevented.

## **4.4 Changes of State**

The conversion of a ceramic body at high temperatures from a solid to a liquid state is a gradual process consisting of four stages; solid, sintered, vitrified and fused liquid. A standard firing process employs the first three stages, avoiding the fused liquid stage so as to prevent excessive deformation.

### **4.4.1 Sintering**

The process of sintering occurs at a temperature which is approximately six tenths of that in degrees Celsius at which the body reaches its liquid state. Strength is imparted to the body as particles bond to form larger crystals of the same crystallographic structure. The bulk density of the body increases as a result of the compaction process and is accompanied by a reduction in porosity. Sintering, therefore, produces hard, dense bodies when fired at temperatures well below the liquidus temperature. The three distinct stages of sintering are as follows [4]:

#### **(i) Initial Phase**

Pores form an interconnected network throughout the material.

#### **(ii) Intermediate Phase**

Pores are still interconnected and densification is accompanied by crystal growth.

#### **(iii) Final Phase**

Pores are no longer connected and shrinkage of closed pores occurs. The porosity remains low at a value less than approximately 10%. Densification ceases but crystal growth continues.

#### **4.4.2 Vitrification**

Vitrification normally occurs at the onset of densification, typically 900°C, and continues up to the melting point of the body under consideration. The temperature at which vitrification commences can be controlled by the compositional content of mullite in the body; an increase of mullite content raises the starting temperature [5]. During vitrification the process of densification continues aided by the development of a viscous liquid phase at the crystal interfaces. Crystals grow in size as the small crystals dissolve and later reprecipitate upon larger crystals. The formation of a viscous liquid provides a bond for the material, most of which is still in its solid state, and thus imparts strength to the body. The increase in strength and durability are accompanied by a decrease in porosity as the viscous liquid penetrates the open pores. Firing shrinkage also occurs during vitrification as the body moves towards its equilibrium state, the high surface tension of the viscous fluid drawing the particles of clay together.

Vitrification must be completed before significant deformation of the body occurs under its own weight. Varying the concentration of alumina and alkali impurities varies the viscosity of the liquid phase which, when combined with a controlled amount of liquid phase, allows the deformation due to gravity to be minimised.

#### **4.4.3 Fusion**

Fusion describes the complete transformation from solid to liquid phase, which occurs at a specific temperature. Although ceramic bodies are not ascribed a melting point it is common to assign a refractoriness value that defines the temperature at which significant deformation occurs. Since the body is in the liquid phase flow occurs due to the effect of gravity and the body undergoes significant deformation.

## 4.5 Physical Changes During Firing

### 4.5.1 Volume

Bodies may experience either an increase or decrease in volume, or even both, throughout the firing period. Not all changes in volume are permanent, however, as the effect of cooling is such as to reverse the volume change. The reversible volume changes arise as a result of thermal expansion or contraction. Problems arise during firing when a difference exists between the value of the thermal expansion coefficient of the clay body and the glaze, causing expansion at unequal rates and ultimately effects similar to crazing. Differential expansion may also appear within the clay body itself yielding localised cracks. Not all bodies have the ability to regain their original volume upon cooling, in which case the thermal expansion coefficient contributes to a permanent change in the volume. Another reversible change arises from the quartz inversion which is itself a reversible reaction. The quartz expands at the inversional temperature of 573°C whilst being heated and contracts at the same temperature upon cooling, as shown in figure 4.1. The results represent those of a clay body which is only subjected to temperatures below those of vitrification so that any other changes in length arising during heating are reversible. Although the volume change associated with the dual quartz reaction is termed reversible it nonetheless produces a permanent increase in volume. The heating process disrupts the packing structure and because the body does not exhibit elastic behaviour the volume increase cannot be recovered totally upon cooling.

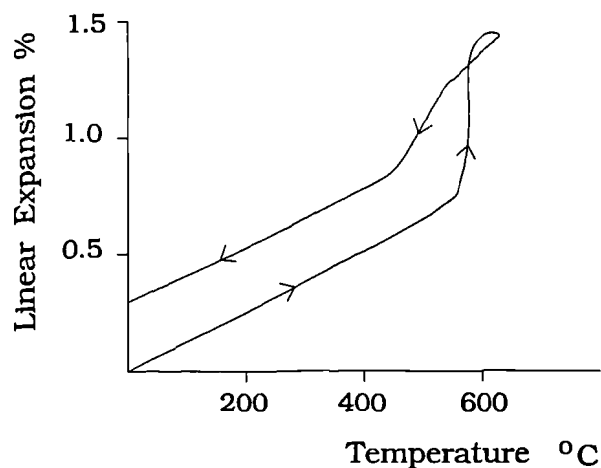


Figure 4.1 Hysteresis behaviour due to quartz inversions.

Irreversible changes in volume are permanent and arise from changes in the mineralogical composition during firing. During the preheating stage of firing the decomposition of certain minerals causes permanent expansion of bodies albeit minimal. The process of sintering results in an irreversible change by consolidating the material, yielding an associated reduction in the volume. Another permanent change in volume, which may be avoided, arises as a result of bloating which is produced by the expansion of trapped gases within closed pores.

All of the irreversible volume changes mentioned above, although of some significance to the final appearance of a fired ceramic article, are relatively small when compared to the firing shrinkage which arises as a result of vitrification. Volumetric firing shrinkages of values greater than 30% may be experienced by certain clay bodies [6]. Increased shrinkage results in cases where the initial porosity is high and which therefore facilitates the compaction process. Anisotropic shrinkage, originating from the shaping process as particles take up their preferred orientation, may occur during firing and inevitably leads to distortion. The rate and amount of shrinkage is not only dependent upon the material composition and structure but also upon the firing schedule applied to the ware.

#### **4.5.2 Porosity**

The true porosity of a body is the percentage of the total body volume occupied by both open and closed pores. The apparent porosity is a measure of the open pores and gives an indirect measure of the apparent vitrification; the greater the number of open pores the greater the volume available to the liquid phase. The porosity of most clay articles increases with temperature during the preheating stage when decomposition of minerals is occurring accompanied by the loss of chemically bonded water [8]. At higher temperatures the sintering process consolidates the material reducing the porosity. Thereafter vitrification causes the porosity to decrease further as molten matter fills the remaining open pores resulting in shrinkage of the body. At slightly above 1200°C the vitrified ware reaches a value of zero apparent porosity. Any increase in the value of the true porosity is now associated with bloating as the volume of the closed pores increases. Raising the temperature further would yield an associated increase in apparent porosity and cause the body to experience the undesirable effects of overfiring.

#### **4.5.3 Weight loss**

Losses in weight during firing occur initially in the smoking stage as a result of loss of water and continue through to the decomposition of kaolinite and that of the carbonates and sulphates. Weight loss is dependent upon the mechanism of vapour diffusion so that the greater the thickness of the article the higher the temperature at which loss occurs [8]. Ceramic materials experiencing a gain in weight do so as a result of either the oxidation of components such as ferrous iron, or the oxidation of sulphides. The average weight loss of ball clays is generally in the region of 8%, whereas purified china clays may exhibit a loss of up to 14% due to their higher content of hydrous minerals.

#### 4.5.4 Specific gravity

The true specific gravity is the mean value of the true density of all the minerals within the clay body. The bulk density depends upon the bulk volume of the clay including that taken up by both open and closed pores. It is related to the true density by

$$\text{density}_{\text{bulk}} = \text{density}_{\text{true}} (1 - \text{porosity})$$

where porosity is the fractional total pore volume. The value of the bulk specific gravity is identical to that of the bulk density when expressed in  $\text{gcm}^{-3}$ . The apparent specific gravity is independent of the volume of open pores so that a vitrified material, which therefore consists of a minimal number of closed pores, will exhibit a similar value to that of the true specific gravity. A typical variation of specific gravity over the firing schedule is depicted in figure 4.2 for a china clay.

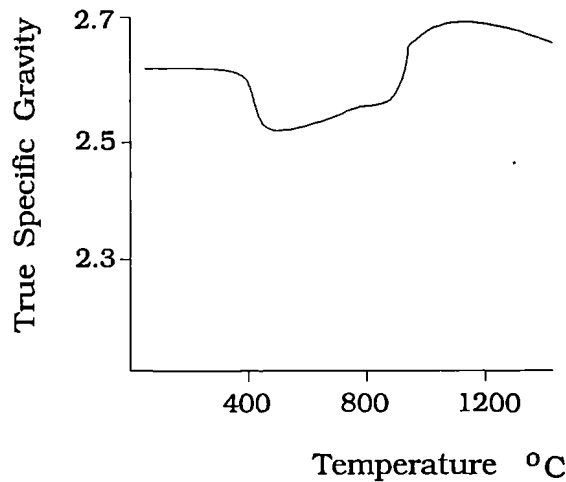


Figure 4.2 Variation of specific gravity with temperature for a kaolinite clay [7].

Thermal expansion of the body accompanied by loss of water at the beginning of the firing cycle causes the true specific gravity to decrease slightly. Decomposition of kaolinite at around  $500^{\circ}\text{C}$  results in a marked decrease, reflecting the change in structure. The subsequent shrinkage of the body due to sintering causes an increase in the specific gravity until about

950°C where the increase is dramatic, reflecting the exothermic reaction upon decomposition of metakaolinite to form mullite. The specific gravity tends to decrease as the temperature increases and as the formation of the liquid phase begins. Once the liquid phase is fully developed the specific gravity remains virtually constant. The weight of the body is constant throughout the liquid phase so that changes in the bulk density, which is porosity dependent, cancel out the volumetric changes resulting from firing shrinkage.

Factors affecting specific gravity include the plasticity of the clay; non-plastic clays yielding higher values of specific gravity than plastic clays. The amount of flux content is also influential as clays of greater flux content show a greater decrease in the specific gravity. The firing schedule affects the specific gravity in such a way that a high rate and short vitrification range yield a greater decrease and faster rate of reduction [8]. Slow cooling rates also have an effect, increasing the crystallisation from a liquid and thus yielding an increase in the specific gravity. The presence of impurities may be significant as they may combine with the body to form a fusible material and therefore cause a modification in the value of the true specific gravity [9].

#### **4.5.5 Strength**

Determination of the strength of a ceramic body during firing is of great industrial importance as it allows calculation of the maximum permissible heating rate. The ratio of the modulus of rupture to the modulus of elasticity is termed the critical strain and depends chiefly upon the mineralogical composition. During firing up to 800°C the value of the modulus of elasticity is virtually constant, the typical value for a kaolinite clay being  $10^4$  MNm<sup>-2</sup>. However, the modulus of rupture, a measure of the stress at which a body ruptures, varies quite considerably, passing through maximum and minimum values which are attributed to the mineralogical changes within the body.

Figure 4.3 depicts the variation of the modulus of rupture, showing an overall increase in magnitude.

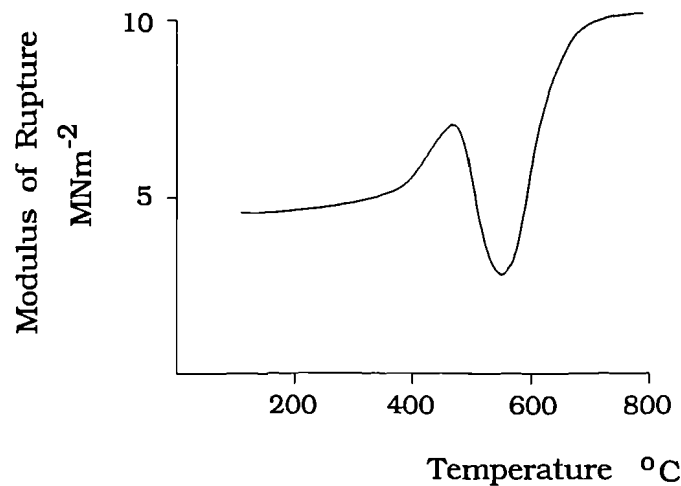


Figure 4.3 Typical variation of Modulus of Rupture for a kaolinite clay [10].

The increase in strength up to approximately 500°C occurs as a result of loss of adsorbed moisture and the bonding of particles which follows. The loss of chemically bonded water and the decomposition of kaolinite produces a reduction in strength from around 500°C. The rapid increase up to 800°C reflects the onset of the sintering of particles within the body. Addition of inert materials has the effect of reducing the overall strength and also reduces the maximum and minimum values of the modulus of rupture so as to smooth out the variation in the critical strain.

At temperatures above 800°C, that is during the glassy phase, experimentation by sonic methods has revealed a decrease in both the Young's modulus and the modulus of rupture, each modulus reaching its maximum value immediately prior to this phase [11]. Measurements of Young's modulus for porcelain reveal a significant decrease from the maximum value of  $7 \times 10^4$  MNm<sup>-2</sup> to 4 MNm<sup>-2</sup> at the end of firing [12].

The strength of fired bodies is significantly affected by the compositional content of mullite, with increased strength resulting from greater

mullite content [5]. The addition of nitrates also effectuates an increase in mechanical strength, whereas bloating decreases the strength [13,7]. Both porosity and, more significantly, the pore geometry are influential upon the elastic moduli of fired bodies; an increase in porosity generally yielding a linear decrease in the elastic moduli. However, in cases where the pores become more spherical as the porosity increases the values of the elastic moduli also increase so that the moduli/porosity relationships are no longer linear [2,14].

#### **4.6 Effects of Excessive Heating**

A great advantage of the firing process is that all body changes which take place, be they physical or chemical, are slow to reach completion, thus reducing the possibility of fracture and other faults such as cracking or discolouring. The rates of heating and cooling are extremely influential upon the quality and appearance of the ware and if not strictly monitored may produce unsatisfactory results. Also of significant importance in product quality is the maximum temperature to which articles are fired and the length of time that they are kept at this temperature. Articles fired at too high a temperature or soaked for too great a period of time experience over-heating which is the term given to the furthering of reactions causing fusion as a result of heating. The presence of a large amount of fused material can cause a body to distort under its own weight so that tall, narrow bodies dramatically lose height and gain in width at the base. Increasing the firing temperature or prolonging the soaking period of such a body would, therefore, cause even greater distortion. Other effects of prolonged soaking include the promotion of crystallisation resulting in a reduction in strength, increased shrinkage or expansion, and the swelling or bloating of articles. The effect of too much heat may also affect the glaze on certain articles resulting in a dull finish.

Continuous heating and cooling may be detrimental to the ware due to the hysteresis nature of thermal expansion. Sudden changes in temperature cause a body to experience thermal shock; the lower a body's resistance the greater the possibility of damage such as flaking and cracking. As a result, gradual cycling of repeated heating and cooling is usually preferred.

The physical changes that occur in the bodies during the firing process together with the time at which they occur and their duration will clearly have a significant effect upon the final product. It is these aspects of the firing process which are therefore of importance in the simulation of the ware and are reconsidered in the application of the TLM models of deformation in chapter 6. The structure and formulation of the TLM models now follows.

## 4.7 References

- [1] A Dinsdale, Pottery Science: Materials, Processes and Products, chapters 1-3&12, Ellis Horwood Series, John Wiley and Sons, 1986.
- [2] V T L Bogahawatta and A B Poole, "Strength-Porosity-Mullite Content Relationships for Kaolinitic Clay Bodies containing Lime Additive", British Ceramic Transactions Journal, vol 90, pp 184-189, 1991.
- [3] A B Searle, Clays and Clay Products, Pitman's Common Commodities and Industries Series, 2nd Edition, chapter II, Sir Isaac Pitman and Sons Ltd, London, 1915.
- [4] T -T Fang and H Palmour, "Useful Extensions of the Statistical Theory of Sintering", Ceramics International, vol 15, pp 329-335, 1989.
- [5] N M Ghoneim, E H Sallam and D M Ebrahim, "Role of Accessory Minerals on the Vitrification of Whiteware Compositions", Ceramics International, vol 16, pp 19-24, 1990.
- [6] W H Holmes, "The Firing of Clay-Based Ceramics", Sci Prog, Oxf, vol 60, pp 87-106, 1972
- [7] F H Clews, Heavy Clay Technology, 2nd Edition, chapter VII, Academic Press, 1969.

- [8] "Effect of Heat on the Physical Properties of Clay", Indian Ceramics, vol 2 [7], pp 233-237, 1955.
- [9] R W Grimshaw, *The Chemistry and Physics of Clays and Allied Ceramic Materials*, 4th Edition, pp 823, Ernest Benn Limited, London, 1971.
- [10] R O Hechroodt, "Factors Influencing the Critical Strain of Clay Materials during Firing", *Transactions of the Journal of the British Ceramic Society*, vol 70, pp 187-190, 1971.
- [11] G C Padgett, J A Cox and J F Clements, "Stress/Strain Behaviour of Refractory Materials at High Temperatures", Research Paper 608, British Ceramic Research Association, also printed in January 1969 *Transactions*.
- [12] J M Gaillard, C Gault, J C Glandus and P Petrault, "Prediction of Deformation in Plates using Finite Element Analysis and the Measurement of Physical Parameters under Process Conditions", *Ceramurgia, Materials Processes*, vol XXI, no 6, pp 229-232, 1991.
- [13] J Lemaitre, M Bulene and B Delmon, "Influence of Uniformly Dispersed Mineralizers on Firing and Mechanical Resistance of Clay Ceramics", *Clay Minerals*, vol 11, pp 313-325, 1976.
- [14] E A Dean and J A Lopez, "Empirical Dependence of Elastic Moduli on Porosity for Ceramic Materials", *Journal of the American Ceramic Society*, vol 66 [5], pp 366-370, 1988.

## **CHAPTER 5**

### **TLM MODELS**

The basic structure of a TLM diffusion routine is shown to yield models simulating the behaviour of viscous beams under the effect of gravity. A step by step development leads to a novel application of the technique to both cases of elongation and bending. The elongational model illustrates the change in behaviour from non-Newtonian to Newtonian at high viscosities and the bending model verifies the viscous/elastic analogy under constant stress. Emphasis is placed on bending with the inherent applicability of the model to beams of initial curvature being highlighted. Incorporation of the classical elastic beam theory previously outlined in chapter 2 yields the development of viscoelastic models which are shown to be in theoretical agreement. Steady state elastic solutions resulting from parallel viscoelastic TLM models are shown to agree with the classical elastic theory at small strains but also exhibit the phenomena of large deflections. The bending model is extended to incorporate deformation in two dimensions and is applicable to thin plates and shells. The formulation of an elastic bending model concludes this chapter.

## 5.1 Trouton's Descending Fluid

Consider a stream of fluid descending under its own weight as it flows through a hole in the base of a container. Once steady state is achieved the shape of the fluid directly beneath the hole resembles that shown in figure 5.1. The width of the stream gradually narrows down the length of the fluid until a point is reached where the fluid breaks away, at regular intervals of time.

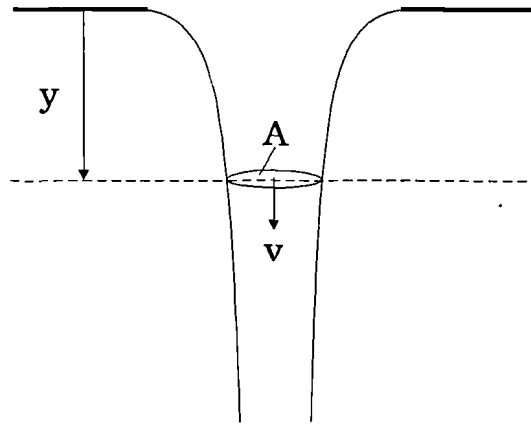


Figure 5.1 Descending viscous fluid.

At a distance  $y$  from the top of the stream the local fluid velocity is  $v$ , the rate of elongation being  $\frac{\partial v}{\partial y}$ . According to Trouton [1], the weight of the stream

below  $y$  provides a tractive force,  $F$ , such that

$$\frac{F}{A} = \lambda \frac{\partial v}{\partial y} \quad (5.1)$$

where  $A$  is the area of the cross-section at  $y$  and  $\lambda$  is a constant for a particular fluid. The volume of the fluid is conserved so that  $vA$  is constant throughout the period of flow. The constant  $\lambda$  is termed the coefficient of viscous traction and is related to the viscosity of the fluid,  $\eta$ , by  $\lambda=3\eta$  [2]. This relationship is analogous to that between Young's modulus of elasticity  $E$  and the shear modulus  $G$ , namely  $E=3G$ . The equation of motion of the fluid is determined by considering a volume element of the fluid at  $y$  of mass  $\rho A dy$ , which yields

$$\frac{\partial F}{\partial y} + \rho A g = \rho A \frac{Dv}{Dt} \quad (5.2)$$

and, upon substitution for F, leads to

$$\frac{\partial^2 v}{\partial y^2} + \frac{\rho}{\lambda} g = \frac{\rho}{\lambda} \frac{Dv}{Dt} \quad (5.3)$$

where

$$\frac{Dv}{Dt} = \frac{\partial v}{\partial t} + v \frac{\partial v}{\partial y} \quad (5.4)$$

so that  $\frac{D}{Dt}$  represents the substantial derivative.

Equations (5.3) and (5.4) are in agreement with the Navier-Stokes equations (2.23), (2.24) in chapter 2 derived for a viscous fluid, under the condition of zero applied pressure.

The problem above can be described as diffusion of the effect of gravity causing relative motion within a body. The amount of relative motion is dependent upon both the viscosity and density of the material. In the limit of either infinite viscosity or zero density no velocity gradient exists. A fluid of infinite viscosity behaves as a rigid solid body so that it would not pour from its original container but would, in fact, fall freely under gravity; all points in the fluid having a common velocity. Equation (5.3) determines the velocity at a distance  $y$  along the length of the descending fluid, provided that the fluid breakpoint has not been reached.

## 5.2 Formulation of an Elongational Viscous Model

Consider a column of viscous fluid supported vertically. The fluid is assumed to be of a suitable consistency so that a clamp at the top of the column supports the weight of the fluid. If the column remains supported for a sufficiently long period of time the shape of the fluid near the support will

resemble that in figure 5.1, the time taken to reach this state being dependent upon the properties of the fluid. It is of interest here to consider the flow of the column of viscous fluid only whilst continuity is maintained. It may therefore be assumed that at any point in the column the fluid does not break away during flow. After a certain period of time has elapsed the fluid will resemble that in figure 5.2. All cross-sections of the fluid may be considered to lie above a fictitious fluid breakpoint since continuity is maintained. The equation of flow will be dependent upon the density and viscosity of the fluid as in the case of the descending stream of viscous fluid.

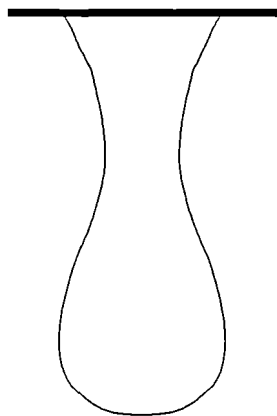


Figure 5.2 Deformed viscous column of fluid.

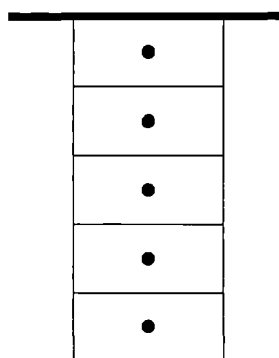


Figure 5.3 Fluid before deformation.

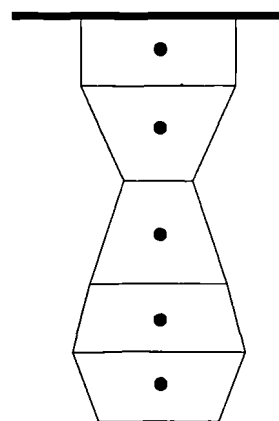


Figure 5.4 Deformed fluid.

Now consider the column of viscous fluid to be spatially discretised into fluid elements as in figure 5.3. Here, the velocity of the fluid within each

element is represented by the velocity at a single, central point. After a certain period of time the shape of the column of fluid will take the form of that in figure 5.2 and is shown in discretised form in figure 5.4. The first point in the top element of the fluid incorporates the no-slip condition and retains its original position as a result. All other elemental points have a new position due to the combination of displacement by elements above and elongation of the elements themselves, this arising from the traction produced by the fluid below. It follows then that the total velocity at any point in the fluid is the sum of the local velocity of the element yielding elongation and the convective, or accumulative, velocity yielding displacement. The acceleration at each point, therefore, consists of two parts; a local acceleration and a convective acceleration. Thus, the equation of motion for the stream of fluid descending under its own weight may be applied to the supported column of fluid, that is

$$\frac{\partial^2 v}{\partial y^2} + \frac{\rho}{\lambda} g = \frac{\rho}{\lambda} \frac{\partial v}{\partial t} \quad (5.5)$$

where  $v$  is now the total velocity consisting of an accumulative velocity and an elongational velocity.

Equation (5.5) may be re-written as follows;

$$\frac{\partial^2 v}{\partial y^2} + \frac{\rho}{\lambda} \frac{\partial(gt)}{\partial t} = \frac{\rho}{\lambda} \frac{\partial v}{\partial t} \quad (5.6).$$

The analogous TLM network equation is given by

$$\frac{\partial^2 \Phi}{\partial y^2} + 2R_d C_d \frac{\partial \Phi'}{\partial t} = 2R_d C_d \frac{\partial \Phi}{\partial t} \quad (5.7)$$

where  $\Phi'$  is a distributed potential such that, in general terms,  $\Phi' = g't$ ;  $g'$  being a constant.

The constant  $\frac{\partial \Phi'}{\partial t}$  may be considered to drive the circuit. Therefore the additional potential  $\Phi'$  causes the network potential  $\Phi$  to increase with time

such that if  $\frac{\partial^2 \Phi}{\partial y^2}$  is positive then  $\frac{\partial \Phi'}{\partial t}$  represents a lower limit in the solution of  $\Phi$ , and if  $\frac{\partial^2 \Phi}{\partial y^2}$  is negative then  $\frac{\partial \Phi'}{\partial t}$  represents an upper limit. Here it is assumed that  $\frac{\partial \Phi'}{\partial t}$  is the only distributed driving source; there being no external, or ambient, sources.

Clearly, in the case of a body of viscous fluid subjected solely to gravity, the acceleration at any point within the fluid cannot exceed the gravitational acceleration. When the upper limit of the acceleration is reached throughout the material the body is free falling and there is no relative motion of the fluid within the body itself, that is there is no flow.

The circuit driver  $\frac{\partial \Phi'}{\partial t}$  provides the network with an associated maximum or minimum distributed potential  $\Phi'$ , the value of which increases with time. The value of  $\Phi'$  after a time period  $t$  may be denoted by  $g't$ , where  $\frac{\partial \Phi'}{\partial t} = g'$ , so that the potential applied to the circuit is increased by  $g'\delta t$  every timestep.

The provision of the applied potential increase to the circuit may be accomplished by re-initialising the incident pulses. That is, the incident pulse values are updated by  $\frac{g'\delta t}{2}$  each timestep, ensuring that the potential is increased by the appropriate amount. In this way the pulses carry the full information of the potential in the network and automatically enforce the limiting behaviour of the driving source. In the limit when  $\Phi = \Phi'$  for each node, no relative motion occurs and the whole network is in static equilibrium with no net current flow since, from chapter 3, all incident pulses have the same value of  $\frac{\Phi'}{2}$ .

Gravity acts upon each element of the body as an internal source, diffusing its effect throughout the body, the flow that develops as a result being dependent upon the material parameters. Modelling the viscosity in the resistance and the density in the capacitance of the network yields

$$\Phi = \text{velocity} = v$$

$$C = C_d \times (\text{elemental volume}) = \rho \times (\text{elemental volume}) = \text{elemental mass} = m$$

$$R = R_d \frac{\text{elemental length}}{2 \text{ cross-sectional area}} = \frac{\text{elemental length}}{2 \lambda \text{ cross-sectional area}}$$

(5.8).

Using the network relationship for current,  $I = C \frac{\partial \Phi}{\partial t}$ , it follows that the current at a node represents the resultant viscous tractive force developed over a given time period. The net current between neighbouring nodes, therefore, represents the net force.

It would be equally valid to model both the density and viscosity by the capacitance, in which case the current at a node would represent the total force divided by the coefficient of viscous traction, or the 'effective' total force, and the net current would represent the net effective force.

In thermal applications the excitation of the network generally arises from either external heat sources or heat generation within the body itself due to, for example, exothermic reactions caused by changes of state. Such internal heat effects have been shown in chapter 3 to be accommodated for by a current generator, or in the case of heat loss by a resistor to earth. When a current generator models a heat effect the addition to the potential of the node is calculated according to

$$\frac{I_{\text{gen}}}{2d \sum_{l=1} \frac{1}{(R+Z)}} \quad (5.9)$$

which in a one dimensional routine ( $d=1$ ) is equal to

$$I_{gen} \frac{(R+Z)}{2} \quad (5.10).$$

It is clear that the excitation due to gravity,  $g$ , cannot be represented accurately in terms of a potential arising from a current generator, since if  $I_{gen} = C g$  then the loading potential would be

$$Cg \frac{R}{2} + Cg \frac{Z}{2} = \frac{\rho g \delta l^2}{4 \lambda} + \frac{g \delta t}{2} \quad (5.11)$$

thereby introducing an additional loading term which is inconsistent with the flow equation (5.5). It is, however, interesting to note that for high values of  $\lambda$  the additional loading term is negligible so that this method of loading is consistent with that of modelling the loading in the pulses. For low values of  $\lambda$  the additional loading term becomes significant and as  $\lambda$  tends to zero this term dominates the routine so that the gravitational acceleration is not imposed as the upper limit in the model.

### 5.2.1 Boundary conditions

No surface forces, such as air resistance or surface tension, are assumed present resulting in the absence of any external sources. Clearly, then, the body may be considered to be insulated from its surroundings since all source generation occurs within the body itself. A one dimensional TLM treatment assumes insulation along the length of a body yet incorporates the cross-sectional geometry in the formulation of the network parameters, so that it does in fact represent a three dimensional body insulated along its entire length. Thus, the question still remaining is "how are support conditions incorporated?" Treatment of boundaries are considered in terms of nodal potentials or pulse values. Consider a solid-fluid boundary, or interface. From viscous flow theory, detailed in chapter 2, the layer of fluid adjacent to the solid boundary does not move with respect to this boundary. That is, a no-

slip condition exists. Consider again a vertical column of fluid supported at the top element, as in figure 5.5. To ensure a value of zero velocity for the first element the nodal potential is set to zero throughout the modelling period.

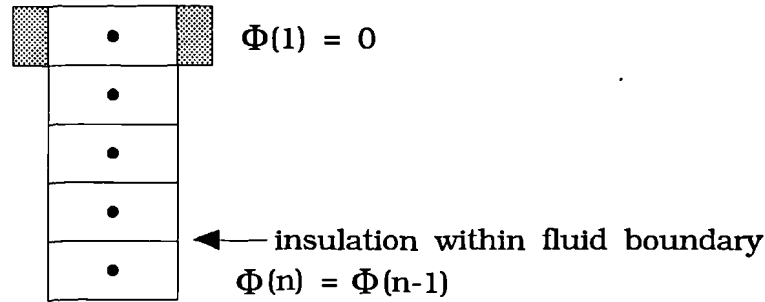


Figure 5.5 Clamped viscous column with boundary conditions.

In this way the no-slip node is unaffected by the rest of the fluid in the column and, therefore, can be considered analogous to an adiabatic node in thermal diffusion applications. Here, it is assumed that the support is unaffected by the presence of the fluid so that the velocity of the support is maintained at zero and, although not modelled directly, is represented by the nodal potential of the first element. The opposite end of the column is unsupported so that its displacement is not impeded by the surroundings. However, at the base of the column the fluid must be retained within the bulk of the material so that although the final element may be displaced it may not experience any elongation. Therefore, the velocity of the final element must equal that of the previous element so that  $\Phi(n)=\Phi(n-1)$  where  $n$  denotes the node of the final element in the column. In this way insulation takes effect within the material boundaries, ensuring no loss of fluid into the surrounding medium. Because the surroundings are assumed to have no effect upon the column of fluid, it follows that the velocity of the medium adjacent to the base of the column is equal to that of the final element. It is now evident that a double insulation is

present at the final node such that  $\frac{\partial^2 v}{\partial x^2} = 0$ .

It should be noted that in figure 5.5 the position of the second node represents a distance of zero from the base of the clamp and the position of the final node  $n$  represents a distance equivalent to the total length of the column extending from the clamp. At the first node the values of the incident pulses are  $V^i(1,1)=0$  and  $V^i(1,2)=V^r(2,1) + \frac{1}{2}g\delta t$ . The nodal representation of figure 5.5 may be altered to that of figure 5.6 where the volume of the first and final elements are half that of a general element. The elements of nodes 1 and  $n$  contain only half a transmission line which connects each of them to their neighbouring fluid elements, so that the link line impedance is maintained constant. The second half of the transmission line is redundant in each case due to the boundary pulse and potential conditions.

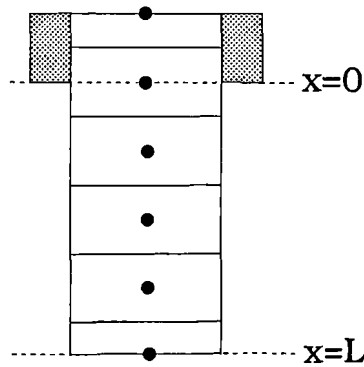


Figure 5.6 Equivalent nodal representation of figure 5.5.

### 5.2.2 Results of elongational model

Using the above formulation elongation results have been obtained for columns of 10cm in length after a period of 0.1s. The columns of fluid all have the same density of  $1 \text{ gcm}^{-3}$  and a cross-sectional area of  $1 \text{ cm}^2$ . Volume is conserved using a Poisson's ratio of 0.5. The viscosity of the columns varies from  $10000 \text{ gcm}^{-1}\text{s}^{-1}$  to  $1 \text{ gcm}^{-1}\text{s}^{-1}$ . The new lengths of the columns resulting from elongation are tabulated below in table 5.1, showing an increase in elongation as the viscosity decreases.

	Viscosity in $\text{gcm}^{-1}\text{s}^{-1}$	Total length in cm
Column 1	10000	10.17
Column 2	1000	11.64
Column 3	100	14.66
Column 4	10	14.85
Column 5	1	14.85

Table 5.1 Lengths of a variety of viscous columns after 0.1s.

From the table it can be seen that the value of  $1 \text{ gcm}^{-1}\text{s}^{-1}$  yields no further increase in elongation than for the value of  $10 \text{ gcm}^{-1}\text{s}^{-1}$  after the same period of deformation. This implies that, although column 5 has a lower viscosity than column 4, the total rate of elongation throughout the column is the same in both cases.

In figure 5.7a the rate of elongation at each element in column 4 reveals high rates of elongation near the support decreasing to zero rates of elongation towards the free end. Figure 5.7b shows that these lower elements have accelerations equivalent to the acceleration of gravity.

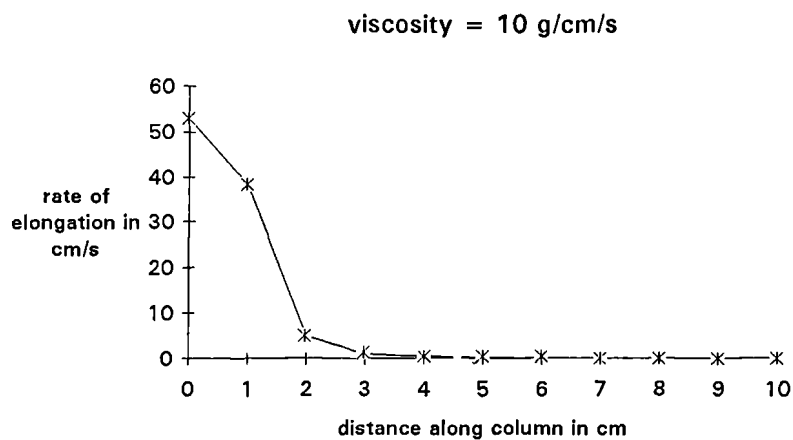


Figure 5.7a Rate of elongation results for column 4 after a time period of 0.1s.

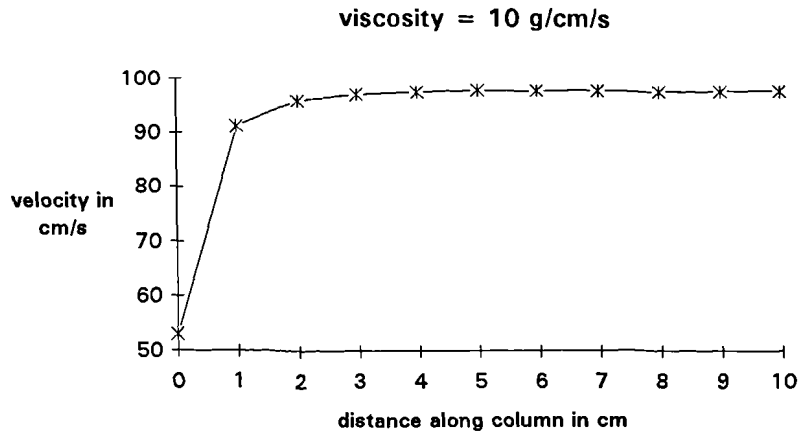


Figure 5.7b Velocity results for column 4 after a time period of 0.1s.

In figure 5.8a the rate of elongation in column 5 reveals a higher rate of elongation closer to the support than for column 4 and from figure 5.8b an increased number of elements are shown to reach a velocity of  $98 \text{ cm/s}^{-1}$  which after a time period of 0.1s is equivalent to the acceleration of gravity. Clearly, although the total amount of elongation is equivalent in both cases the distribution of the elongation throughout the columns is different. In fact, only at high viscosities is the elongation rate, and hence the elongation, linearly distributed over each element in the column, being proportional to the weight of the fluid below each element.

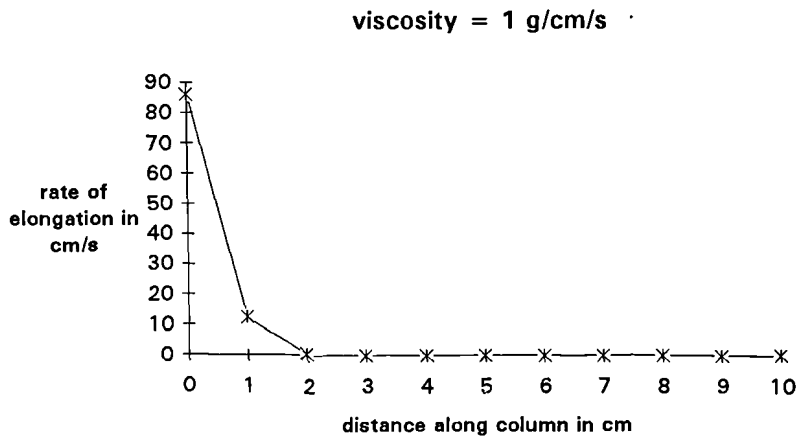


Figure 5.8a Rate of elongation results for column 5 after a time period of 0.1s.

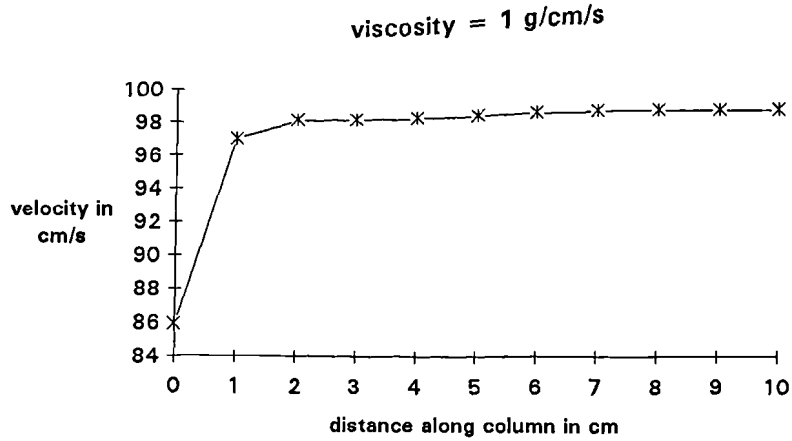


Figure 5.8b Velocity results for column 5 after a time period of 0.1s.

The rate of elongation along column 1 is depicted in figure 5.9a and shows a nearly linear relationship with distance from the end of the beam, and hence with the weight below each element. Figure 10 shows the rate of elongation displaying a linear relationship with distance for a column of  $10^5 \text{ gcm}^{-1}\text{s}^{-1}$ .

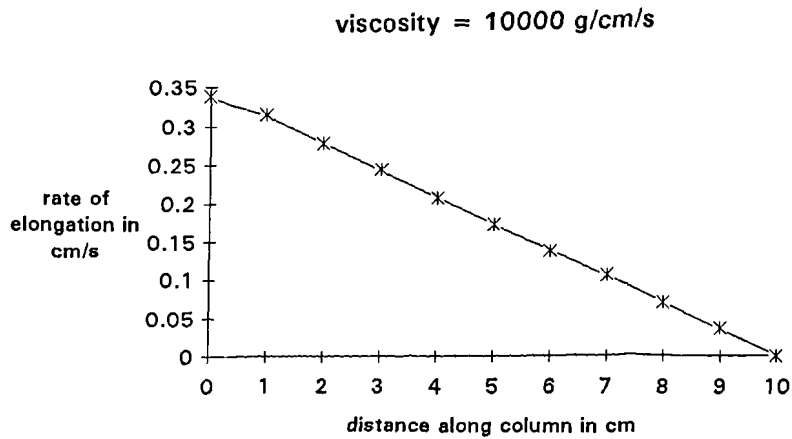


Figure 5.9a Rate of elongation results for column 1 after a time period of 0.1s.

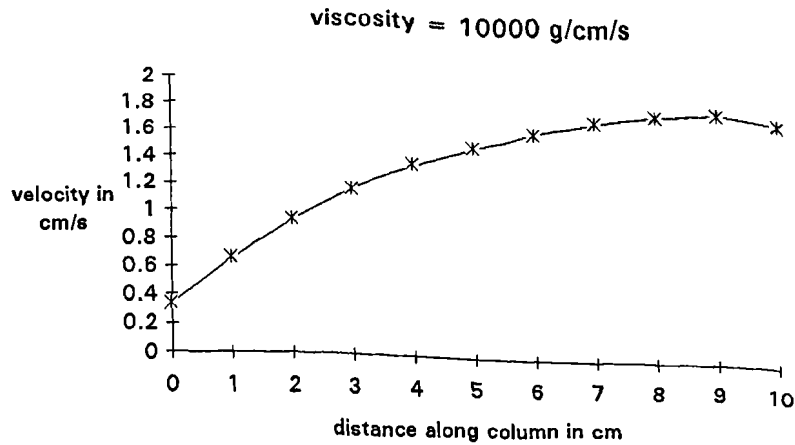


Figure 5.9b Velocity results for column 1 after a time period of 0.1s.

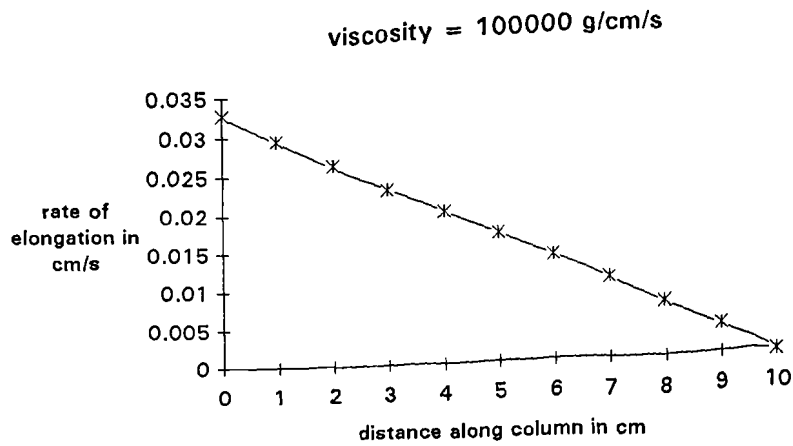


Figure 5.10 Rate of elongation for column of  $10^5 \text{ gcm}^{-1}\text{s}^{-1}$  after 0.1s.

The resultant stress distribution is, therefore, dependent upon the viscosity (and density) and is reflected by the elongation distribution. As the viscosity is taken towards a zero value all the elements in the column reach the gravitational acceleration except the first element beyond the support which experiences all the elongation.

The elongation of each column is calculated from the elongation rate but may perhaps differ slightly from observed results since the model does not incorporate the effect of surface tension. Bodies of low viscosity, therefore,

do not display a profile as depicted in figure 5.2 where bulging at the base of the column, beyond its original width, arises due to surface tension.

### 5.3 Formulation of a Bending Viscous Model

Consider a column of viscous fluid supported horizontally, the cross-section of which being depicted in figure 5.11a. After a period of time, assuming no elongation of the material, the curvature of the cantilever of fluid changes under the effect of gravity to represent that in figure 5.11b. For a material of infinite viscosity the curvature of the cantilever would remain equal to zero.

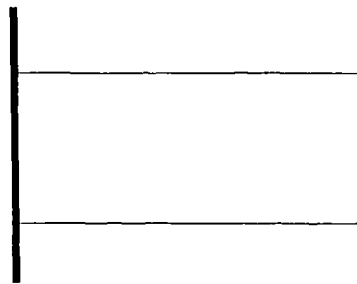


Figure 5.11a

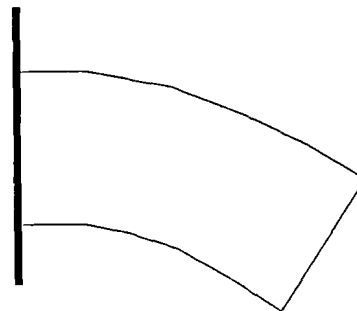


Figure 5.11b

A beam of discrete elements may be considered analogous to a hinged system of rigid bodies; the stiffness of the hinges being represented by the viscosity of the material. As mentioned in section 2.1.5 of chapter 2, the rotation and translation of a fluid element resembles that of a rigid body. The concept of a hinged system therefore enables the laws of rigid body motion,

outlined in section 2.3, to be applied to a viscous body subject to rotational effects. Each element is assumed to represent a rigid body which rotates about each of its neighbours according to the supporting constraints.

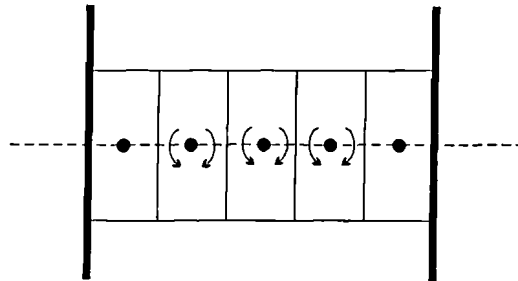


Figure 5.12 Simply supported beam of fluid.

In the case of a column of fluid, supported horizontally at both ends, each element rotates relative to elements on either side as in figure 5.12.

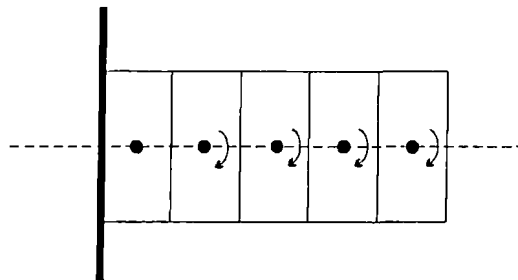
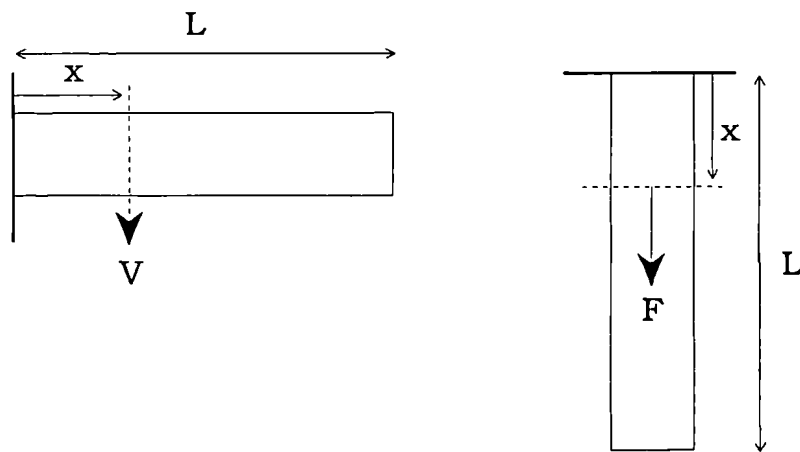


Figure 5.13 Cantilever of fluid.

Elements in a cantilever rotate only about neighbours lying at the same side as the support; in figure 5.13 elements rotate only about neighbours on their left. Thus, in either case elements rotate about the neighbours which form a line of connection to a support. This line of connection runs through the centres of the elements and is equivalent to the neutral axis as defined in chapter 2. As in the case of the vertical column of fluid gravity acts at each point within the fluid. However, in the case of the horizontally supported beams the effect of

the action of gravity is such as to produce a shearing force, and hence a moment, causing each element to rotate.

Consider the rotation of an element of the cantilever in figure 5.13. In this case, the effect of gravity on the element produces a shearing force which results in rotation. The shearing force  $V$  acting on a horizontal beam at a distance  $x$  from the support is equivalent to the tractive force  $F$  acting on an identical beam supported vertically, the beams being depicted in figures 5.14a and 5.14b respectively.



Figures 14a and 14b Horizontal and vertical viscous beams subjected to shear and traction respectively.

Results from the elongational model show that both the amount of elongation and the distribution of the elongation throughout the beam is dependent upon the viscosity and /or density. The elongation of each element is directly proportional to the velocity causing elongation which is itself proportional to the net force on the element. The resultant force distribution is therefore parameter dependent. It now follows that the shear force acting on a horizontally supported beam of fluid must also be viscous/density dependent. In the case of very low viscous fluids, where the acceleration of the elements at the lower end of a vertical beam is equivalent to the gravitational acceleration,

no elongation of the fluid occurs in this lower region as the difference in the resultant force between consecutive elements is zero. It follows that no net force acts on each of these lower elements. Therefore, for a horizontally supported beam of the same fluid parameters, no shear force would act on the beam towards its free end. However, in the case of highly viscous fluids where the elemental elongation is proportional to the weight of the fluid below, so that  $F$  is given by  $F = \rho (L-x) A g$ , where  $A$  is the area, then the shear force  $V$  is also given by  $V = \rho (L-x) A g$ .

Initially, gravity acts parallel to the sides of the element as in figure 5.15a. The shearing force is assumed to act along the boundary on the right of the element and produces an elemental bending moment  $\delta M$ . From chapter 2, the shearing force  $V$  is related to the bending moment  $M$  by

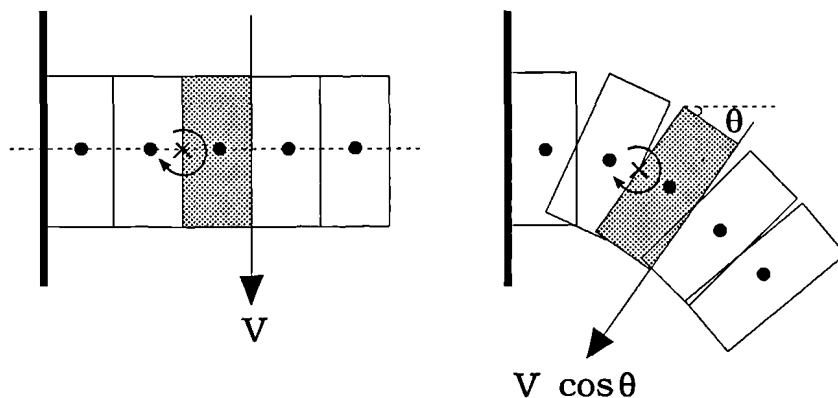
$$V = \frac{dM}{dx} \quad (5.12)$$

from which it follows that the elemental bending moment  $\delta M$  is given by

$$\delta M = V \delta l \quad (5.13)$$

where  $\delta l$  is the elemental length.

The line of connection passes through a fictitious hinge which connects the element to its neighbour so that the elemental bending moment acts about this hinge.



Figures 5.15a and 5.15b Local rotation of a rigid body element at subsequent time intervals.

The elemental bending moment causes the element to rotate without, it is assumed, changing the shape of the element so that opposite sides remain parallel. Figure 5.15b shows the subsequent rotation experienced by the element. The element has rotated about the fictitious hinge and lies at an angle  $\theta$  to the horizontal. Gravity is assumed to produce a shearing force which acts parallel to the sides of the element at all times. The component of gravity which now acts parallel to the sides of the element is  $g \cos\theta$ . Therefore the associated shearing force is now  $V \cos\theta$  and the elemental bending moment is given by

$$\delta M = V \delta l \cos\theta \quad (5.14).$$

For a highly viscous fluid, which does not move significantly before the stresses have developed fully, the shear force is given by  $V = \rho (L-x) \text{ area } g$ , so that the expression for the elemental bending moment becomes

$$\delta M = \rho (n-i) \delta l^2 \text{ area } g \cos\theta \quad (5.15)$$

where  $n\delta l = L$  and  $i\delta l = x$ .

The area of overlap of the elements in figure 5.15b is equivalent to the area of the gap formed between them, as a result of rotation about hinges lying on the neutral axis which passes through their centres. It follows that, when considering three dimensions, volume is conserved; each element being modelled with the same elemental volume and hence elemental mass. However, real fluids maintain material continuity, with the fluid elements experiencing tension along the upper length of the element and compression along the lower length. The fluid, therefore, is stressed tractively so that the coefficient of viscous traction is responsible for the ensuing flow. In the rigid body representation the pure rotation of each element must result from a combination of two equal shearing actions, so that no deformation of the shape of the fluid elements is observed, and indicates that the flow is dependent upon the shear viscosity. Therefore, the present representation may be assumed to maintain material continuity, and thus represent bending, only if the coefficient

of viscous traction is used in the model so that fluid elements are able to deform tractively with bending.

The above discussion leads to the formulation of the equation describing angular rotation in a viscous body. The form of the equation will take that of equation (5.5) derived earlier but will replace the concept of linear momentum by that of angular momentum for a three dimensional body. Thus,

$$\frac{\partial^2 I_z \omega}{\partial x^2} + \frac{\partial M}{\partial x} \frac{1}{\lambda} = \frac{\rho}{\lambda} \frac{\partial I_z \omega}{\partial t} \quad (5.16)$$

where  $I_z = \frac{bh^3}{12}$  is the area moment of inertia, defined in section 2.3.4 of chapter 2 and  $\omega$  is the total angular velocity.

Or, in terms of the shearing force V,

$$\frac{\partial^2 I_z \omega}{\partial x^2} + \frac{V}{\lambda} = \frac{\rho}{\lambda} \frac{\partial I_z \omega}{\partial t} \quad (5.17).$$

Substituting for  $V = \rho (n-i)dl bh g \cos\theta$  for high values of  $\lambda$ , leads to

$$\frac{\partial^2 I_z \omega}{\partial x^2} + \frac{\rho (n-i)dl bh g \cos\theta}{\lambda} = \frac{\rho}{\lambda} \frac{\partial I_z \omega}{\partial t} \quad (5.18).$$

Each element, therefore, rotates as a result of gravity acting upon the element itself and as a result of the rotation of neighbouring elements. For example, in the case of the cantilever in figures 5.15a and 5.15b if the second element from the support rotates through an angle  $\theta$  then, because of material continuity, so must all the remaining elements in the beam.

Figure 5.16 shows the axis of rotation of a solid body. The shaded region depicts the plane area  $bh$  normal to the axis.

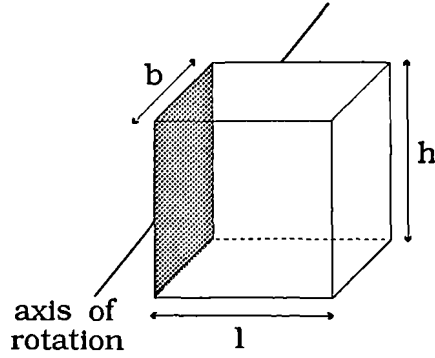


Figure 5.16 The axis of rotation passes through a fictitious hinge connecting neighbouring elements.

Substituting for  $I_z$  in equation (5.18) leads to

$$\frac{\partial^2 \frac{h^2 \omega}{12}}{\partial x^2} + \frac{\rho}{\lambda} \frac{\partial((n-i)\delta l g t \cos\theta)}{\partial t} = \frac{\rho}{\lambda} \frac{\partial \frac{h^2 \omega}{12}}{\partial t} \quad (5.19).$$

Comparison of equation (5.16) with the modified diffusion equation (5.7) yields the following relationships:

$$\Phi = \frac{h^2 \omega}{12}$$

$$C = \rho \times (\text{elemental volume}) = \text{mass} = m$$

$$R = \frac{\text{elemental length}}{2 \lambda \text{ cross-sectional area}} \quad (5.20).$$

Now,  $\Phi' = (n-i)\delta l g t \cos\theta$  so that the pulses are updated by  $\frac{(n-i)\delta l g \delta t \cos\theta}{2}$

each timestep. It is evident that for high viscosities (or low densities) the value of  $\Phi'$  varies for each node so that the applied potential does not act as a constant uniform upper limit to the circuit potential as in the elongational model. However, for low viscosities (or high densities) the shear force and

hence  $\Phi'$  must be determined from the net forces in the elongational model, yielding zero shear forces in the limit as the viscosity tends to zero. A limit is therefore also imposed upon the circuit potential in the bending model which has a constant uniform value of zero.

Using the network relationship for current,  $I = C \frac{\partial \Phi}{\partial t}$ , the current at a node has units of force multiplied by distance and therefore represents the resultant viscous bending moment. The net current between nodes, therefore represents the net bending moment.

As mentioned earlier in the case of the elongational model, the viscosity may also be modelled by the capacitance so that the resistance is purely dependent upon the dimensions of the body, and the current represents the bending moment divided by the coefficient of viscous traction.

Clearly, the angular velocity  $\omega$  of each element may be determined from the corresponding value of the nodal potential. The angle of inclination,  $\theta$ , can thus be determined from the relationship  $\theta = \int_0^t \omega dt$  which is

represented in discrete form by the summation of  $\omega \delta t$  over the period of deformation.

The viscous approach at high viscosities is similar to that taken in classical elastic theory, described in section 2.4.2 of chapter 2, where the shearing force acting on each section of a beam is equivalent to the total weight of the beam to the right of that section. In the elastic formulation it is assumed that the elastic body stresses are developed instantaneously. In the viscous model the shear viscous stresses, and thus bending moments, are allowed to develop with time so that ultimately the material parameters not only dictate the magnitude of the deformation but also dictate the change in curvature along the length of the beam.

### 5.3.1 Boundary conditions

The effects of the surrounding media on the body are represented by the boundary conditions. In fact, the types of boundaries occurring in the case of the cantilever are similar to those of the vertically supported column of fluid discussed in section 5.3 and are illustrated in figure 5.17. At the supported end the no-slip condition applies within the fluid so that the angular velocity of the first element is zero ensuring no relative motion with respect to the stationary support. This is achieved in the TLM network by setting the nodal potential to zero at the first node throughout the simulation. The pulses incident at the first node take the following form,  $V^i(1,1)=0$  and  $V^i(1,2)=V^r(2,1)+\frac{1}{2}(n-1)\delta l g \delta t \cos\theta$ . The sides of the cantilever are not subject to any resistance to motion and are effectively insulated from the surroundings. This ensures that, at each distance  $x$  along the cantilever, the angular rotation throughout the height and width of the beam is constant so that no shearing effects are introduced and the cantilever experiences pure bending. As in the case of the vertical column, these boundary conditions can be adequately modelled by a one dimensional treatment. Once again, the surroundings are assumed to have no effect at the free end of the cantilever so that the angular velocity of the surroundings adjacent to the free end is equivalent to that of the final node. This insulation may be represented by a perfectly reflecting boundary, such that the pulse incident from the free end is equal to the pulse reflected from the node as depicted in figure 5.17.

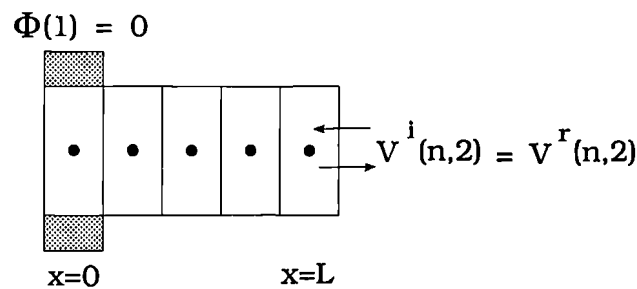


Figure 5.17 Boundary conditions for viscous cantilever.

Clearly, the boundary condition at the free end of the cantilever is slightly different from that of the vertical column where the condition of no elongation, that is  $\frac{\partial v}{\partial x} = 0$  and hence zero net force, was enforced by setting the potential of the final node equal to that of the previous node. At the free end of the cantilever the bending moment is zero yielding  $M = \lambda I_z \frac{\partial \omega}{\partial x} = 0$  and therefore  $\frac{\partial \omega}{\partial x} = 0$ . Although the angular strain rate  $\frac{\partial \omega}{\partial x}$  is zero, the end of the cantilever does in fact strain with respect to the previous element so that the potential of the final node is not equal to that of the previous node. However, the final element is not assumed to strain with respect to the surroundings and so the final nodal potential is equal to that of the adjacent node of the surrounding medium.

Consider now a simply supported beam where both ends are clamped, as in figure 5.18. Clearly, at each end of the beam the no-slip condition holds ensuring zero rotation.

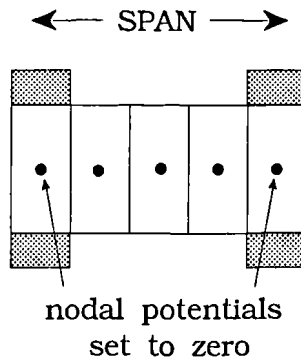


Figure 5.18 Boundary conditions for a simply supported viscous beam.

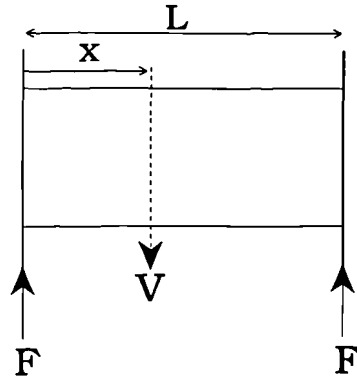


Figure 5.19 Forces acting on simply supported beam.

The weight of the beam is supported equally by the two supports so that the upward force exerted by each support is given by  $F = \frac{1}{2} \rho \text{ area } L g$ , as shown in figure 5.19. Therefore, for a highly viscous fluid the resultant downward force acting at a distance  $x$  from the left support is given by

$$V = F - \rho \text{ area } x g = \rho \text{ area } \left( \frac{L}{2} - x \right) g \quad (5.21).$$

As for the cantilever, a general element of the beam will rotate throughout the deformation period so that the component of gravity causing the rotation is  $g \cos\theta$ , where  $\theta$  is the angular inclination of the element to the horizontal. The notation for the shear force acting on a general element  $i$  is, therefore, given by

$$V = \rho \left( \frac{n}{2} - i \right) \delta l \text{ area } g \cos\theta \quad (5.22)$$

where  $n\delta l = L$  and  $i\delta l = x$ .

The shear force is incorporated by the updated pulse values yielding;

$$V^i = V^i + \frac{g \delta t}{2} \cos\theta \left( \frac{n}{2} - i \right) \delta l \quad (5.23).$$

At present lateral movement of the beam ends will accompany sagging. The ends will move towards one another as if they had been placed on rollers.

The no-slip boundaries, therefore, only enforce the condition of zero rotation. If it is required to enforce constraints upon the lateral movement, such as a restriction upon the length of the span, then additional control related to the error in the lateral movement is necessary at the beam ends. Such a controlling mechanism is described in the following section.

### 5.3.2 PID control and tuning

Proportional, integral and derivative (PID) control consists of a combination of three types of control which are commonly applied to electronic feedback amplifier design [3,4]. A particular feedback system may not have a good transient response and may also yield considerable steady state errors. Application of PID control to the system enables improvement in both the transient and steady state responses. The proportional and integral controls are applied to improve the steady state response of the system, but unfortunately at the same time generally yield instability during the transient. The purpose of the derivative control is therefore to dampen the system and thus yield an improved transient response.

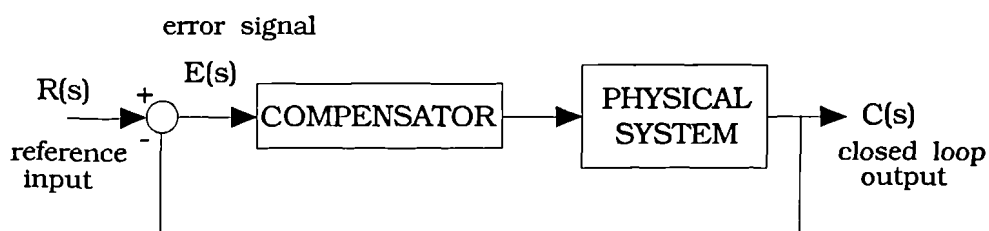


Figure 5.20 Unity gain feedback system and compensator.

The compensator in figure 5.20 houses the PID control. Each of the three control types may be expressed in either continuous or discrete form.

### Proportional control

Here, the applied control is directly proportional to the error observed over each timestep and thus is expressed continuously as

$$u(t) = K_p E(t) \quad (5.24)$$

or discretely as

$$u(k) = K_p E(k) \quad (5.25)$$

where  $u(t)$  is the control as a function of time,  $t$ ;

$u(k)$  is the control as a function of iteration number,  $k$ ;

$K_p$  is a proportionality constant;

$E(t)$  is the error as a function of time;

$E(k)$  is the error as a function of iteration number.

### Derivative control

Here, the applied control is proportional to the time rate of the error and is expressed continuously as

$$u(t) = K_p T_D \frac{dE(t)}{dt} \quad (5.26)$$

or discretely as

$$u(k) = K_p T_D \left( \frac{E(k) - E(k-1)}{T} \right) \quad (5.27)$$

where  $T_D$  is termed the derivative time;

$T$  represents the iteration timestep.

### Integral control

Integration of the error provides the control in this case and may be expressed continuously as

$$u(t) = \frac{K_p}{T_I} \int_{t_0}^t E(t) dt \quad (5.28)$$

or discretely as

$$u(k) = \frac{K_p}{T_I} T E(k) + u(k-1) \quad (5.29)$$

where  $T_I$  is the integral (or reset) time.

The PID controller can thus be expressed discretely as

$$u(k) = K_p \left( E(k) + T_D \left( \frac{E(k) - E(k-1)}{T} \right) + \frac{T}{T_I} E(k) \right) + u(k-1) \quad (5.30).$$

The error  $E(k)$  is determined experimentally and thus it just remains to determine the values of the constants  $K_p$ ,  $T_D$  and  $T_I$ .

The method for determination of the constants may be considered analogous to tuning the system. Initially, the proportional control only is considered. The constant  $K_p$  is gradually increased until the response of the system oscillates. The value at which oscillations first appear is noted and  $K_p$  in the PID control equation is set to half of this value, so that the solution is kept well away from any instability. The values of the remaining constants are then determined by trial and error until the system is tuned.

In the case of a simply supported beam the source of error results from the change in the span with time. In the associated TLM network the control is applied by a current generator at each of the no-slip boundary nodes and contributes a correcting moment. The PID control, therefore, takes the following form

$$I_{gen} = (a \text{ ERROR}(k) + b \text{ SUM\_ERROR}(k) + c \text{ DIFF\_ERROR}(k)) \frac{C\delta l}{\delta t^2} \quad (5.31)$$

where

$\text{ERROR}(k)$  represents the change in span, with respect to the true, or original, span. That is,  $\text{ERROR}(k) = 0.5(\text{SPAN}(k) - \text{TRUE\_SPAN}(k))$ . The factor of 0.5 being included since the two supports equally compensate for the error;

SUM\_ERROR(k) represents the summation of ERROR(k) up to and including the present iteration;

DIFF\_ERROR(k) represents the change in ERROR(k) over an iteration, namely  $ERROR(k) - ERROR(k-1)$ ;

C is the capacitance of the element;

$\delta t$  is the iteration timestep;

$\delta l$  is the nodal separation;

a, b and c are constants to be determined using the tuning technique described above.

The correcting moment is dependent upon the nodal potential, unlike the force due to gravity, and is applied to the model via a current generator.

#### 5.4 Temporal and Spatial Convergence

Any TLM routine may be shown to exhibit temporal and spatial convergence if formulated correctly. The following example illustrates that convergence is achievable for the bending model. The TLM routine was executed for a cantilever of length 10cm, cross-sectional area of  $1\text{cm}^2$ , density of  $1\text{gcm}^{-3}$  and viscosity,  $\eta$ , of  $10^5\text{gcm}^{-1}\text{s}^{-1}$ . A nodal separation of 1cm was used and the angular deformation at the end of the cantilever, after a time period of 0.1s, is plotted in figure 5.21 for decreasing timesteps.

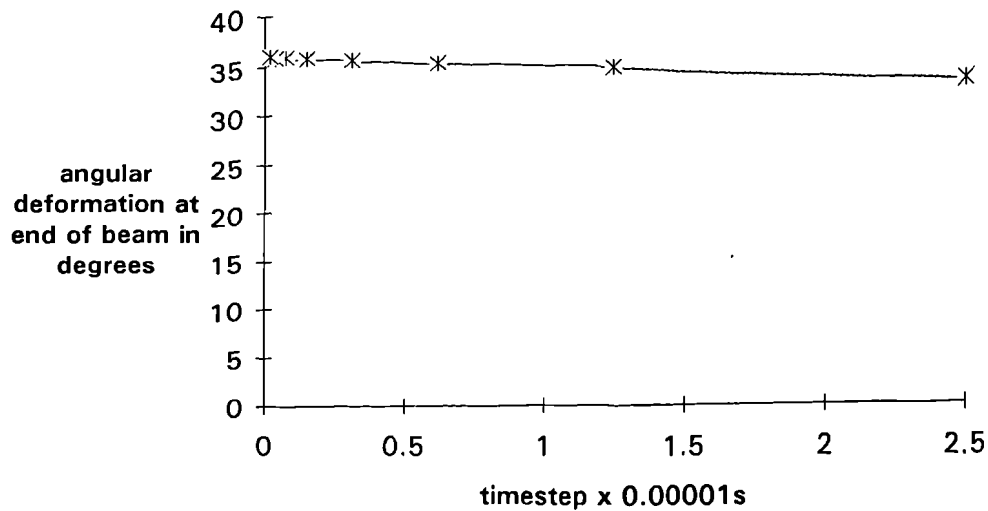


Figure 5.21 Graph of convergence of angular deformation as  $\delta t$  is decreased successively by a factor of 0.5.

Clearly, as the timestep is decreased the angular deformation increases and tends to a converged value.

In any numerical modelling technique altering the number of elements should not significantly affect the result but should serve to improve the accuracy with increased mesh refinement, until convergence has been reached. However, in the TLM modelling of the diffusion equation extra care must be taken to ensure that when reducing the spatial separation the timestep is also reduced. If the timestep is not reduced then the second order time derivative of the potential may become significant so that the routine no longer models diffusion but instead models a damped wave. This condition of consistency with modelling the diffusion equation is achieved by reducing both the spatial step and timestep such that the ratio  $\frac{\delta t}{\delta l^2}$  is kept constant, once a converged pair of  $\delta l$  and  $\delta t$  have been determined [5]. Figure 5.22 illustrates convergence for the above consistency requirement for a cantilever of length 10cm, cross-sectional area  $1\text{cm}^2$ , density  $1\text{gcm}^{-3}$  and viscosity  $10^5\text{gcm}^{-1}\text{s}^{-1}$ . The results in each case are taken after a time period of 0.1s.

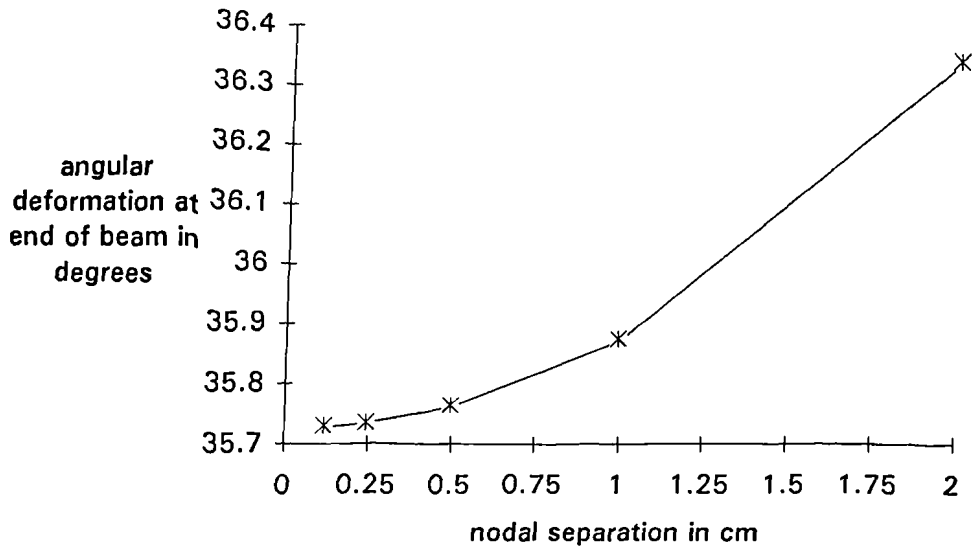


Figure 5.22 Graph showing approach to convergence as the nodal separation is decreased; the timestep is reduced by the same factor squared to satisfy consistency requirements.

### 5.5 Comparison with Finite Difference

The finite difference method allows partial differential equations to be expressed discretely and is based upon the approximation that the gradient of a curve at a point halfway between two points on the curve is equal to the mean gradient [6], as shown in figure 5.23.

The gradient of the curve  $f'(x)$  may now be expressed as

$$f'(x) = \frac{f(x+h) - f(x-h)}{2h}$$

and the second derivative may be expressed as

$$f''(x) = \frac{f(x+h) - 2f(x) + f(x-h)}{h^2}$$

where  $h = x_{i+1} - x_i$ .

The first order time derivative is expressed more simply as

$$\frac{f(x, t+\epsilon) - f(x, t)}{\epsilon}$$

where  $\epsilon$  is the time increment.

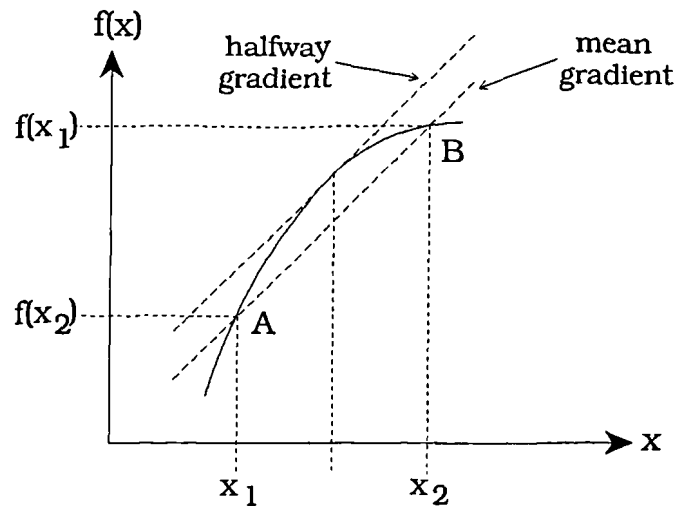


Figure 5.23 Graph illustrating the comparison of the mean and halfway gradients.

A finite difference routine may now be formulated to model the viscous equation for rotation.

$$\frac{\partial^2 I_z \omega}{\partial x^2} + \frac{\rho b h (L - x) g \cos \theta}{\lambda} = \frac{\rho}{\lambda} \frac{\partial I_z \omega}{\partial t} \quad (5.32)$$

This is achieved by rewriting equation (5.32) in discrete notation. Let  $I_z \omega(x, t)$  denote the angular momentum at a distance  $x$  along the beam and at time  $t$ , such that  $I_z = \frac{bh^3}{12}$ . The second order space differential may now be written as

$$\frac{I_z \omega(x + \delta l, t) - 2I_z \omega(x, t) + I_z \omega(x - \delta l, t)}{\delta l^2}$$

and the first order time differential may be written as

$$\frac{I_z \omega(x, t + \delta t) - I_z \omega(x, t)}{\delta t}$$

Substituting the above into equation (5.32) leads to

$$\frac{I_z\omega(x+\delta l, t) - 2I_z\omega(x, t) + I_z\omega(x-\delta l, t)}{\delta l^2} + \frac{\rho b h (L-x) g \cos\theta}{\lambda} = \frac{\rho}{\lambda} \frac{I_z\omega(x, t+\delta t) - I_z\omega(x, t)}{\delta t} \quad (5.33).$$

Rearranging equation (5.33) gives

$$I_z\omega(x, t+\delta t) = I_z\omega(x, t) + \left( \left( \frac{I_z\omega(x+\delta l, t) - 2I_z\omega(x, t) + I_z\omega(x-\delta l, t)}{\delta l^2} \right) \frac{\lambda\delta t}{\rho} \right) + g\delta t b h (L-x) \cos\theta \quad (5.34)$$

or, in terms of nodal representation where  $i\delta l$  represents the general position  $x$  and  $n\delta l$  represents the length of the beam,

$$I_z\omega(i, t+\delta t) = I_z\omega(i, t) + \left( \left( \frac{I_z\omega(i+1, t) - 2I_z\omega(i, t) + I_z\omega(i-1, t)}{\delta l^2} \right) \frac{\lambda\delta t}{\rho} \right) + g\delta t b h (n-i) \delta l \cos\theta \quad (5.35).$$

As in the TLM routine, for a cantilever the angular momentum at the support is set to zero throughout the period of flow so that at  $x=0$ ,  $I_z\omega(0, t) = 0$ . At the free end of the cantilever,  $x=L$ , the insulated boundary condition is incorporated by setting  $I_z\omega(L+\delta l, t) = I_z\omega(L, t)$ . The boundary conditions corresponding to the notation of equation (5.35) are, therefore, at  $i=1$ ,  $I_z\omega(1, t) = 0$  and at  $i=n$ ,  $I_z\omega(n+1, t) = I_z\omega(n, t)$ .

Figures 5.24 and 5.25 below show the angular deformation near the support for a cantilever bending under gravity of length 10cm, cross-sectional area of  $1\text{cm}^2$  and density of  $1\text{gcm}^{-3}$ . The TLM and finite difference routines were executed for a range of viscosities and for a time period of 0.01s, in each case using converged values of the nodal separation and iteration timestep.

From the graphs it can be seen that good agreement is obtained between the two approaches.

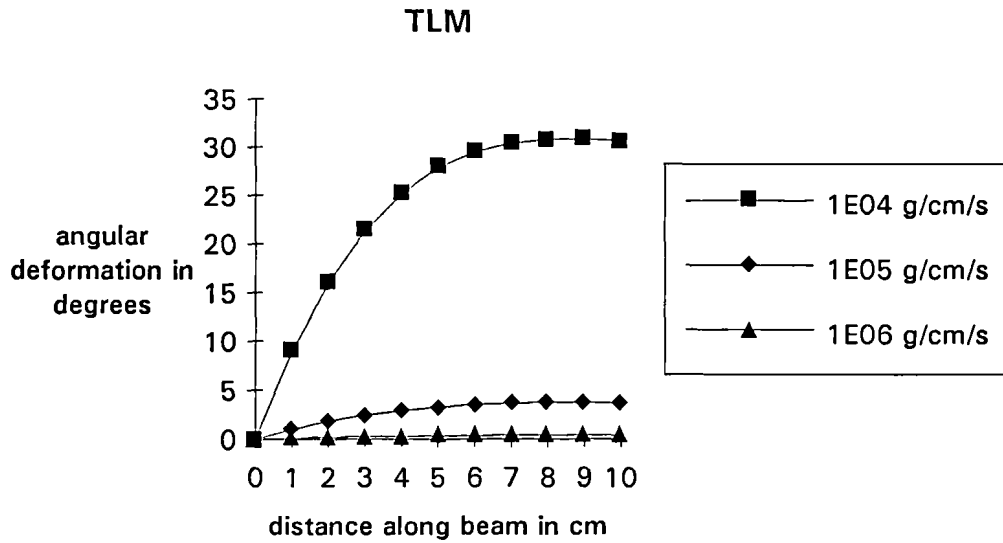


Figure 5.24 Angular deformation for different viscosities using a TLM routine.

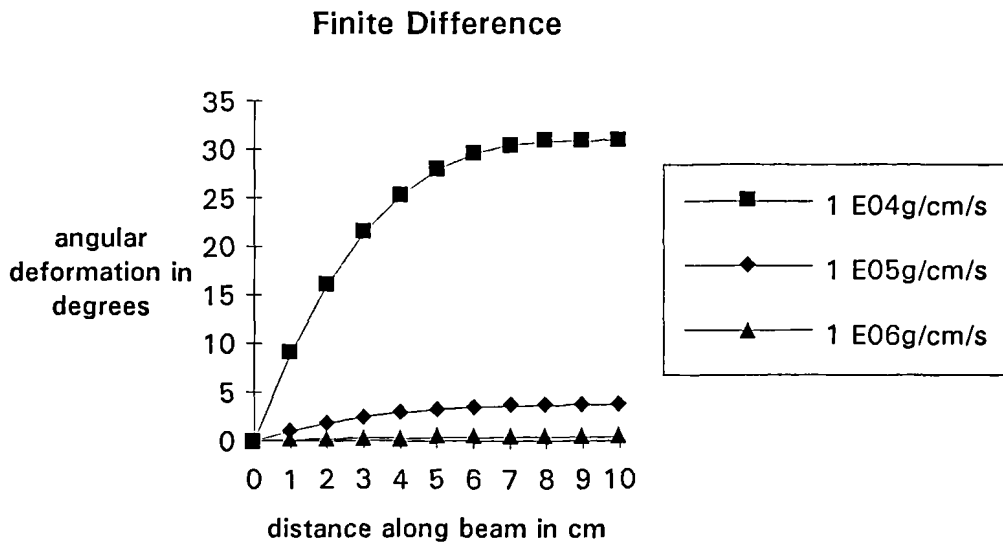


Figure 5.25 Angular deformation for different viscosities using a finite difference routine.

Figure 5.26 shows a graph of the difference in the results of figures 5.24 and 5.25. The magnitude of the discrepancy in the angular deformation increases as the amount of deformation increases, the error being no greater than 0.6%.

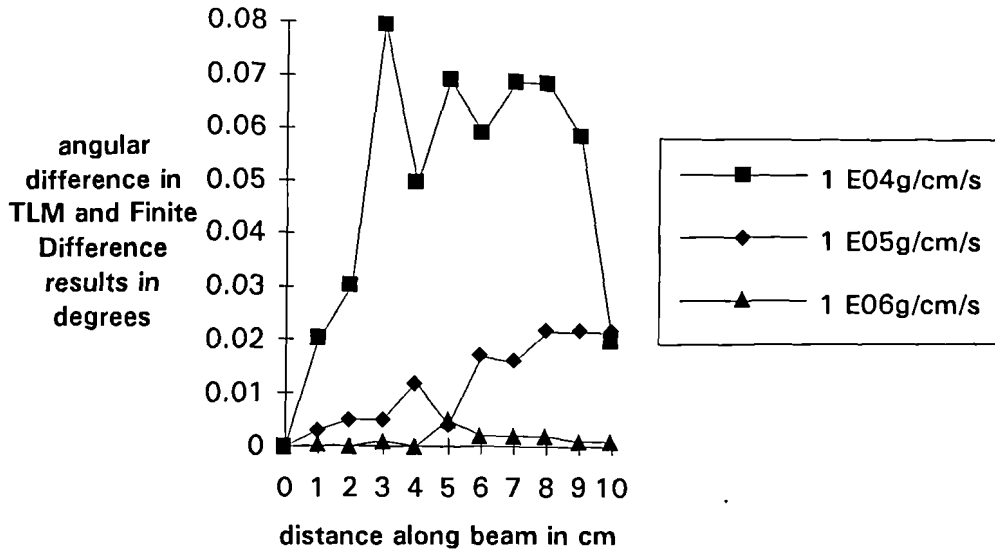


Figure 5.26 Comparison of TLM and Finite Difference results (note the vertical scale).

### 5.6 Rotation under Constant Stress

Consider a cantilever of viscous fluid that does not experience elongation as the beam deforms. If a constant shear force is applied to each element then each element is also subjected to a constant stress. Throughout the period of flow each element experiences a different but constant resultant stress. Therefore, each element in the fluid reaches a particular steady state angular velocity which is dependent upon the stress, density and viscosity.

TLM results have been obtained for a cantilever having a deformable length of 10cm, a cross-sectional area of  $1\text{cm}^2$  and a density of  $1\text{gcm}^{-3}$ . The pulses at each node  $i$  are updated by a constant value of  $\frac{(n-i)\delta l g \delta t}{2}$ , so that the beam experiences the same shearing forces as in the analytical small strain elastic solution. The angular velocity at the free end of the cantilever is plotted against time in figure 5.27 for different values of viscosity,  $\eta$ .

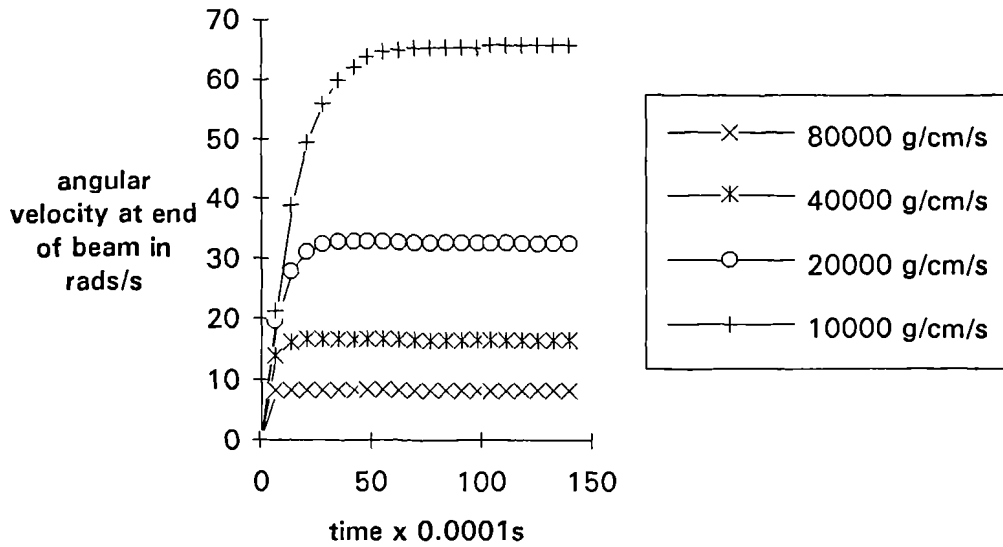


Figure 5.27 Graph of angular velocity against time for different values of viscosity, under the condition of constant applied stress.

From figure 5.27 it can be seen that under a constant shearing force, and hence constant stress, a decrease in viscosity yields a greater steady state angular velocity. This is consistent with the theoretical behaviour of a viscous fluid under constant stress, detailed in chapter 2, where  $\tau = \eta \frac{dy}{dt}$  under constant stress  $\tau$ .

Figure 5.28 depicts the variation in steady state angular velocity along the beam for different values of the coefficient of viscous traction  $\lambda$ , where  $\lambda=3\eta$ . Figure 5.29 depicts the variation in angular deformation along the beam for different values of Young's Modulus, the magnitudes of which are equal to those of the coefficients of viscous traction in figure 5.28. The elastic deformations were calculated from the analytical small strain theory detailed in section 2.4 of chapter 2.

Figure 5.30 plots the difference of the graphs of figures 5.28 and 5.29 and reveals close agreement. Therefore a viscous/elastic analogy is apparent under constant stress such that the angular velocity is analogous to the angular deformation and the coefficient of viscous traction is analogous to the Young's

Modulus [7]. The results illustrate that this analogy exists under constant stress even at low viscosities, which in the elongational model yield non-Newtonian behaviour.

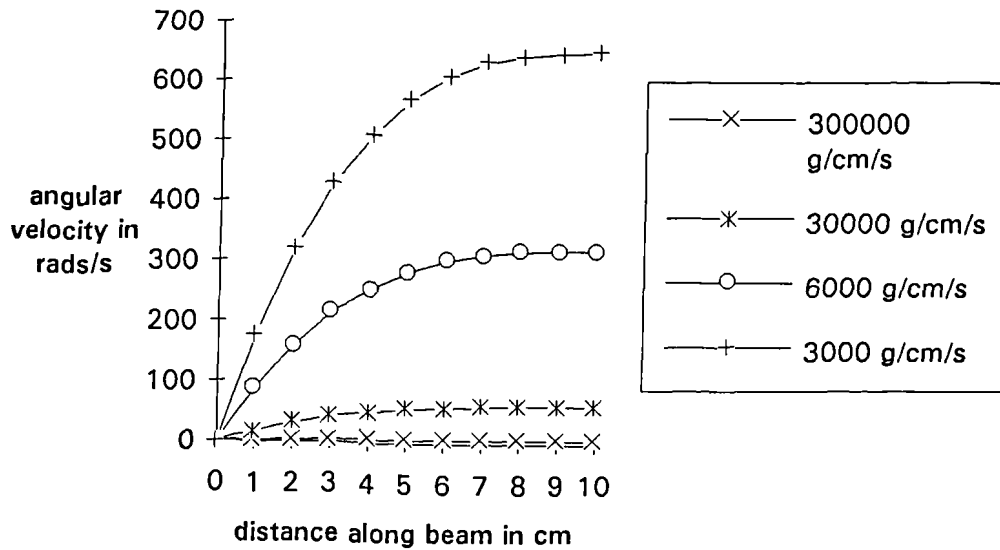


Figure 5.28 Variation of angular velocity along beams of different values of the coefficient of viscous traction, under constant stress.

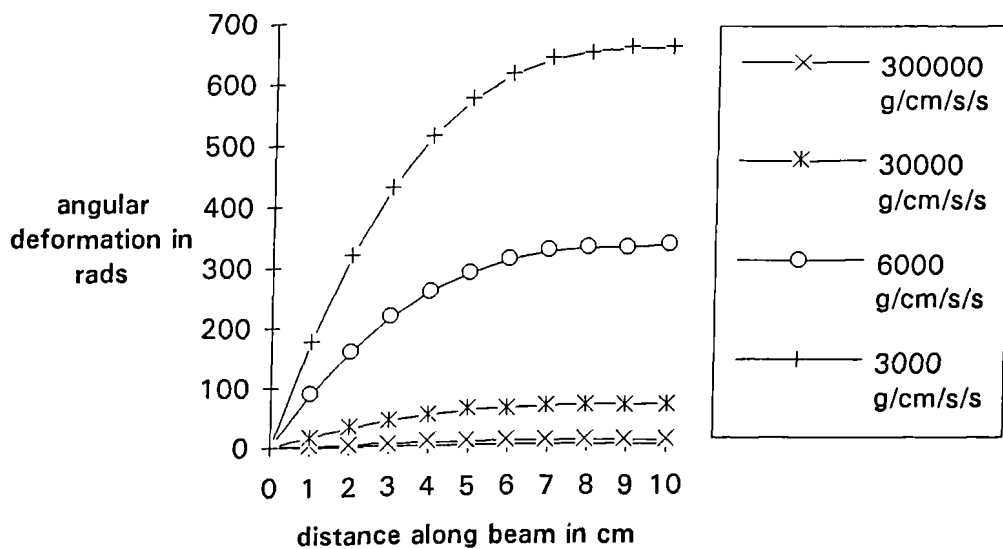


Figure 5.29 Analytical variation of angular deformation along beams of different values of Young's Modulus, under constant stress.

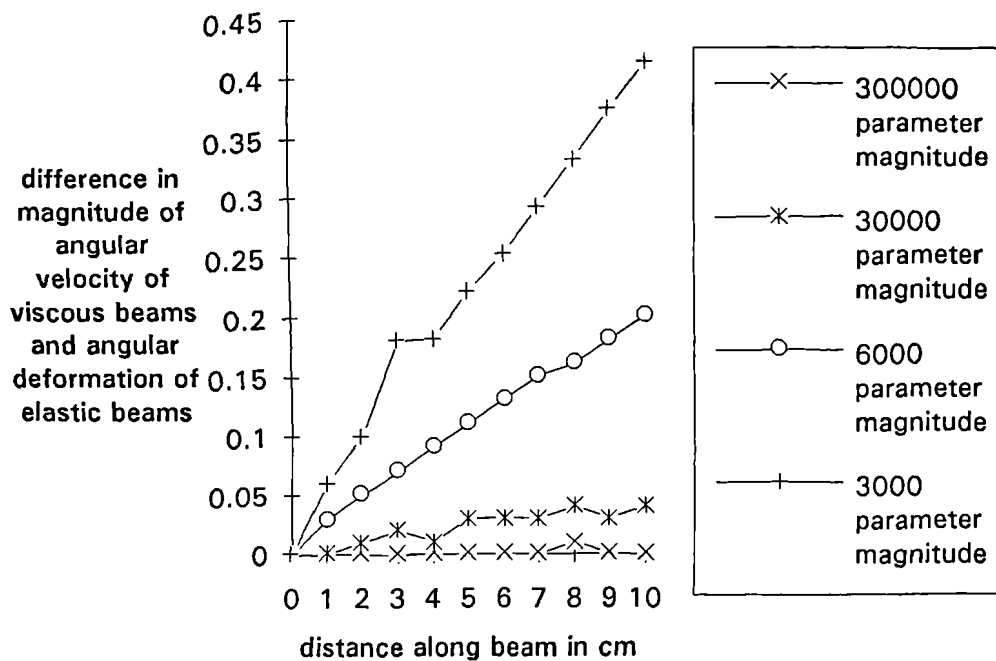


Figure 5.30 Comparison of the graphs of figures 5.29 and 5.30 revealing analogous results.

In figure 5.30 the magnitude of the discrepancy in the analogous results increases as the parameter magnitude decreases but remains less than 0.07% in each case.

From figure 5.27 it is apparent that, as well as the steady state solution, the time taken to reach a particular steady state is also parameter dependent such that a decrease in viscosity corresponds to an increase in the rise time. A low diffusivity, therefore, not only yields a large rise time but also a high steady state, so that the gradients of graphs in figure 5.27 increase as the diffusivity decreases. Modifying the material parameters not only serves to either increase or decrease the velocities reached at steady state but also characterises the variation in angular velocity along the length of the column. Thus, the resultant stress distribution within the body is also parameter dependent.

Compare the above with a rod placed in an ambient temperature of 100°C so that it is gradually heated to a steady state temperature. The time taken to reach the steady state here is also parameter dependent, such that it decreases with an increase in thermal diffusivity. The greater the thermal diffusivity the faster the thermal response of the material. However, the steady state temperature reached is independent of the thermal parameters and is uniform across the rod. Clearly, all rods of equivalent dimensions will reach the same steady state temperature of 100°C but after different periods of time, the rise times reflecting the thermal response which is parameter dependent. It therefore follows that rods of low diffusivity exhibit less steep temperature/time gradients as depicted in figure 5.31.

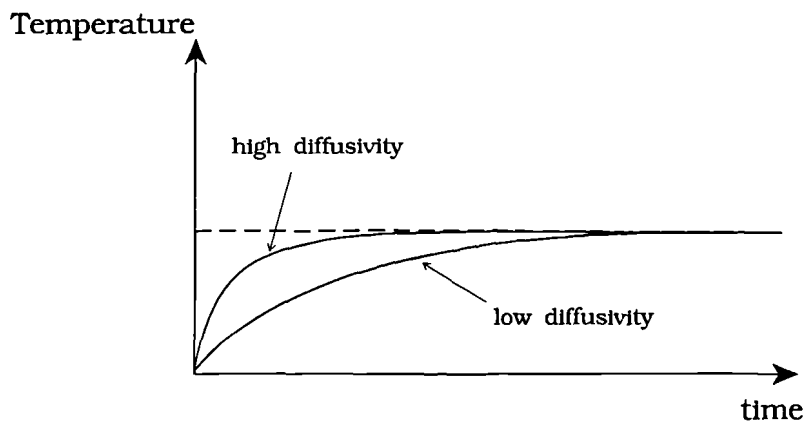


Figure 5.31 Variation of temperature with time for different diffusivities under constant ambient conditions.

In the TLM modelling of diffusion problems it is required that the term in the Telegrapher's equation containing the second order time differential of the potential is much smaller than that containing the first order time differential of the potential so that in a one-dimensional model,

$$L_d C_d \frac{\partial^2 \Phi}{\partial t^2} \ll 2R_d C_d \frac{\partial \Phi}{\partial t} \quad (5.36).$$

The ratio of these two terms may, therefore, be used as an error parameter  $m$  [8] such that

$$m = \frac{L_d C_d \frac{\partial^2 \Phi}{\partial t^2}}{2R_d C_d \frac{\partial \Phi}{\partial t}} \ll 1 \quad (5.37).$$

The impedance of the transmission lines is given by

$$Z = \sqrt{\frac{L_d}{C_d}} = \frac{\delta t}{C} \quad (5.38)$$

where  $C = C_d \delta l^3$  represents the lumped capacitance and  $R_d$  represents the lumped resistance.

Equation (5.38) allows substitution for  $L_d$  in (5.37) and representing the

lumped resistance by  $R = \frac{R_d \delta l}{2\delta l^2}$ , together with the expression for  $C$  above

leads to

$$m = \frac{\delta t^2 \frac{\partial^2 \Phi}{\partial t^2}}{4RC\delta l^4 \frac{\partial \Phi}{\partial t}} \quad (5.39).$$

Inspection of the transient of figure 5.29 leads to the following general equation for each of the curves;

$$\Phi = A \left( 1 - \exp\left(\frac{-t}{RC}\right) \right) \quad (5.40)$$

where  $\Phi$  represents the temperature at time  $t$  and  $A$  is the steady state temperature.

From (5.39) it follows that

$$\frac{\partial \Phi}{\partial t} = \frac{A}{RC} \exp\left(\frac{-t}{RC}\right) \quad (5.41)$$

and

$$\frac{\partial^2 \Phi}{\partial t^2} = -\frac{A}{(RC)^2} \exp\left(\frac{-t}{RC}\right) \quad (5.42)$$

so that the expression for  $m$  now becomes

$$m = \frac{\delta t^2}{4(RC)^2 \delta l^4} \quad (5.43).$$

Clearly, for a constant error and constant  $\delta l$ , a low value of  $RC$  demands a smaller value of  $\delta t$  than a correspondingly higher value of  $RC$ .

Equation (5.43) also yields the accuracy requirement that for constant  $RC$  a constant error is maintained if when reducing  $\delta l$  the timestep  $\delta t$  is chosen

so that the ratio  $\frac{\delta t}{\delta l^2}$  is constant [5].

A fluid of high viscosity, although of a slow steady state flow rate, exhibits a fast stress response and therefore a fast rate of change of velocity since the resistance to the diffusion is inversely proportional to the viscosity. The fluid has a low  $RC$  value and, therefore, from equation (5.43) must be modelled using a smaller timestep than fluids of lower viscosities to ensure accuracy. The requirement that bodies of slow deformation rates be modelled using small timesteps is clearly unfortunate if it is desired to simulate their behaviour over long periods of time. The accuracy requirement also dictates that a fast deforming body may be sampled less frequently than a body that is deforming more slowly. However, the choice of timestep for a body of high deformation rate should not be chosen so large that crucial information is missed.

The development of the total stress response under gravity is achieved faster in a highly viscous fluid, in fact in the limit of infinite viscosity the total stress response time is infinitesimal so that the total stresses may be considered to be developed instantaneously, at the same time there being infinitesimal resulting flow. This situation may be compared with an elastic body where, in

the formulation of the equations for the pure bending of an elastic cantilever, each section instantaneously experiences the total shearing force of the weight of the beam beyond that section [9]; the development of the elastic stresses not being time dependent.

### 5.7 Coupled Viscous Model

In general, a viscous body deforming under gravity will exhibit both aspects of elongation and bending as detailed in sections 5.2 and 5.4 respectively. A model reflecting the full behaviour of such a body involves the coupling of two TLM meshes; one describing the elongation and the other describing the rotation. In a coupled model each mesh feeds information into the other. Thus, the elongation affects the magnitude of the rotation and the angular inclination affects the component of gravity promoting elongational flow. The elongation directly modifies the resistance which is modelled identically in each network. The full action of gravity upon a general element, inclined at an angle  $\theta$ , is depicted in figure 5.32.

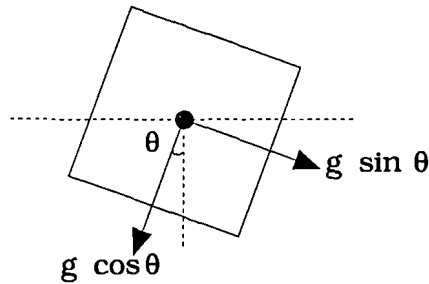


Figure 5.32 Viscous element subject to both elongation and rotation.

The component of gravity promoting elongation is now  $g \sin \theta$  so that the following expressions for the pulses in the two meshes apply:

$$\begin{aligned}
 \text{Elongation mesh:} \quad & V_i = V_i + \frac{g \delta t \sin \theta}{2} \\
 \text{Rotation mesh:} \quad & V_i = V_i + \frac{V(i) \delta t \cos \theta}{2\rho b h} \quad (5.44)
 \end{aligned}$$

where  $V(i)$  represents the shear force on a general element  $i$ .

When the viscosity of the beam is high the shear force may be replaced by  $\rho b h(L-x)g$  so that the pulses in the rotation mesh become

$$v_i = v_i + \frac{(L-x) g \delta t \cos\theta}{2} \quad (5.45)$$

and the coupling incorporates the changes in shear stress due to changes in length and hence changes in cross-sectional area. When the viscosity is low the shearing forces  $V(i)$  must be obtained from tractive forces in a vertical elongation model so that shear stresses due to both the magnitude of the viscosity and the dimensional changes are incorporated via the coupling.

### 5.8 Meshing and Beams of Initial Curvature

TLM meshes for the vertical column, cantilever and simply supported beam are one dimensional and therefore consist of a 'string' of nodes. Thermal bodies which can be modelled adequately by a one dimensional treatment are those which are insulated along their entire length. Consider a rod of length  $L$ , cross-sectional area  $A$  and density  $\rho$ . The rod has thermal conductivity  $K$ , specific heat capacity  $S$  and heat transfer coefficient  $H$ . If the rod is insulated along its length and subject to identical heat sources at each end, as depicted in figure 5.33, then after a certain period of time a uniform temperature gradient is established; the temperature at each point along the rod being the same as that of the heat sources. The time taken to reach this steady state is dependent upon the dimensions of the rod and its material parameters.

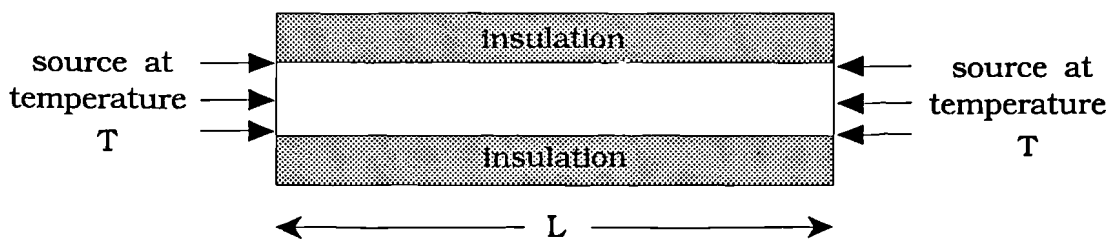


Figure 5.33 Insulated rod subjected to constant heat sources at each end.

Consider now an identical rod which, although of the same length  $L$  and cross-section  $A$ , has a different curvature as shown in figure 5.34. Under the same heating conditions as before the curved rod will acquire an identical uniform temperature distribution and in the same time period as for the straight rod. In fact, an identical rod of any curvature will reach the same steady state in the same time period. Thus, the transfer of heat along an insulated rod is independent of curvature. It therefore follows that a curved insulated rod can be modelled as a straight insulated rod of equivalent length and cross-section.

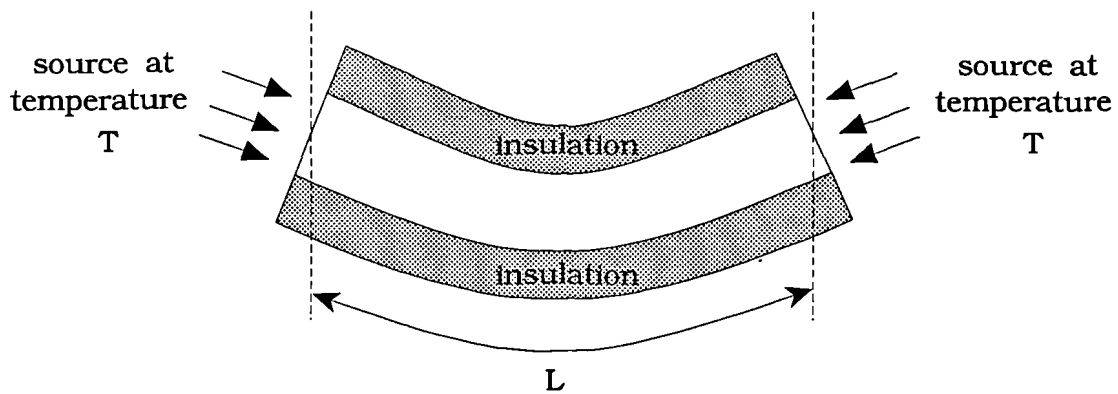


Figure 5.34 Insulated curved rod subjected to constant heat sources at each end.

A TLM mesh representing an insulated rod of any curvature is shown in figure 5.35, illustrating that the arrangement of resistors and transmission lines in the network is independent of element orientation.

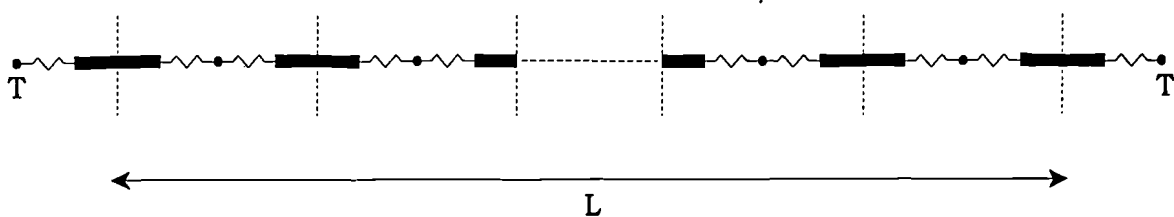


Figure 5.35 Curvature-independent TLM mesh.

Consider now a viscous column, cantilever and simply supported beam. Each beam may be modelled by a one dimensional TLM mesh; the structure of which, as in the case of an insulated rod, being independent of curvature. Although the meshing itself is independent of curvature the effect of gravity upon each of the bodies is not, so that the pulses in the network effectively incorporate the curvature into each model. It follows then that throughout the modelling period of a cantilever or simply supported beam the associated TLM mesh does not change its structure even though the beams themselves are deforming; it is only the values of R, Z and the incident pulses which alter.

Clearly then, beams having initial curvature may also be modelled using the same mesh structure as above, with the initial orientation of each element being incorporated in the pulses at the beginning of the modelling period. Figure 5.36 depicts a curved beam having initial angular orientation  $\theta_i$  at a general node  $i$ .

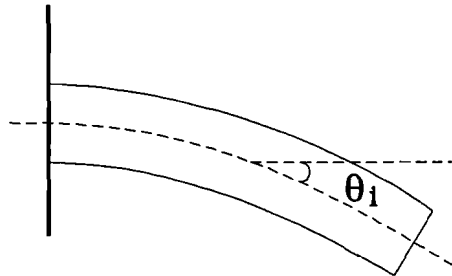


Figure 5.36 Curved beam supported as a cantilever.

The pulses at a general node are, therefore, given by

$$V_i = V_i + \frac{(n-i)\delta l g \delta t \cos\theta_i}{2} \quad (5.46).$$

The weight to the right of element  $i$  is given by  $(n-i)\delta l A \rho g$  but is now inclined at an angle  $\theta_i$ .

It is assumed here that the initial state of the beam is such that the beam has either been formed with an initial curvature or that it has been pre-deformed to this state by, for example, elastic deformation.

## 5.9 Incorporation of Elasticity

### 5.9.1 Elasticity in series

The Maxwell model for the series combination of viscoelasticity has been described earlier in section 2.5 of chapter 2. This model consists of initial elastic deformation followed by viscous flow. Incorporation of series elasticity to the viscous TLM model is very straightforward. The elastic deformation of a cantilever, for example, may be calculated analytically using the classical theory detailed in section 2.4.2 of chapter 2. This deformation may be used as the starting point for the viscous flow so that in the TLM routine the viscous deformation is applied to an initially curved beam. The resultant deformation, therefore, consists of elastic strain followed by viscous strain so that  $\gamma_{\text{total}} = \gamma_{\text{elastic}} + \gamma_{\text{viscous}}$ .

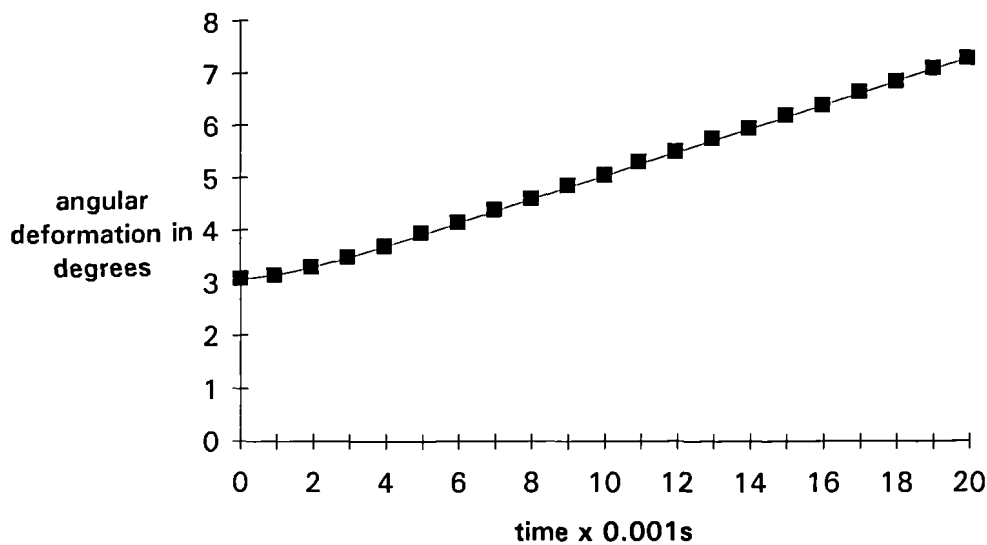


Figure 5.37 Graph of angular deformation against time under constant applied stress for a series viscoelastic beam, obtained from the TLM model.

Figure 5.37 shows the angular deformation near the support for a cantilever of length 10cm, cross-sectional area of  $1\text{cm}^2$  and density of  $1\text{gcm}^{-3}$ . The value of Young's Modulus of Elasticity in series,  $E_s$ , is  $10^7 \text{gcm}^{-1}\text{s}^{-2}$  and

the viscosity,  $\eta$ , is  $10^4 \text{ gcm}^{-1}\text{s}^{-1}$ . The cantilever is subjected to a constant shear force  $V = \rho b h \delta l g$ , and hence constant stress as no elongation occurs.

### 5.9.2 Elasticity in parallel

The Kelvin model represents a parallel combination of viscosity and elasticity, such that the elastic and viscous stresses are additive. That is, the total shear stress  $\tau_{\text{total}}$  is given by

$$\tau_{\text{total}} = \tau_{\text{elastic}} + \tau_{\text{viscous}} \quad (5.47).$$

It will be recalled that in the bending viscous model the stress is incorporated by means of an applied potential  $\Phi'$  such that

$$\tau_{\text{viscous}} = \tau_{\text{total}} = \frac{\text{shear force}}{\text{area}} = \frac{1}{bh\delta l} C \frac{\partial \Phi'}{\partial t} = \rho \frac{\partial \Phi'}{\partial t} \quad (5.48)$$

where for a cantilever  $\Phi' = g(n-i)\delta l \cos\theta t$  and is modelled by the pulses according to

$$V^i = V^i + \frac{(n-i)\delta l \cos\theta g \delta t}{2} \quad (5.49).$$

Therefore, in a parallel viscoelastic model

$$\tau_{\text{total}} = \tau_{\text{elastic}} + \rho \frac{\partial \Phi'}{\partial t} \quad (5.50)$$

which leads to

$$\frac{\partial \Phi'}{\partial t} = \frac{(\tau_{\text{total}} - \tau_{\text{elastic}})}{\rho} \quad (5.51)$$

or, in terms of the pulses,

$$V^i = V^i + \frac{(\tau_{\text{total}} - \tau_{\text{elastic}})\delta t}{2\rho} \quad (5.52).$$

The state of zero applied viscous stress is achieved in the model when

$$\frac{\partial \Phi'}{\partial t} = 0$$

resulting in  $\tau_{\text{total}} = \tau_{\text{elastic}}$  so that the TLM routine yields the elastic solution.

Now, from chapter 2,

$$\theta = \frac{1}{EI_z} \int_0^s M ds = \frac{\rho g (n-i) \delta l \cos\theta}{\rho g (n-i) \delta l \cos\theta EI_z} \int_0^s M ds \quad (5.53)$$

where  $I_z = \frac{bh^3}{12}$ .

Rearranging equation (5.53) yields

$$\rho g (n-i) \delta l \cos\theta = \frac{\theta EI_z \rho g (n-i) \delta l \cos\theta}{\int_0^s M ds} \quad (5.54)$$

so that  $\tau_{total} = \tau_{elastic}$ .

Substituting for  $\tau_{total}$  and  $\tau_{elastic}$  in equation (5.52) now yields the form of the incident pulses for parallel viscoelastic flow;

$$V^i = V^i + \frac{g (n-i) \delta l \delta t \cos\theta}{2} - \frac{\theta EI_z g (n-i) \delta l \delta t \cos\theta}{2 \int_0^s M ds} \quad (5.55)$$

which may be written as

$$V^i = V^i + \frac{g (n-i) \delta l \delta t \cos\theta}{2} - \frac{\theta(i)}{\theta_{elastic}(i)} \frac{g (n-i) \delta l \delta t \cos\theta}{2}$$

$$\text{where } \theta_{elastic} = \frac{\int_0^s M ds}{EI_z} \quad (5.56).$$

The viscous equation incorporating parallel elasticity is, therefore, given by

$$\frac{\partial^2 I_z \omega}{\partial x^2} + \frac{\rho (n-i) \delta l bh g \cos\theta}{\lambda} \left( 1 - \frac{\theta(i)}{\theta_{elastic}(i)} \right) = \frac{\rho}{\lambda} \frac{\partial I_z \omega}{\partial t} \quad (5.57).$$

This formulation assumes that the parallel viscoelastic behaviour is performed upon a beam whose initial angular deformation is zero along its

entire length. If the initial angular orientation is denoted by  $\theta_o(i)$  then equation (5.56) becomes

$$V^i = V^i + \frac{g(n-i)\delta l \delta t \cos\theta}{2} - \frac{(\theta(i) - \theta_o(i))}{\theta_{\text{elastic}}(i)} \frac{g(n-i)\delta l \delta t \cos\theta}{2} \quad (5.58).$$

The parallel viscoelastic angular deformation of a cantilever may be calculated where  $\int_0^s M ds = \frac{\rho b h g}{6} (s^3 - 3s^2L + 3sL^2)$  using the elastic solution from equation (2.71) in chapter 2,  $s$  being the distance along the beam. Graphs of angular deformation, at 1cm from the support, are plotted against time in figure 5.38 for a cantilever of length 10cm, cross-sectional area  $1\text{cm}^2$ , density  $1\text{gcm}^{-3}$  and viscosity  $10^4 \text{gcm}^{-1}\text{s}^{-1}$ . The value of parallel elasticity,  $E_p$ , in the graphs ranges from  $10^6 \text{gcm}^{-1}\text{s}^{-2}$  to  $10^8 \text{gcm}^{-1}\text{s}^{-2}$ .

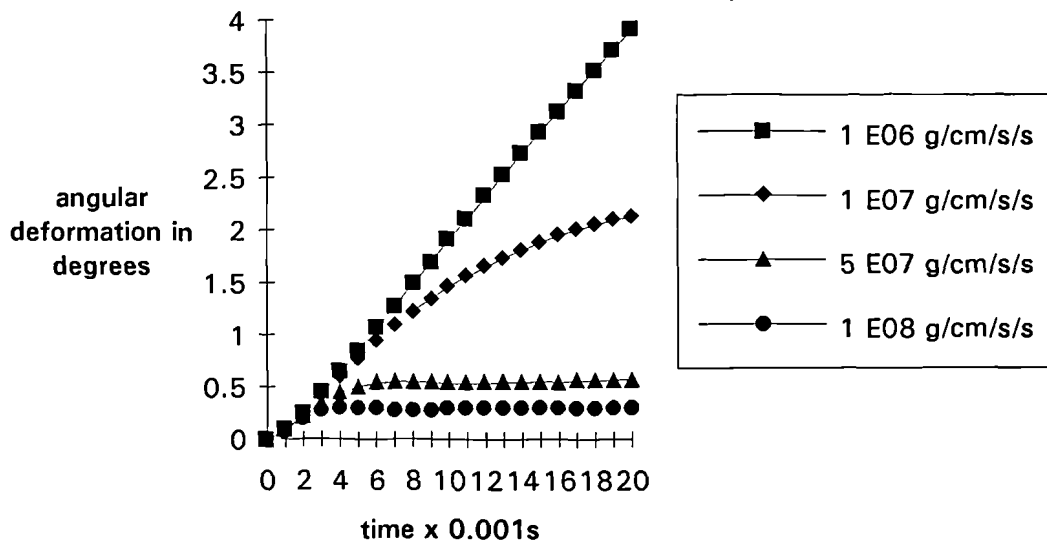


Figure 5.38 TLM graphs of angular deformation against time under constant bending moment for different values of parallel elasticity,  $E_p$ .

The graphs of figure 5.38 show that the greater the value of  $E_p$  the quicker the steady state is reached. For  $E_p = 10^8 \text{gcm}^{-1}\text{s}^{-2}$  it can be seen that slight oscillations occur before the steady state is reached. These oscillations

arise because of the low viscosity of the beam and illustrate the true damped wave type of behaviour.

Clearly, viscoelastic models may be formed for beams of any shape provided that either the path of integration or the elastic angular deformation is known.

Theoretical results obtained from small strain theory display a proportionality between the inverse of Young's Modulus and the angular deformation. Thus, according to this theory, a cantilever of low elasticity may have a steady state solution such that the free end of the beam deforms beyond  $90^\circ$  to the horizontal. Clearly, this is not a realistic solution as the beam would in fact hang so that the end of the beam lies at an angle of  $90^\circ$  to the horizontal. The graphs depicted in figure 5.39 compare results obtained from the parallel viscoelastic TLM model when run to steady state against theoretical small strain results where the angular deformation is given by

$$\theta = \frac{6\rho g}{Eh^2} \left( L^2x - x^2L + \frac{x^3}{3} \right).$$

The cantilever is of length 10cm, cross-sectional area  $1\text{cm}^2$  and density  $1\text{gcm}^{-3}$ .

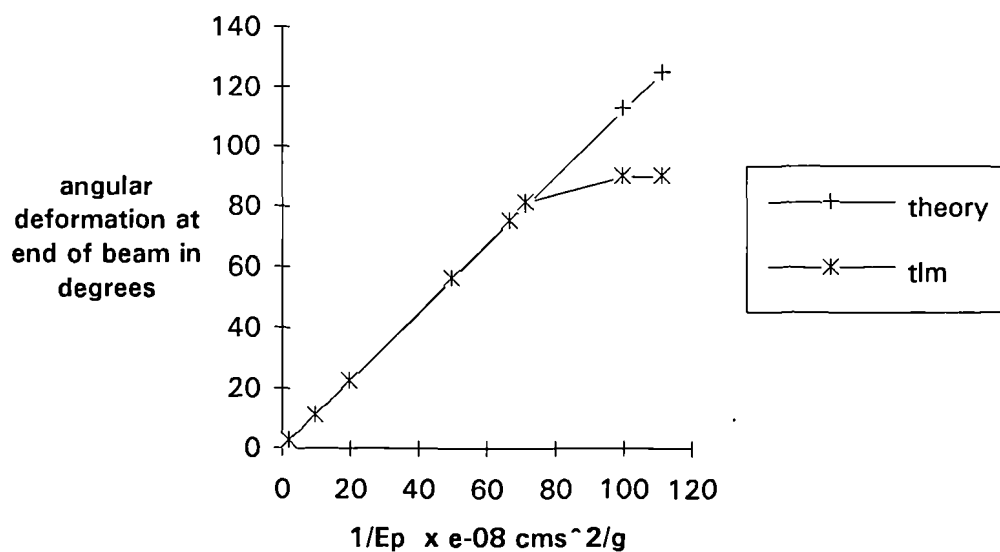


Figure 5.39 Comparison of steady state TLM elastic solution with small strain theory for decreasing values of Young's Modulus,  $E_p$ .

The TLM results show good agreement with small strain theory for high values of Young's Modulus, that is for theoretical angular deformations less than  $90^\circ$ . As the Young's Modulus is decreased further the TLM results predict vertical deformation at the end of the beam and, therefore, more accurately represent the true deformation.

### 5.9.3 Combinations of series and parallel elasticity

Three and four component viscoelastic models, as described in chapter 2, can now be constructed by effectively 'fitting' together the appropriate types of flow and deformation. Figure 5.40 shows a three component model consisting of an elastic spring in series with a parallel combination of a viscous dashpot and a second elastic spring. A graph of strain against time for such a model under constant stress is plotted in figure 5.41 and illustrates the behaviour upon removal of the stress. The results have been obtained for a cantilever of the same dimensions and density as above. The viscosity of the beam is  $10^4 \text{ gcm}^{-1}\text{s}^{-1}$ , with  $E_s = 10^8 \text{ gcm}^{-1}\text{s}^{-2}$  and  $E_p = 10^7 \text{ gcm}^{-1}\text{s}^{-2}$ , the angular deformation being that at 1cm from the support. The load is removed at  $t=0.2\text{s}$ .

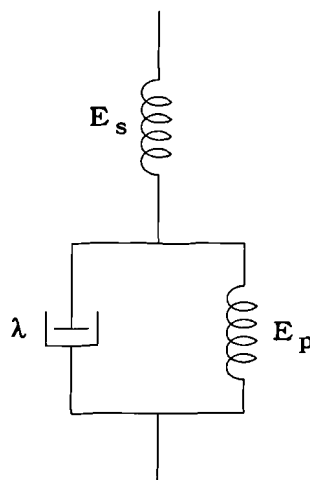


Figure 5.40 A three component viscoelastic model.

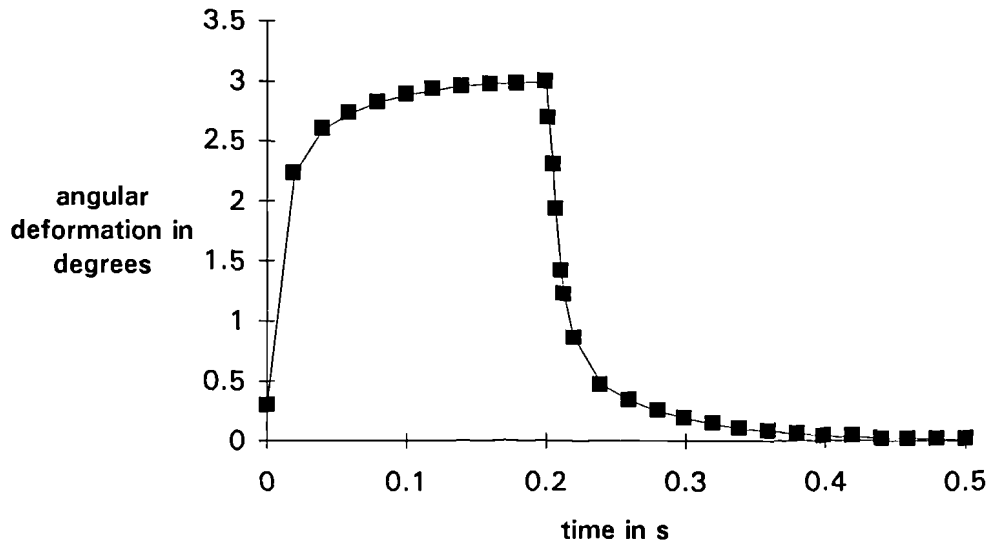


Figure 5.41 Graph of angular deformation against time under constant applied stress for the three component TLM viscoelastic model. The load is removed at 0.2s.

The graph of figure 5.41 can be seen to be in agreement with the theoretical results of figure 2.25a in chapter 2. A three component model comprising a viscous dashpot in replacement of the series elastic spring in figure 5.40 is achieved by running two TLM routines simultaneously over the period of deformation; one for the series viscous flow and the other for the parallel viscoelastic deformation. The routines are coupled since the strains are additive and appear in the loading terms of each routine. A four component model consisting of initial elasticity, followed by viscous flow and finally parallel viscoelastic flow is simply a series combination of initial elastic deformation followed by the three component viscoelastic mechanism described above.

## 5.10 Viscous Deformation in Two Dimensions

The general approach taken to model the deformation of viscous beams may also be applied to two dimensional plates and shells. As in elastic theory the rigidity of a plate is assumed to be increased by a factor dependent upon the value of Poisson's Ratio,  $\nu$ , for the material. The rigidity of an elastic two dimensional plate was shown in section 2.4.3 of chapter 2 to be

$$D = \frac{E h^3}{12 (1-\nu^2)} = EI'_z \quad (5.59)$$

where  $E$  is the Young's Modulus,  $h$  is the plate thickness and  $I'_z$  is the modified area moment of inertia.

It follows from (5.59) that the area moment of inertia,  $I_z = \frac{bh^3}{12}$ , for the deformation of beams, given in section 5.3, must be replaced by

$$I'_z = \frac{h^3}{12(1-\nu^2)} \quad (5.60).$$

The two dimensional viscous equation for pure bending is

$$\frac{\partial^2 I'_z \omega}{\partial x^2} + \frac{\partial^2 I'_z \omega}{\partial y^2} + \frac{\rho b h (n_x - i) \delta l g \cos \theta}{\lambda} = \frac{\rho}{\lambda} \frac{\partial I'_z \omega}{\partial t} \quad (5.61)$$

so that all four incident pulses are updated each iteration by

$$\frac{(n_x - i) \delta l g \delta t \cos \theta}{2} \quad (5.62)$$

where  $n_x \delta l$  represents the length of the cantilever.

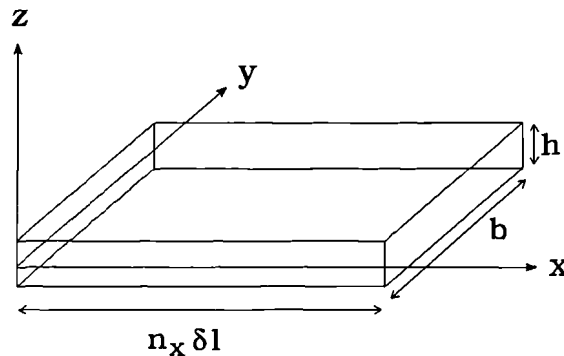


Figure 5.42 Two dimensional cantilever supported at the left along the  $y$  axis.

The general equation of a two dimensional diffusion network is, from chapter 3,

$$\frac{\partial^2 \Phi}{\partial x^2} + \frac{\partial^2 \Phi}{\partial y^2} = 4 R_d C_d \frac{\partial \Phi}{\partial t} \quad (5.63)$$

so that the resistance of the TLM network is now modelled by

$$R = \frac{\text{elemental length}}{4 \lambda \text{ cross-sectional area}} \quad (5.64)$$

and the line impedance is given by

$$Z = \frac{2\delta t}{C} \quad (5.65)$$

where  $C = \rho \times \text{elemental volume}$ , as two whole transmission lines equally share the capacitance of an element.

This formulation allows the modelling of asymmetric deformation as observed when the viscosity of a plate varies in the  $y$  direction, provided that the variation is not so great that the shearing in this direction becomes significant. A variation in viscosity along the length of a beam using the one-dimensional formulation is easily achieved simply by incorporating the appropriate value in the resistance. Alternatively, modelling the viscosity in the capacitance would necessitate the use of stubs to account for the variation along the beam. A viscosity variation in the  $y$  direction of a two dimensional plate supported as a cantilever, as depicted in figure 5.42, would produce a change in curvature in both the  $x$  and  $y$  dimensions of the plate; the viscosity variation having an effect upon the deformation in the  $x$  direction. Plates having initial curvature in both the  $x$  and  $y$  dimensions may also be modelled by equation (5.61), provided that the curvature in the  $y$  direction is slight so that shearing forces in the direction of the width are not significant. Plates supported not only along the width but also along the length in the  $x$  direction may have significant shearing forces in each of the two dimensions so that a cross spatial derivative term would need to be present in the diffusion equation

to account for the torsional bending. The Navier-Stokes equations relate the velocity components in each of the three dimensions under constant pressure as follows [11],

$$\begin{aligned}
\rho \left( \frac{\partial v_x}{\partial t} + v_x \frac{\partial v_x}{\partial x} + v_y \frac{\partial v_y}{\partial y} + v_z \frac{\partial v_z}{\partial z} \right) &= \rho g_x - \frac{\partial}{\partial x} \left( \frac{2}{3} \eta \left( \frac{\partial v_x}{\partial x} + \frac{\partial v_y}{\partial y} + \frac{\partial v_z}{\partial z} \right) \right) + \\
&\quad \eta \left( \frac{\partial^2 v_x}{\partial x^2} + \frac{\partial^2 v_y}{\partial y \partial x} + \frac{\partial^2 v_z}{\partial z \partial x} \right) + \eta \left( \frac{\partial^2 v_x}{\partial x^2} + \frac{\partial^2 v_x}{\partial y^2} + \frac{\partial^2 v_x}{\partial z^2} \right) \\
\rho \left( \frac{\partial v_y}{\partial t} + v_x \frac{\partial v_x}{\partial x} + v_y \frac{\partial v_y}{\partial y} + v_z \frac{\partial v_z}{\partial z} \right) &= \rho g_y - \frac{\partial}{\partial y} \left( \frac{2}{3} \eta \left( \frac{\partial v_x}{\partial x} + \frac{\partial v_y}{\partial y} + \frac{\partial v_z}{\partial z} \right) \right) + \\
&\quad \eta \left( \frac{\partial^2 v_x}{\partial x \partial y} + \frac{\partial^2 v_y}{\partial y^2} + \frac{\partial^2 v_z}{\partial z \partial y} \right) + \eta \left( \frac{\partial^2 v_y}{\partial x^2} + \frac{\partial^2 v_y}{\partial y^2} + \frac{\partial^2 v_y}{\partial z^2} \right) \\
\rho \left( \frac{\partial v_z}{\partial t} + v_x \frac{\partial v_x}{\partial x} + v_y \frac{\partial v_y}{\partial y} + v_z \frac{\partial v_z}{\partial z} \right) &= \rho g_z - \frac{\partial}{\partial z} \left( \frac{2}{3} \eta \left( \frac{\partial v_x}{\partial x} + \frac{\partial v_y}{\partial y} + \frac{\partial v_z}{\partial z} \right) \right) + \\
&\quad \eta \left( \frac{\partial^2 v_x}{\partial x \partial z} + \frac{\partial^2 v_y}{\partial y \partial z} + \frac{\partial^2 v_z}{\partial z^2} \right) + \eta \left( \frac{\partial^2 v_z}{\partial x^2} + \frac{\partial^2 v_z}{\partial y^2} + \frac{\partial^2 v_z}{\partial z^2} \right)
\end{aligned} \tag{5.66}$$

In each of the above equations the left hand side may be written as  $\rho \frac{Dv_x}{Dt}$ ,

$\rho \frac{Dv_y}{Dt}$  and  $\rho \frac{Dv_z}{Dt}$  respectively and in the case of incompressible flow

$\frac{\partial v_x}{\partial x} + \frac{\partial v_y}{\partial y} + \frac{\partial v_z}{\partial z} = 0$ , so that the equations reduce to

$$\begin{aligned}
\rho \frac{Dv_x}{Dt} &= \rho g_x + \eta \left( \frac{\partial^2 v_x}{\partial x^2} + \frac{\partial^2 v_x}{\partial y^2} + \frac{\partial^2 v_x}{\partial z^2} \right) \\
\rho \frac{Dv_y}{Dt} &= \rho g_y + \eta \left( \frac{\partial^2 v_y}{\partial x^2} + \frac{\partial^2 v_y}{\partial y^2} + \frac{\partial^2 v_y}{\partial z^2} \right) \\
\rho \frac{Dv_z}{Dt} &= \rho g_z + \eta \left( \frac{\partial^2 v_z}{\partial x^2} + \frac{\partial^2 v_z}{\partial y^2} + \frac{\partial^2 v_z}{\partial z^2} \right)
\end{aligned}
\tag{5.67}.$$

It is evident that each equation requires the velocity components in each of the three dimensions so that the coupling of three velocity meshes would be required for the complete solution.

The incorporation of both series and parallel elasticity into the basic two dimensional viscous model of equation (5.61) is achieved as set out for the one dimensional case in section 5.10; the appropriate analytical elastic solutions being two dimensional. In cases where a fuller description of the deformation is required, the elastic equations will take a similar form to the three dimensional viscous equations above so that they incorporate the complete three dimensional behaviour.

### 5.11 Formulation of an Elastic Bending Model

The static solution of the deformation of an elastic cantilever under its own weight is given by

$$EI_z \frac{d^2\theta}{dx^2} = \rho b h (L - x) g \tag{5.68}.$$

In order that equation (5.68) may be modelled by a TLM routine, time dependency must be introduced. As it stands the above equation is one of an

equilibrium of forces, so that time dependency may be introduced by re-writing (5.68) as an equation of motion as follows,

$$EI_z \frac{\partial^2 \theta}{\partial x^2} + \rho b h (L - x) g \cos \theta = \rho I_z \frac{\partial^2 \theta}{\partial t^2} \quad (5.69)$$

where the introduction of the transient has allowed the implementation of the component of gravity,  $g \cos \theta$ , as the beam deforms.

Rearrangement of (5.69) leads to

$$\frac{\partial^2 I_z \theta}{\partial x^2} + \frac{\rho b h (L - x) g \cos \theta}{E} = \frac{\rho}{E} \frac{\partial^2 I_z \theta}{\partial t^2} \quad (5.70)$$

where it should be noted that the loss of the negative sign in front of the gravitational term is due to assuming that for the solution the double integration is now performed along the beam in the opposite direction.

Equation (5.70) represents an elastic wave of Young's modulus  $E$  and velocity  $\sqrt{\frac{E}{\rho}}$ , and describes an elastic cantilever vibrating under the effect of gravity. The steady state solution of (5.70) is given by equation (5.68) and may be obtained from equation (5.70) if a damping term is introduced, such that

$$\frac{\partial^2 I_z \theta}{\partial x^2} + \frac{\rho b h (L - x) g \cos \theta}{E} = \frac{\rho}{E} \frac{\partial^2 I_z \theta}{\partial t^2} + \frac{\lambda}{E b h} \frac{\partial I_z \theta}{\partial t} \quad (5.71).$$

The damping term is proportional to the coefficient of viscous traction  $\lambda$  and the angular velocity of the wave. A high viscosity increases the damping and brings the beam to rest with fewer oscillations than for a lower viscosity. Although the transient is dependent upon the viscosity, the steady state solution is independent of the value of viscosity so that equation (5.71) may be used to obtain static elastic solutions.

Comparison of the viscous equation (5.18) and the damped elastic equation (5.71) reveals a similar loading term so that, again, the pulses model the effect of gravity. The angular inclination of the beam is, therefore,

represented by the pulses and not by the mesh structure, so that the elastic model may be applied to beams of initial curvature as detailed in section 5.8 for the viscous model.

The corresponding one dimensional damped wave equation for the TLM network is given by

$$\frac{\partial^2 \Phi}{\partial x^2} + 2 R_d C_d \frac{\partial \Phi'}{\partial t} = L_d C_d \frac{\partial^2 \Phi}{\partial t^2} + 2 R_d C_d \frac{\partial \Phi}{\partial t} \quad (5.72).$$

Comparison of equations (5.71) and (5.72) yields the following network parameters

$$\begin{aligned} \Phi &= I_z \theta \\ C_d &= \frac{\rho}{E} \\ 2R_d &= \frac{\lambda}{\rho b h} \end{aligned} \quad (5.73)$$

so that the distributed inductance is of unit magnitude.

The incident pulses take the following form,

$$V^i = V^i + 0.5 \left( \frac{\rho (bh)^2 (n-i) \delta l g \cos \theta \delta t}{\lambda} \right) \quad (5.74)$$

and the boundary conditions are identical to those for the viscous bending model, with a zero potential at the clamped end of the beam and a perfectly reflecting boundary at the free end.

Figure 5.43 compares elastic solutions obtained from a TLM formulation of equation (5.71) with those obtained from small strain elastic theory for a beam of length 10cm, cross-sectional area 1cm<sup>2</sup> and density 1gcm<sup>-3</sup>.

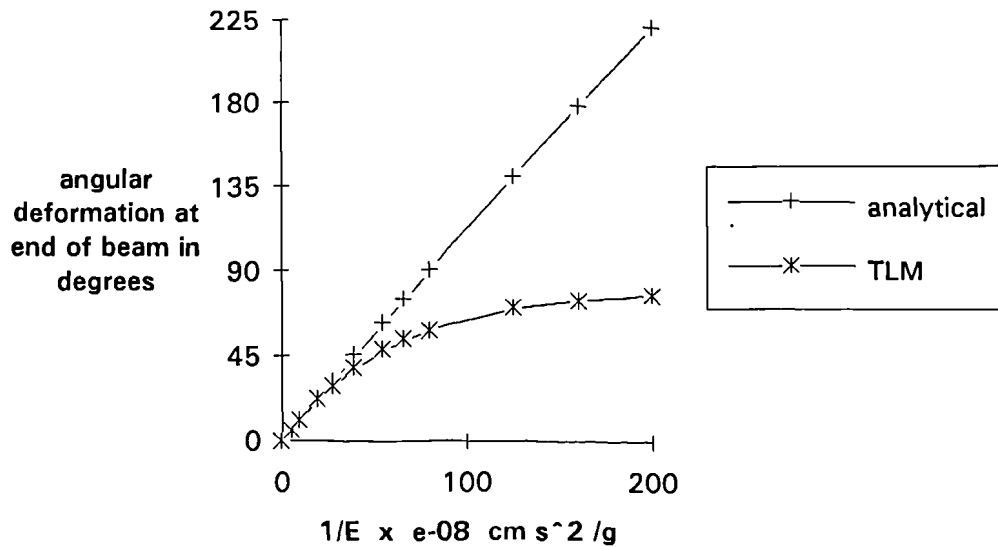


Figure 5.43 Comparison of TLM and analytical elastic solutions.

Comparison of the analytical and TLM steady state solutions of figure 5.43 shows agreement for small deformations but shows a discrepancy at low values of elasticity when the angular deformation becomes significant and  $\cos\theta$  is much smaller than 1. The solutions from the elastic TLM routine give angular deformations which are less than those from the viscous based parallel viscoelastic model in figure 5.37 as the elasticity decreases, although both models show the maximum deformation tending to  $90^\circ$  as the elasticity tends to zero. The TLM elastic routine is considered to yield the most accurate results since deviation from the analytical solution commences at angles whose cosine values dictate a significant reduction in the gravitational component. The steady state graph of the parallel viscoelastic model does not begin to deviate significantly from that of the analytical solution until the deformation reaches approximately  $80^\circ$ , which implies that although the  $\cos\theta$  dependency of the routine behaves correctly as a limiting factor it does not, however, accurately influence the magnitude of the stresses acting on the beam.

## 5.12 References

- [1] F T Trouton, "On the Coefficient of Viscous Traction and its Relation to that of Viscosity", *Proceedings of the Royal Society*, vol 77, pp 426-440, 1906.
- [2] M Reiner, *Deformation, Strain and Flow*, pp 78-85, 2nd edition, H K Lewis & Company Ltd, London, 1960.
- [3] S P Banks, *Control Systems Engineering*, pp 212-214, Prentice-Hall International (UK) Ltd, 1986.
- [4] G F Franklin, J D Powell & M. L. Workman, *Digital Control of Dynamic Systems*, pp 222-229, 2nd edition, Addison-Wesley Publishing Company, Inc, 1990.
- [5] P Johns and G Butler, "The Consistency and Accuracy of the TLM Method for Diffusion and its Relationship to Existing Methods", *International Journal for Numerical Methods in Engineering*, vol 19, pp 1549-1554, 1983.
- [6] B M Irons and N G Shrive, *Numerical Methods in Engineering and Applied Science: Numbers are Fun*, Chapters 2&8, Ellis Horwood Ltd, 1987.
- [7] M Reiner, *Deformation, Strain and Flow*, H.K Lewis & Company Ltd, London, chapter V, 1960.

- [8] S H Pulko, A Mallik, R Allen and P B Johns, "Automatic Timestepping in TLM Routines for the Modelling of Thermal Diffusion Processes", *International Journal of Numerical Modelling: Electronic Networks, Devices and Fields*, vol 3, pp 127-136, 1990.
- [9] S Timoshenko, *Strength of Materials, Part I, Elementary Theory and Problems*, 3rd edition, Robert E Krieger Publishing Company, New York, pp 141, 1976.
- [10] J G Freeman, "Mathematical Theory of Deflection of Beam", *Philosophical Magazine and Journal of Science*, vol 37, pp 855-862, 1945.
- [11] J R Welty, C E Wicks and R E Wilson, *Fundamentals of Momentum, Heat, and Mass Transfer*, third edition, John Wiley & Sons, pp 123-128, 1984.

## CHAPTER 6

### APPLICATION OF TLM MODELS TO CERAMICS

Existing models of deformation, suitable for application to ceramics, are discussed. Evidence of viscoelastic behaviour at high temperatures is provided allowing the applicability of models to the firing of sanitary ware to be addressed. Ceramic testpieces are introduced for which the analytical elastic solutions are given. Finally, deformation results from viscoelastic TLM routines for the various testpieces are compared with experimental results.

## 6.1 Existing Deformation Models

Previous methods designed to predict deformation of ceramics during firing have assumed either purely viscous or purely elastic behaviour. McDowall and Vose [1] based their method upon the analogy of steady state viscous flow and elastic deformation under constant stress. Instead of considering an equation of motion for the viscous flow, they assume that a viscous body is subject to the same stress as an elastic body under gravity and that the equations of equilibrium applied to the bending of elastic beams may be applied to those of a viscous nature. This leads to the replacement of the Young's Modulus,  $E$ , in the bending equations by the product of the coefficient of viscous traction and the period of deformation,  $\lambda t$ . Subsequently, the expression for the central sag of a simply supported viscous rod is shown to depend upon the dimensions of the rod and the material properties of density and viscosity over a given heating schedule, as shown by equation (6.1).

$$\text{Sag} = \frac{L_{TF}^4}{d_{TF}^2} \left( \int_t^{t_F} \frac{15 g \rho_{TF} f(T)}{8 \lambda} dt \right) \quad (6.1)$$

where

$f(T)$  is a function dependent upon the temperature and material of the ceramic;

$L_{TF}$  is the length of the rod at the final firing temperature  $T_F$  ;

$d_{TF}$  is the diameter at the final firing temperature;

$\rho_{TF}$  is the density at the final firing temperature;

$\lambda$  is the coefficient of viscous traction;

the integral is performed over the period during which significant sagging occurs,  $t_F$  denoting the time at which the maximum firing temperature is reached.

The integral expression in equation (6.1) is assumed to be constant for a ceramic rod during a specific firing schedule and is termed the Pyroplastic Index. This constant provides a measure of the amount of deformation during firing; the higher the value the greater the deformation. Adcock, Drummond and McDowall [2] have applied this approach to a variety of test pieces, each of different geometry. Although the investigators claim good agreement with experiment for their particular clay body McNabb and Duncan [3] highlight that discrepancies with experiment were obtained when the theory was put into general industrial practice. These authors also consider the deformation arising from viscous flow but incorporate temperature effects and internal stresses which may result in additional deformation independent of the gravitational force, such as the yielding of ware towards regions of higher temperature. The basic equations vary only slightly from those of Adcock et al, using a modified expression for the Pyroplastic Index which includes a dependence on porosity. Gaillard et al [4] take a purely elastic approach to the modelling of a porcelain plate even though a high vitreous phase content is observed. A finite element code is employed which assumes linear elastic behaviour and considers only steady states. Young's Modulus is temperature dependent and isotropic. Shrinkage is incorporated and results for a single plate are claimed to be in perfect accord with experiment. However, it is suggested that the simplified approach be developed to take into account the viscoelastic behaviour of the material.

## **6.2 Viscoelastic Behaviour at High Temperatures**

Evidence of the viscoelastic behaviour of ceramics at high temperatures is well documented [5-9]. Experiments have been devised to determine the behaviour of bodies when subject to constant stresses, such as torsion testing and flexural bending. Uniaxial testing, although commonly applied to metals

and polymers, is not favoured for ceramics because of the necessity for high temperature grips which are not readily available. The application of compression testing is limited because of the tendency for specimens to buckle and subsequently fail. However, such tests have been successfully carried out on a kaolinite body [5] and show that ultimately the deformation under compression is proportional to time, yielding steady flow under constant stress. Initial behaviour reflects that of a parallel viscoelastic combination, the deformation occurring at a faster rate than that displayed during the period of Newtonian flow which follows.

In flexure it has been found that steady state creep is not easily achieved [6]; some materials may be subjected to bending for up to 1200 hours and still fail to display signs of approaching steady state. This behaviour sheds doubt on the general applicability of the viscous modelling approach employed by McDowall and Vose [1] where steady state flow is assumed throughout bending. Bending tests carried out on pre-fired refractories at high temperatures further limit the applicability of the viscous approach, revealing departure from the linear relationship between deformation and load prior to fracture [7]. At temperatures in the region of 1300°C the stress/strain behaviour is highly non-linear being viscoelastic in nature even though the deformation at room temperature is shown to be elastic until brittle fracture occurs.

The creep data obtained for a particular ceramic under each type of testing may not, in general, be in agreement; the response under compression being different from that under tension and in bending [6,8]. This highlights the importance of carrying out the appropriate test according to the service requirements of the body.

All the above experimentation has been carried out on pre-fired ceramics at high temperatures and implies that similar behaviour may be expected at high temperatures during firing. In fact, torsion testing of sanitary

ware bodies during firing has been shown to reveal a viscoelastic response [9]. The testing was performed over a range of temperatures from room temperature up to a firing temperature of 1200°C and results from 800°C onwards are clearly indicative of three component viscoelastic behaviour with initial elasticity. As the temperature is increased, under constant applied torque, the results reveal an increase in the initial elastic deformation and an increase in flow rate, indicating a decrease in both the series and parallel values of Young's Modulus as well as a decrease in the viscosity. Glass is known to be viscoelastic at all temperatures [10] and experimental results for viscosities in the region of  $10^{13}$  gcm<sup>-1</sup>s<sup>-1</sup> indicate stress relaxation behaviour for a range of silicate glasses. Three component viscoelastic behaviour is consistent with that obtained when a glass fibre is subjected to stretching; a slowly applied strain rate allows stretching, or flow, whereas a rapidly applied strain rate will cause the fibre to break before flow is established. This behaviour is reflected in glass forming operations for viscosities as low as  $10^4$  gcm<sup>-1</sup>s<sup>-1</sup>, where the speed of application of the plunger can drastically affect the build up of stresses in the glass. These elastic stresses may yield localised imperfections or even fracture if considerable.

The viscoelastic behaviour of all ceramic bodies is dependent upon composition and must be determined experimentally. A three component viscoelastic model displaying initial elastic deformation, however, may provide an adequate representation for the behaviour of most viscoelastic materials [11].

It is now not unreasonable to assume that deformation under the action of gravity during the firing process may also be represented by such a viscoelastic model.

### 6.3 Applicability of Deformation Models During Firing Cycle

In all of the existing models described earlier the deformation during firing is assumed to occur during the heating of the ware up to the maximum firing temperature. Comparison of three sanitary ware formulations during firing has been shown to reveal a change in behaviour due to an increase in rigidity on cooling [9]. Investigation of the viscoelastic behaviour yielded greater flow during the heating cycle, highlighting a reduced temperature dependence for viscosity and Young's Modulus on cooling. The rigidity on cooling was found to be significantly greater for the formulation with the highest quartz content which, although considerably viscoelastic at 1000°C on heating, behaved as though essentially rigid at the same temperature during cooling. Results obtained from the high temperature torsion testing of porcelain bodies also indicate a higher viscosity during cooling [12]. The rigidity of these bodies, therefore, is greatly enhanced so that negligible deformation may be assumed to occur after vitrification. Once cooling begins all phase reactions terminate with porosity close to zero and firing shrinkage constant. The types of problems which occur during cooling are those affecting the appearance of the ware such as dunting, commonly associated with the  $\alpha$ - $\beta$  quartz inversion [13]. Thermal stresses may also remain in the ware which if considerable cause shattering. The cooling cycle, therefore, may be assumed to play an insignificant role in the deformation of the ware and may be disregarded in simulations.

### 6.4 Variation of Viscosity and Elasticity During Firing

Viscosity varies with temperature according to

$$\eta = A T \exp\left(10^3 \frac{B}{T}\right) \quad (6.2)$$

where A and B are parameters dependent upon the composition of the melt [14]. Values of viscosity for various silicate melts at temperatures around 1300°C have been determined [14] and lie in the region of  $10^4 - 10^5 \text{ gcm}^{-1}\text{s}^{-1}$ . The same viscosity range has also been determined for whiteware compositions during the glassy phase [15]. At the beginning of a firing cycle the temperature of the article is very low so that the viscosity has a near infinite value. The viscosity decreases to a minimum value over a time period of approximately 10 hours, this minimum value being reached at the maximum firing temperature. The variation of viscosity during the firing cycle and the length of time that the ware is held at each temperature is important with regard to the product quality and appearance.

Examination of the RC time constant for the TLM model in chapter 5 has revealed that bodies of high viscosity must be modelled using very small timesteps. This can be seen to be extremely unfortunate for the modelling of the viscosity range above, where the higher viscosities, and their associated long time periods, necessitate timesteps so small that run times would be unacceptably large. However, this problem may be overcome by considering the stress / strain rate relationship for viscous flow,

$$\tau = \eta \frac{d\gamma}{dt} \quad (6.3).$$

Clearly, under constant stress  $\tau$ , a number of pairs of values of  $\eta$  and  $\frac{d\gamma}{dt}$  exist

that satisfy equation (6.3). Therefore, if  $\eta_1, \frac{d\gamma_1}{dt}$  and  $\eta_2, \frac{d\gamma_2}{dt}$  are two such pairs of values then it follows that

$$\frac{\eta_1}{\eta_2} = \frac{\frac{d\gamma_2}{dt}}{\frac{d\gamma_1}{dt}} \quad (6.4).$$

Both pairs of values will yield the same strain  $\gamma$  if the periods of flow,  $t_1$  and  $t_2$ , satisfy

$$\frac{t_1}{t_2} = \frac{\eta_1}{\eta_2} \quad (6.5).$$

As an example, consider  $\tau = 10^6 \text{ gcm}^{-1}\text{s}^{-2}$ . Then for  $\eta_1 = 10^{10} \text{ gcm}^{-1}\text{s}^{-1}$  it follows that  $\frac{d\gamma_1}{dt} = 10^{-4} \text{ s}^{-1}$  and for  $\eta_2 = 10^5 \text{ gcm}^{-1}\text{s}^{-1}$  it follows that

$\frac{d\gamma_2}{dt} = 10 \text{ s}^{-1}$ . If the strains  $\gamma_1$  and  $\gamma_2$  are to be equal and the first flow period

is  $t_1 = 10^7 \text{ s}$  then  $\gamma_1 = 10^3 = \gamma_2$ , yielding  $t_2 = 10^2 \text{ s} = t_1 \frac{\eta_2}{\eta_1}$ .

The stress / strain rate behaviour is clearly advantageous in the TLM model, allowing highly viscous bodies to be modelled equivalently by lower viscosities provided that the modelling viscosity is not so low that the equivalence relation breaks down. The breakdown of the stress / strain rate equivalence coincides with the viscosity at which the body begins to deform before the full distribution of the stresses has occurred, as illustrated in the results of the elongating viscous columns in chapter 5. Figure 6.1 shows a typical variation in the angular strain rate under constant stress for both a high and a low value of viscosity, as generated by the TLM model.

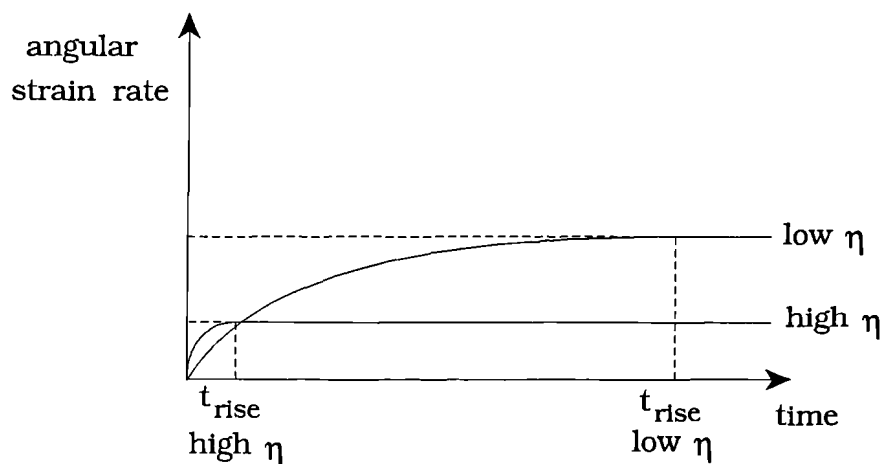


Figure 6.1 Graph of angular strain rate against time for high and low viscosities.

The steady state is reached in each case when  $t = t_{\text{rise}}$  so that for  $0 \leq t \leq t_{\text{rise}}$  the graph follows an exponential curve and for  $t \geq t_{\text{rise}}$  the graph is constant.

Therefore, for  $t \leq t_{\text{rise}}$

$$\frac{d\gamma}{dt} = \frac{\tau}{\eta} \left( 1 - \exp\left(\frac{-t}{RC}\right) \right) \quad (6.6)$$

and, for  $t \geq t_{\text{rise}}$

$$\frac{d\gamma}{dt} = \frac{\tau}{\eta} \quad (6.7).$$

If the modelling time period is less than  $t_{\text{rise}}$  then clearly a higher value of viscosity must be chosen so that the stress / strain rate equivalence holds.

The variation in viscosity throughout the firing cycle may be represented by a series combination of Newtonian viscous flows each yielding a strain  $\gamma_i$  after their period of flow  $t_i$ , as depicted in figure 6.2.

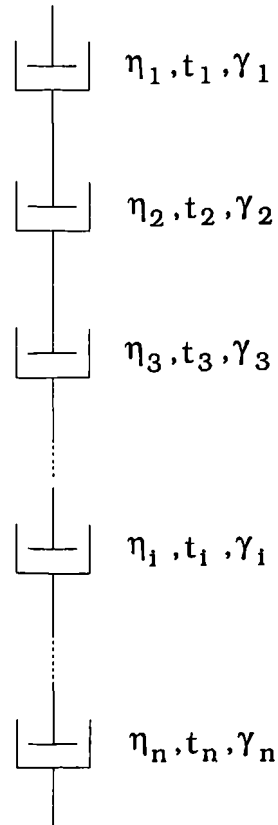


Figure 6.2 A series combination of viscous flows over time .

The above combination may be replaced by a single constant value of viscosity and time period, which is calculated from the equivalence relation, such that the total strain  $\gamma$  satisfies  $\sum_{i=1}^n \gamma_i = \gamma$ . Figures 6.3a and 6.3b illustrate such a flow replacement under the condition of constant stress.

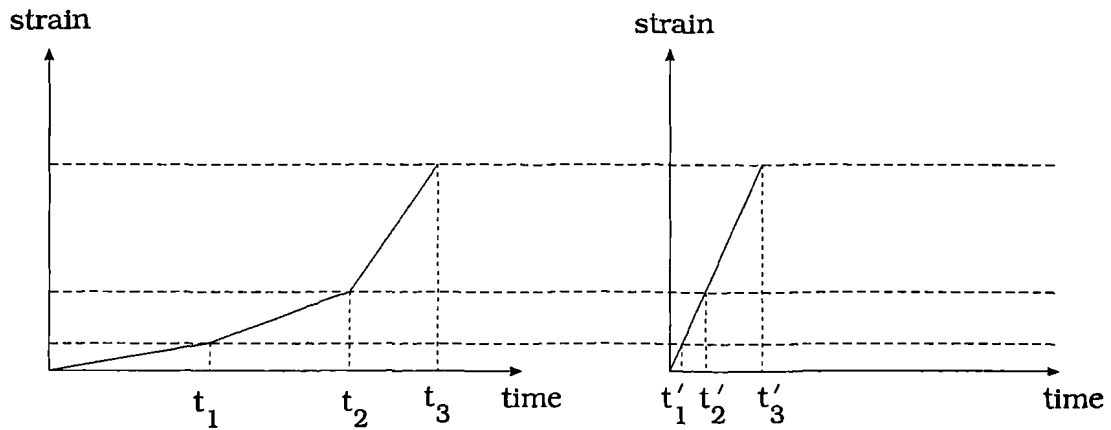


Figure 6.3a Varying viscosity

Figure 6.3b Constant viscosity

It is evident from figures 6.3a and 6.3b that although the strain rate differs between the two graphs, the strain and hence, during bending under gravity, the angular deformation,  $\theta$ , remains the same so that  $\cos\theta$  and hence the stress is also modelled accurately throughout the deformation using the constant viscosity approach .

A body which may be represented by a three-component viscoelastic mechanism exhibits such behaviour under any load and also, therefore, under a time varying load. As a body bends under gravity it experiences a decrease in load due to the increase in angular deformation, so that at each moment in time the body responds with its three-component viscoelastic behaviour. Figure 6.4 illustrates such a series combination of three-component viscoelastic flows. The parameters with subscript n denote those values at the maximum firing

temperature, so that  $\lambda_1$  is greater than  $\lambda_2$  is greater than  $\lambda_n$ , and similarly for the elastic moduli.

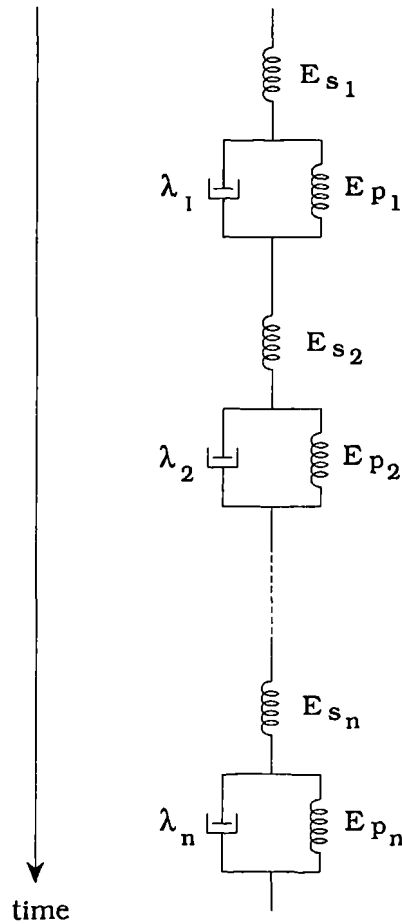


Figure 6.4 Three-component viscoelastic behaviour with time dependent parameters.

Due to the problem of modelling high viscosities, the above series combination must be rearranged so that the complete behaviour may be modelled most efficiently by the TLM deformation model. For simplicity it will be assumed initially that the same stress  $\tau$  acts on each of the series components. This assumption allows the lumping together of all the elastic deformations resulting from the series elastic moduli,  $E_{s_i}$ , so that their summed

deformation  $\gamma_s = \sum_{i=1}^n \gamma_{s_i}$  may be performed at time  $t=0$  from a single

elastic modulus value  $E_s$ . It now follows that  $\gamma_s$  may be expressed in terms of  $E_s$  as

$$\gamma_s = \frac{\tau}{E_s} = \sum_{i=1}^n \frac{\tau}{E_{s_i}} = \sum_{i=1}^n \gamma_{s_i} \quad (6.8)$$

where it is apparent that the single elastic modulus  $E_s$  is related to the series values  $E_{s_i}$  by

$$\frac{1}{E_s} = \sum_{i=1}^n \frac{1}{E_{s_i}} \quad (6.9).$$

Figure 6.5 depicts the modified representation of figure 6.4 such that the total deformation is equal, although the transient deformation differs.

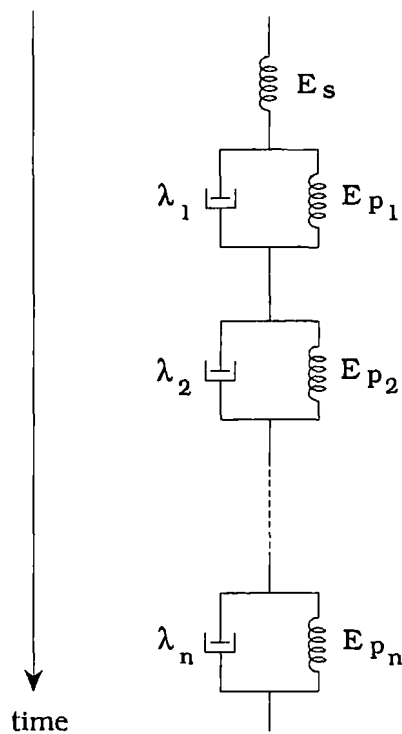


Figure 6.5 Time dependent three-component viscoelastic behaviour with initial lumped elasticity.

It is now evident from figure 6.5 that the viscosity values  $\lambda_i$  are in series and therefore may be replaced by a constant viscosity value  $\lambda$ , in the manner described earlier. The consequence of altering the viscosity is an

alteration to the time scale  $t'$  which is calculated according to equation (6.5) so that the ratio of  $\frac{t_i}{\lambda_i}$  is kept constant. The series three-component combination with constant viscosity and corresponding new time scale is depicted in figure 6.6.

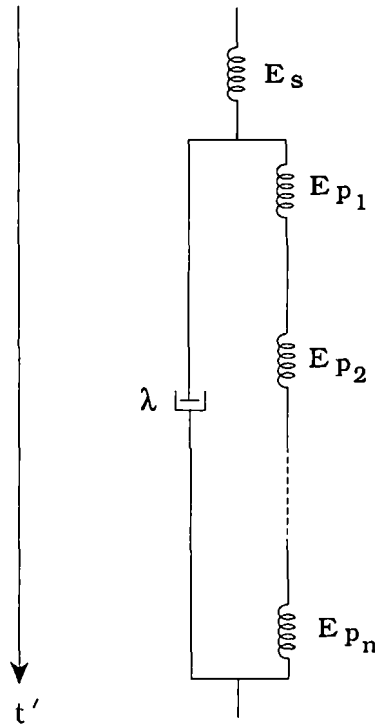


Figure 6.6 Three-component viscoelastic combination with constant viscosity and modified time period,  $t'$ .

The strain of a parallel viscoelastic combination is given by

$$\gamma_{p_i} = \frac{\tau}{E_{p_i}} \left( 1 - \exp\left(\frac{-E_{p_i} t_i}{\lambda_i}\right) \right) \quad (6.10)$$

and is clearly unaffected by the appropriate modification of both the viscosity and the time period.

The parallel elastic moduli  $E_{p_i}$  are also in series so that their strains are additive, allowing the replacement by a single elastic modulus  $E_p$  such that

$$\frac{1}{E_p} = \sum_{i=1}^n \frac{1}{E_{p_i}} \quad (6.11).$$

Consider two consecutive parallel viscoelastic flows of viscosity  $\lambda$  and parallel elastic moduli  $E_{p1}$  and  $E_{p2}$ , of duration  $t_1$  and  $t_2$  respectively. The strain is given by the following equations and is depicted in figure 6.7a.

$$\gamma = \frac{\tau}{E_{p1}} \left( 1 - \exp\left(\frac{-E_{p1}t}{\lambda}\right) \right) \quad \text{for } 0 < t < t_1$$

and

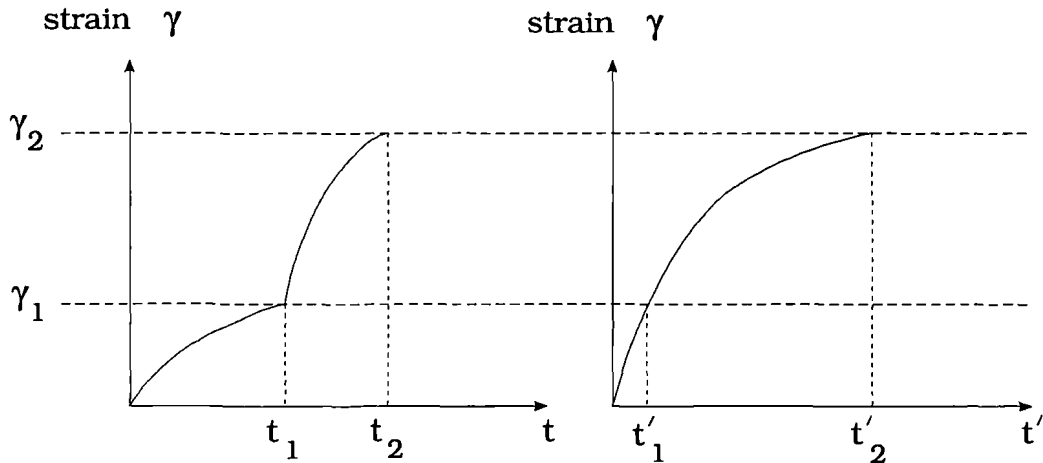
$$\gamma = \frac{\tau}{E_{p1}} \left( 1 - \exp\left(\frac{-E_{p1}t_1}{\lambda}\right) \right) + \frac{\tau}{E_{p2}} \left( 1 - \exp\left(\frac{-E_{p2}(t-t_1)}{\lambda}\right) \right) \quad \text{for } t_1 < t < t_2$$

(6.12)

Now let  $E_{p1}$  and  $E_{p2}$  be replaced by a single modulus of elasticity  $E_p$  such that  $\frac{1}{E_p} = \frac{1}{E_{p1}} + \frac{1}{E_{p2}}$  then the strain  $\gamma'$  is given by

$$\gamma' = \frac{\tau}{E_p} \left( 1 - \exp\left(\frac{-E_p t'}{\lambda}\right) \right) \quad \text{for } 0 < t' < t'_2 \quad (6.13)$$

and is depicted in figure 6.7b.



Figures 6.7a and 6.7b Strain / time diagrams for varying parallel elastic modulus and equivalent constant parallel elastic modulus respectively.

If the two representations are to be equivalent then the strain at  $t_2$  should be equal to that at  $t'_2$ , yielding

$$\gamma = \gamma_2 = \frac{\tau}{E_{p1}} \left( 1 - \exp\left(\frac{-E_{p1}t_1}{\lambda}\right) \right) + \frac{\tau}{E_{p2}} \left( 1 - \exp\left(\frac{-E_{p2}(t_2 - t_1)}{\lambda}\right) \right) \quad (6.14)$$

and

$$\gamma' = \gamma_2 = \frac{\tau}{E_p} \left( 1 - \exp\left(\frac{-E_p t'_2}{\lambda}\right) \right) \quad (6.15).$$

Substituting for  $E_p$  in (6.15) leads to

$$\gamma' = \gamma_2 = \frac{\tau}{E_{p1}} \left( 1 - \exp\left(\frac{-E_{p1}E_{p2}t'_2}{(E_{p1} + E_{p2})\lambda}\right) \right) + \frac{\tau}{E_{p2}} \left( 1 - \exp\left(\frac{-E_{p1}E_{p2}t'_2}{(E_{p1} + E_{p2})\lambda}\right) \right) \quad (6.16).$$

Comparison of each of the two terms on the right hand side of equations (6.14) and (6.16) yields,

$$t_1 = \frac{E_2 t'_2}{(E_1 + E_2)} \quad \text{and} \quad t_2 - t_1 = \frac{E_1 t'_2}{(E_1 + E_2)} \quad (6.17)$$

and therefore,

$$t_2 = \left( \frac{E_1}{(E_1 + E_2)} + \frac{E_2}{(E_1 + E_2)} \right) t'_2 = t'_2 \quad (6.18).$$

The total period of flow is therefore the same in both representations. From figures 6.7a and 6.7b it is clear that although the final deformation is equal in the two cases the transient deformation is not identical but is in fact equivalent due to the scaling of the time axis  $t'$ . For example, the equivalent time period of the deformation  $\gamma_1$  is denoted by  $t'_1$  and may be calculated by equating equations (6.12) and (6.13) at times  $t_1$  and  $t'_1$  respectively, yielding

$$t'_1 = - \frac{\lambda}{E_p} \ln \left( 1 - \frac{E_p}{E_{p1}} \left( 1 - \exp\left(\frac{-E_{p1}t_1}{\lambda}\right) \right) \right) \quad (6.19).$$

If the stress  $\tau$  is not constant but varies with  $\cos\theta$ , as during bending under gravity, then because the strains and hence the angular deformations are equivalent in the two representations so, therefore, are the stresses.

The series three-component viscoelastic combination of figure 6.4, under constant stress, may now be represented by the single valued three-component viscoelastic combination of figure 6.8.

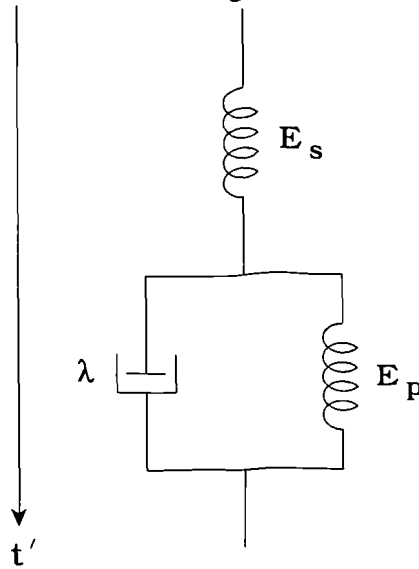


Figure 6.8 Equivalent single valued representation of a series three-component combination with time dependent parameters.

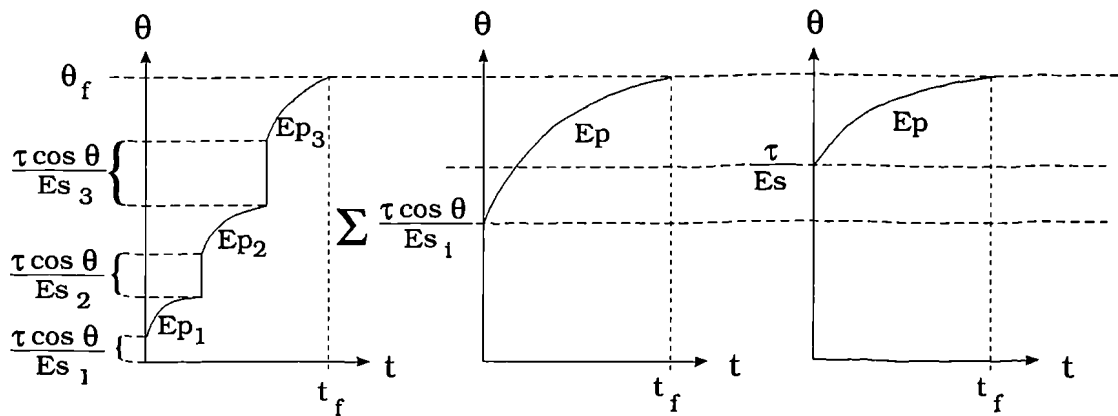
It has been shown that in the case of either varying viscous flow or varying parallel viscoelastic flow the replacement by constant parameters applies under the condition of constant stress and also under a stress which varies as  $\cos\theta$ . In the case of a series combination of varying elastic moduli, lumping of the components allows only one value of stress to be applied. Therefore, if, as during bending, the true stress varies as  $\cos\theta$  then the true

deformation is given by  $\sum_{i=1}^n \frac{\tau \cos\theta_i}{E s_i}$  compared to the lumped deformation of

$$\sum_{i=1}^n \frac{\tau}{E s_i} = \frac{\tau}{E s} \text{ where } \sum_{i=1}^n \frac{1}{E s_i} \text{ is replaced by } \frac{1}{E s}. \text{ Clearly, as } \theta_i \text{ increases } \cos\theta_i$$

decreases so that the lumped deformation is greater than the true deformation, since in the lumped deformation the stress takes its maximum value throughout such that  $\cos\theta_i = 1$ .

Consider now the series three-component viscoelastic behaviour depicted in figure 6.9a where the viscosity is constant throughout the deformation period. This behaviour may be represented equivalently by that of figure 6.9b where the strains due to the series elastic components have been lumped together and performed initially. If the series elastic moduli are to be replaced by a single modulus value  $E_s$ , as in figure 6.9c, then to ensure the same final deformation  $\theta_f$  at time  $t_f$ , the rate of deformation must be less than that of figure 6.9b, but still must be dependent upon the elastic parameter  $E_p$ , demanding therefore a decrease in the stress. It follows that, for the transient strain curve of figure 6.9c to mimic that of figure 6.9b from  $\frac{\tau}{E_s}$  to  $\theta_f$ , the stress must commence at a lower value of  $\cos\frac{\tau}{E_s}$ . It is evident that the three-component viscoelastic mechanism of figure 6.8 represents this behaviour if a constant stress of  $\tau$  is applied to the series elastic component and a deformation dependent stress of  $\tau\cos\theta$  is applied to the parallel viscoelastic component.



Figures 6.9a, 6.9b and 6.9c

The application of  $\tau$  as the initial stress has resulted in too much stress being applied to the system so that in order for figure 6.9c to yield the correct final angular deformation the excess stress must be accounted for during the transient of the parallel combination. It may be assumed that in figure 6.9b the

deformation  $\theta_f$  lies on a viscoelastic curve whose steady state solution is determined only by an elastic parameter  $E_{p_m}$ . The angular deformation  $\theta_f$  may

therefore be expressed by  $\theta_f = \frac{\tau \cos \theta_f}{E_{p_m}} \left( 1 - \exp\left(\frac{-E_{p_m} t_f}{\lambda}\right) \right)$ . If the parallel

elasticity  $E_p$  in figure 6.9c is replaced by  $E_{p_m}$  and the behaviour of the three component model of figure 6.8 modified so that the steady state strain is only dependent upon  $E_{p_m}$ , that is under constant stress  $\frac{\tau}{E_{p_m}} = \frac{\tau}{E_s} + \frac{\tau}{E_p}$ , then in

figure 6.9b  $\theta_f$  is given by

$$\theta_f = \frac{\tau \cos \theta_f}{E_{p_m}} \left( 1 - \exp\left(\frac{-E_{p_m} t_f}{\lambda}\right) \right) = \sum \frac{\tau \cos \theta}{E_{s_i}} + \frac{\tau \cos \theta_f}{E_p} \left( 1 - \exp\left(\frac{-E_p t_f}{\lambda}\right) \right).$$

It therefore follows that in figure 6.9c

$$\theta_f = \frac{\tau \cos \theta_f}{E_{p_m}} \left( 1 - \exp\left(\frac{-E_{p_m} t_f}{\lambda}\right) \right) = \frac{\tau}{E_s} + \sum \frac{\tau \cos \theta}{E_{s_i}} - \frac{\tau}{E_s} + \frac{\tau \cos \theta_f}{E_p} \left( 1 - \exp\left(\frac{-E_p t_f}{\lambda}\right) \right)$$

illustrating that the initial excess stress, and hence strain of  $\frac{\tau}{E_s}$ , is now properly accounted for.

## 6.5 Firing Shrinkage

During the firing of vitreous china sanitary ware no elongation of the ware is observed as a result of viscous flow and, therefore, a coupled model of elongation and bending is not applicable. Various changes in the dimensions of a vitreous china body occur throughout the firing process and are discussed in chapter 4. Some of the changes are temporary, occurring over certain periods of the firing cycle. A permanent decrease in the dimensions of a vitreous china body is apparent once the article has been fired and is termed the firing shrinkage. Linear firing shrinkages are commonly in the region of 10%

of the original dimensions and thus significantly affect the amount of deformation observed. Incorporation of this effect in the TLM model is, therefore, essential if an accurate prediction of the deformation is required. The variation of firing shrinkage with time is approximately linear from the onset of vitrification up to the maximum firing temperature, and is concentrated during this period of the firing schedule. Thus, the change in the dimension of the body as a result of firing shrinkage accompanies the viscous deformation.

Implementation of the linear variation of firing shrinkage over the simulation period ensures modification of the elemental lengths at each iteration according to

$$\delta l = \left( 1 - \left( \frac{\text{firing shrinkage} \times k \delta t}{\text{simulation period}} \right) \right) \delta l_0 \quad (6.20)$$

where the firing shrinkage is expressed as a percentage of the original length;

$k$  is the iteration number;

$\delta l$  is the elemental length at time  $k \delta t$ ;

$\delta l_0$  is the original, pre-fired elemental length.

Consider a simply supported beam; if the material shrinks whilst deforming viscously, as in firing, the length and thus the span of the beam will be affected. A reduction in the span accompanies the deformation as shown in figure 6.1.

Before firing:



After firing:



Figure 6.1 Reduction in span after firing.

Equation (5.31) in section 5.3.2 governing control at the ends of the beam must now be modified to incorporate the shrinkage so that the span does not remain constant but decreases linearly with time according to the amount of firing shrinkage.

## 6.6 Analytical Elastic Solutions for Test Pieces

### 6.6.1 Hoop

The geometric symmetry of the test piece depicted in figure 6.4 simplifies the problem in that it is only necessary to determine the solution for one half of the hoop.

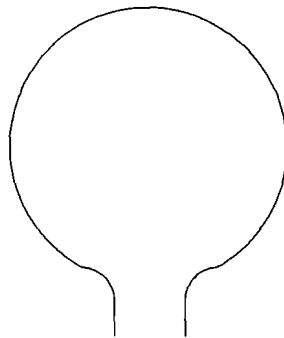


Figure 6.4 Outline of hoop for which an elastic solution is required.

Both halves of the hoop may be considered as comprising three separate sections, each having a different but constant radius of curvature. The width and thickness of the hoop are constant and are considered to be small in comparison with the circumference, so that any shearing effects are negligible.



section of the hoop. The change in angular deformation within each section is then calculated from the equilibrium condition for bending beams, namely

$$\theta = \int_0^s \frac{M}{EI} ds \quad (6.24).$$

Consider section (i) of the hoop as in figure 6.6, then the bending moment  $M_I$  at a distance  $R\phi$  along the curve is given by equation (6.25).

$$M_I = M_0 - T_0 R(1 - \cos\phi) - \int_0^\phi wR^2 (\sin\phi - \sin u) du \quad (6.25)$$

which leads to

$$M_I = M_0 - T_0 R(1 - \cos\phi) - wR^2 [\phi \sin\phi + \cos\phi - 1] \quad (6.26)$$

where  $w$  is the weight of the section per unit length.

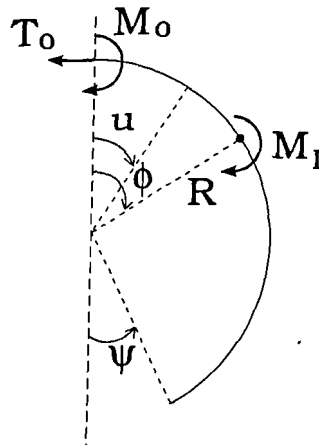


Figure 6.6 Forces and moments acting on section (i) of the hoop.

Figure 6.7 shows the forces and bending moments acting on section (ii), where the weight of section (i) is  $wR(\pi - \psi)$  and  $\alpha = \frac{\pi}{2} - \psi$ . The expression for the general bending moment  $M_{II}$  at a distance  $r\phi$  along the curve in this section is given in equation (6.27).

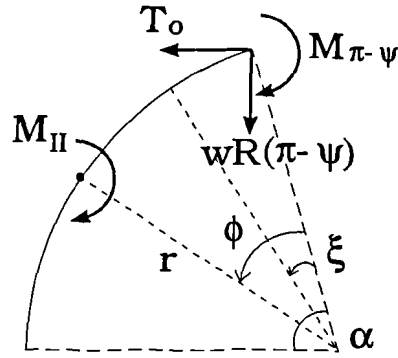


Figure 6.7 Forces and moments acting on section (ii) of the hoop.

$$\begin{aligned}
 M_{II} = M_{\pi-\psi} - T_0 r[\sin\alpha - \sin(\alpha - \phi)] - \int_0^\phi wr^2[\cos(\alpha - \phi) - \cos(\alpha - \xi)] d\xi \\
 - wRr(\pi - \psi)[\cos\alpha - \cos(\alpha - \phi)]
 \end{aligned}
 \tag{6.27}$$

where  $M_{\pi-\psi}$  is calculated from  $M_I$  at  $\phi = \psi$  in equation (6.26), that is

$$M_{\pi-\psi} = M_0 - T_0 R(1 + \cos\psi) - wR^2[(\pi - \psi)\sin\psi - \cos\psi - 1]
 \tag{6.28}.$$

Substituting (6.28) into (6.27) and evaluating the integral leads to

$$\begin{aligned}
 M_{II} = M_0 - T_0 R(1 + \cos\psi) - wR^2[(\pi - \psi)\sin\psi - \cos\psi - 1] \\
 - T_0 r[\sin\alpha - \sin(\alpha - \phi)] + wr^2[\phi\cos(\alpha - \phi) + \sin(\alpha - \phi) - \sin\alpha] \\
 + wRr(\pi - \psi)[\cos(\alpha - \phi) - \cos\alpha]
 \end{aligned}
 \tag{6.29}.$$

Figure 6.8 shows the forces and bending moments acting on section (iii) and equation (6.30) gives the general expression for the bending moment at a distance  $s$  from the top of this section.

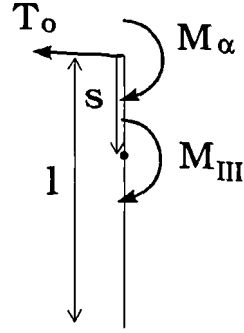


Figure 6.8 Forces and moments acting on section (iii) of the hoop.

$$M_{III} = M_{\alpha} - T_0 s \quad (6.30)$$

where  $M_{\alpha}$  is the bending moment in section (ii) at  $\phi = \alpha$ . Thus, from equation (6.29)

$$\begin{aligned} M_{\alpha} = & M_0 - T_0 R(1 + \cos\psi) - wR^2[(\pi - \psi)\sin\psi - \cos\psi - 1] - T_0 r \sin\alpha \\ & + wr^2[\alpha - \sin\alpha] + wRr(\pi - \psi)[1 - \cos\alpha] \end{aligned} \quad (6.31).$$

Substituting for  $M_{\alpha}$  in equation (6.30) yields

$$\begin{aligned} M_{III} = & M_0 - T_0 R(1 + \cos\psi) - wR^2[(\pi - \psi)\sin\psi - \cos\psi - 1] - T_0 r \sin\alpha \\ & + wr^2[\alpha - \sin\alpha] + wRr(\pi - \psi)[1 - \cos\alpha] - T_0 s \end{aligned} \quad (6.32).$$

It is now possible to determine the total energy  $U$  defined in equation (6.21). Applying the condition of zero rotation at the top of the hoop stated in equation (6.22) leads to the following expression.

$$\int_I M_I \frac{dM_I}{dM_0} ds + \int_{II} M_{II} \frac{dM_{II}}{dM_0} ds + \int_{III} M_{III} \frac{dM_{III}}{dM_0} ds = 0 \quad (6.33).$$

Equation (6.33) is further simplified to

$$\int_I M_I ds + \int_{II} M_{II} ds + \int_{III} M_{III} ds = 0 \quad (6.34)$$

since, by inspection,

$$\frac{dM_I}{dM_o} = \frac{dM_{II}}{dM_o} = \frac{dM_{III}}{dM_o} = 1 \quad (6.35).$$

The limits of the integrals are determined from figures 6.6, 6.7 and 6.8 so that equation (6.34) may be expressed as

$$\int_0^{\pi-\psi} M_I R \, d\phi + \int_0^{\alpha} M_{II} r \, d\phi + \int_0^1 M_{III} \, ds = 0 \quad (6.36).$$

Evaluation of equation (6.36) yields an expression of the form

$$M_o A_1 - T_o B_1 = C_1 \quad (6.37)$$

where  $A_1$ ,  $B_1$  and  $C_1$  are constants determined by integration.

Applying now the condition of no horizontal displacement at the top of the hoop (6.23) to the total energy expression (6.21) yields

$$\int_I M_I \frac{dM_I}{dT_o} \, ds + \int_{II} M_{II} \frac{dM_{II}}{dT_o} \, ds + \int_{III} M_{III} \frac{dM_{III}}{dT_o} \, ds = 0 \quad (6.38)$$

where

$$\frac{dM_I}{dT_o} = -R(1 - \cos\phi)$$

$$\frac{dM_{II}}{dT_o} = -R(1 + \cos\psi) - r[\sin\alpha - \sin(\alpha - \phi)]$$

$$\frac{dM_{III}}{dT_o} = -r\sin\alpha - s - R[1 + \cos\psi] \quad (6.39).$$

Applying the limits of integration as in equation (6.36) and thus evaluating equation (6.38) yields an expression of the form

$$M_o A_2 + T_o B_2 = C_2 \quad (6.40)$$

where  $A_2$ ,  $B_2$  and  $C_2$  are constants determined by integration.

The values of  $M_o$  and  $T_o$  may now be determined from the simultaneous equations (6.37) and (6.40). Substitution of  $M_o$  and  $T_o$  in equations (6.26), (6.29) and (6.32) yields solutions for the bending moments throughout the

hoop so that the angular deformation may be calculated in each section according to equation (6.24), to give

$$\theta_I = \int_0^\phi \frac{M_I R}{EI} d\phi = \frac{R}{EI} [M_o \phi - T_o R(\phi - \sin \phi) - wR^2 [-\phi \cos \phi + 2 \sin \phi - \phi]] \quad (6.41)$$

$$\begin{aligned} \theta_{II} &= \int_0^\phi \frac{M_{II} r}{EI} d\phi \\ &= \frac{r}{EI} [M_o \phi - T_o R \phi [1 + \cos \psi] - wR^2 \phi [(\pi - \psi) \sin \psi - \cos \psi - 1] \\ &\quad - T_o r [\phi \cos \psi - \cos(\frac{\pi}{2} - \psi - \phi) + \sin \psi] \\ &\quad + w r^2 [-\phi \sin(\frac{\pi}{2} - \psi - \phi) + 2 + \phi \sin \phi - 2 \sin \psi] \\ &\quad + w R r (\pi - \psi) [-\sin(\frac{\pi}{2} - \psi - \phi) - \phi \sin \psi + \cos \psi]] \end{aligned} \quad (6.42)$$

$$\begin{aligned} \theta_{III} &= \int_0^s \frac{M_{III}}{EI} ds \\ &= \frac{s}{EI} [M_o - T_o R(1 + \cos \psi) - wR^2 [(\pi - \psi) \sin \psi - \cos \psi - 1] - T_o r \cos \psi \\ &\quad + w r^2 [\frac{\pi}{2} - \psi - \cos \psi] + w R r (\pi - \psi) [1 - \sin \psi] - \frac{T_o s}{2}] \end{aligned} \quad (6.43).$$

The angular inclination with respect to the horizontal in section (i) of the hoop is given by  $\theta = \pi - \phi$ , and in section (ii) by  $\theta = \psi + \phi$  so that equations (6.41) and (6.42) may be expressed as

$$\theta_I = \frac{R}{EI} [M_o (\pi - \theta) - T_o R [(\pi - \theta) - \sin \theta] - wR^2 [(\pi - \theta) \cos \theta + 2 \sin \theta - \pi + \theta]] \quad (6.44)$$

$$\begin{aligned}
\theta_{II} = & \frac{r}{EI} [M_o(\theta - \psi) - T_o R(\theta - \pi)[1 + \cos \psi] \\
& - wR^2(\theta - \psi)[(\pi - \psi) \sin \psi - \cos \psi - 1] - T_o r[(\theta - \psi) \cos \psi - \sin \theta + \sin \psi] \\
& + wr^2[(\psi - \theta) \cos \theta + 2 + (\theta - \psi) \sin(\theta - \psi) - 2 \sin \psi] + wRr(\pi - \psi)[- \cos \theta - (\theta - \psi) \sin \psi + \cos \psi]
\end{aligned}
\tag{6.45}$$

and are now compatible with the rotational TLM model formulation discussed in chapter 5.

The expressions for  $\theta_I$ ,  $\theta_{II}$  and  $\theta_{III}$  for the left half of the hoop are obtained by inverting the integrals in each case and replacing  $\theta$  by  $2\pi - \theta$  in equations (6.44) and (6.45).

### 6.6.2 Mushroom Shell

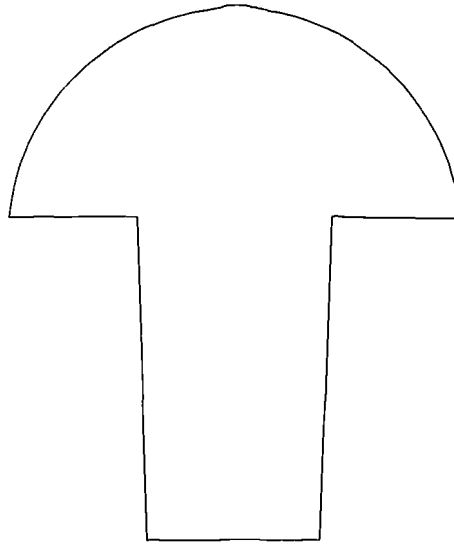


Figure 6.9 Outline of three dimensional mushroom.

The analytical solution for the elastic deformation of the mushroom shell, illustrated in figure 6.9, considers only the deformation of the plate connecting the stalk and the dome. Due to the high elasticity of the material deformation of the stalk and dome is considered negligible, significant deformation occurring only in the plate.

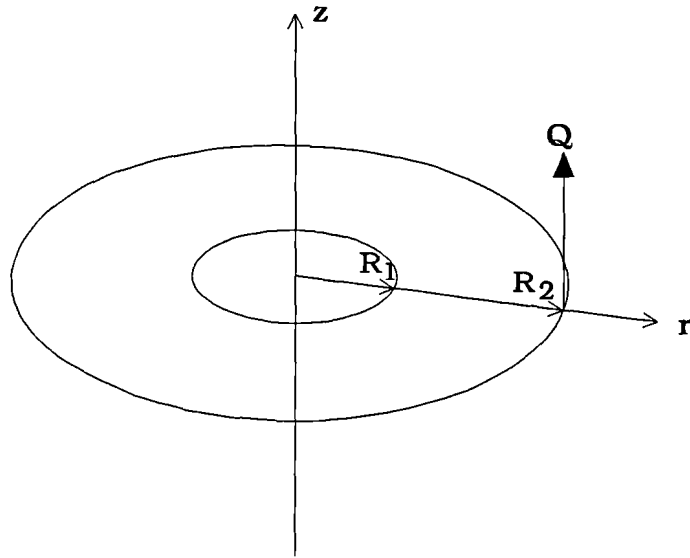


Figure 6.10 Circular 2-d plate with hole of radius  $R_1$  at centre.

The plate is considered to be clamped at the inner radius, so that both the vertical displacement and the angular deformation are zero at  $R_1$ . At the outer edge of the plate the thickness increases so as to reinforce the structure where the plate joins the dome. This reinforcement is modelled by considering the plate to have a weightless, rigid ring fixed to the outer rim which forces the gradient to be zero. The weight of the dome acting along this circumference is also taken into consideration.

The displacement of the plate in the  $z$  direction is denoted by  $w$  and in chapter 2 was shown to be related to the vertical force per unit length  $Q$  by the following equation

$$\frac{d}{dr} \left( \frac{1}{r} \frac{d}{dr} \left( r \frac{dw}{dr} \right) \right) = -\frac{Q}{D} \quad (2.100).$$

The weight per unit area of the plate is given by  $q$ , so that  $Q2\pi r = \int_0^r q2\pi r \, dr$

which, upon substitution for  $Q$  in (2.100), leads to

$$\frac{1}{r} \frac{d}{dr} \left( r \frac{d}{dr} \left( \frac{1}{r} \frac{d}{dr} \left( r \frac{dw}{dr} \right) \right) \right) = -\frac{q}{D} \quad (6.46).$$

The general solution of (6.46) is given by

$$w = -\frac{qr^4}{64D} + a_1r^2 + a_2 + a_3r^2 \ln r + a_4 \ln r \quad (6.47)$$

where  $a_1, a_2, a_3$  and  $a_4$  are constants of integration to be determined.

The dome of the mushroom is of radius  $R$  and represents the cap of a sphere of radius  $R$  as illustrated in figure 6.11.

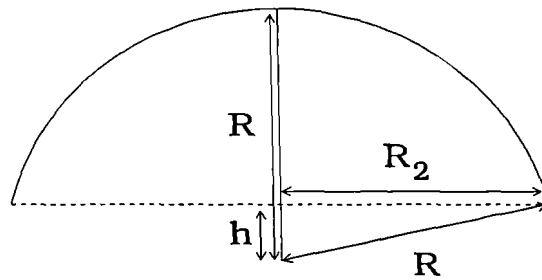


Figure 6.11 Dome of mushroom represented by a spherical cap.

The surface area of the cap can be calculated as a fraction of that of a hemisphere and is, therefore, given by

$$2\pi R^2 \frac{(R-h)}{R} = 2\pi R^2 \left( 1 - \frac{\sqrt{(R^2 - R_2^2)}}{R} \right) \quad (6.48).$$

The force per unit length  $Q$  in figure 6.10 is equal to the weight of the dome per unit length. The expression for the surface area of the dome in (6.48) therefore leads to

$$Q = \frac{\text{weight of dome}}{2\pi R_2} = \frac{q 2\pi R^2 \left( 1 - \frac{\sqrt{(R^2 - R_2^2)}}{R} \right)}{2\pi R_2} \quad (6.49)$$

and substitution for  $Q$  in equation (2.100) now yields

$$-D \frac{d}{dr} \left( \frac{1}{r} \frac{d}{dr} \left( r \frac{dw}{dr} \right) \right) = - \frac{qR^2 \left( 1 - \frac{\sqrt{(R^2 - R_2^2)}}{R} \right)}{R_2} \quad (6.50).$$

Substituting for  $w$  from (6.47) at  $r=R_2$  into (6.50) leads to

$$\frac{qR_2}{2} - \frac{4Da_3}{R_2} = - \frac{qR^2 \left( 1 - \frac{\sqrt{(R^2 - R_2^2)}}{R} \right)}{R_2} \quad (6.51).$$

Also, at the outer edge of the plate the gradient is zero so that  $\frac{dw}{dr}=0$  at  $r=R_2$

which, from equation (6.47), yields

$$2a_1R_2 + (2R_2 \ln R_2 + R_2)a_3 + \frac{a_4}{R_2} - \frac{qR_2^3}{16D} = 0 \quad (6.52).$$

The conditions at the inner radius  $r=R_1$  are  $w=0$  and  $\frac{dw}{dr}=0$  which, from

equation (6.47), give

$$a_1R_1^2 + a_2 + a_3R_1^2 \ln R_1 + a_4 \ln R_1 - \frac{qR_1^4}{64D} = 0 \quad (6.53)$$

and

$$2a_1R_1 + (2R_1 \ln R_1 + R_1)a_3 + \frac{a_4}{R_1} - \frac{qR_2^3}{16D} = 0 \quad (6.54).$$

Expressions may now be obtained for each of the constants of integration.

Rearrangement of (6.51) gives

$$a_3 = \frac{R_2}{4D} \left( \frac{qR_2}{2} + \frac{qR}{R_2} \left( 1 - \sqrt{R^2 - R_2^2} \right) \right) \quad (6.55).$$

Solving the remaining simultaneous equations yields

$$a_4 = \frac{1}{\left( \frac{R_2}{R_1^2} - \frac{1}{R_2} \right)} \left( \frac{qR_2}{16D} (R_1^2 - R_2^2) + 2R_2 (\ln R_2 - \ln R_1) a_3 \right) \quad (6.56)$$

$$a_1 = \left( \frac{qR_1^3}{16D} - (2R_1 \ln R_1 + R_1)a_3 - \frac{a_4}{R_1} \right) \frac{1}{2R_1} \quad (6.57)$$

$$a_2 = \frac{qR_1^4}{64D} - a_1 R_1^2 - a_3 R_1^2 \ln R_1 - a_4 \ln R_1 \quad (6.58).$$

The vertical deflection of the plate  $w$  may now be determined from equation (6.47). The angular deformation of the plate,  $\theta$ , is determined by differentiation of (6.47) with respect to  $r$ , since  $\tan \theta = \frac{dw}{dr}$ , yielding

$$\theta = \tan^{-1} \left( -\frac{qr^3}{16D} + 2a_1 r + a_3(2r \ln r + r) + \frac{a_4}{r} \right) \quad (6.59).$$

## 6.7 Comparison of TLM with Experimental Results

### 6.7.1 Details of testpieces

Results have been obtained for seven vitreous china ware testpieces:

- (i) three bars, supported as cantilevers;
- (ii) three hoops;
- (iii) a three-dimensional mushroom shell.

All of the testpieces were slipcast into plaster of paris moulds. The bars and hoops were manufactured from the same slip, and therefore taken to be of the same density, viscosity and elasticity. A slip of different composition was used in the manufacture of the mushroom which produced less deformation in identical bars made from the first slip. The values of viscosity and elasticity for the mushroom, therefore, were assumed to be higher. The mass of each testpiece is assumed constant throughout the deformation period so that the bulk density increases as the volume of the pieces decreases due to firing shrinkage. The time variation of the bulk density does not result from the

gravitational deformation of the material and therefore the body may be assumed incompressible throughout the liquid phase.

The bodies are assumed to deform significantly during firing throughout the viscosity range of approximately  $10^{11} \text{ gcm}^{-1}\text{s}^{-1}$  to  $10^5 \text{ gcm}^{-1}\text{s}^{-1}$  and over a time period of approximately four hours. The range of Young's Modulus in series is assumed to be approximately  $10^{12} \text{ gcm}^{-1}\text{s}^{-2}$  to  $10^6 \text{ gcm}^{-1}\text{s}^{-2}$ . The range of Young's Modulus in parallel, implemented as  $E_{p_m}$  described in section 6.4, is assumed to be the same order of magnitude as that of the viscosity.

The dimensions of each of the three bars are given in table 6.1 and were calculated from the mould dimensions after taking account of the 4% linear drying shrinkage. The length of each bar is the deformable length, that is the length protruding from the clamped support.

	bar 1	bar 2	bar 3
length in cm	10.40	10.40	20.24
width in cm	1.63	2.69	1.63
height in cm	0.91	1.59	0.91

Table 6.1 Pre-fired dimensions of bars.

The elastic solutions for the short bars, bar 1 and bar 2, may be obtained either from the small strain analytical theory or from the TLM elastic model as the values of the Young's Moduli are high so that both approaches yield the same small strain result. The elastic solutions for the long bar, however, demand implementation of the TLM elastic model as the deformation can no longer be considered as small strain.

A schematic of the hoops is depicted in figure 6.12 with the corresponding dimension values being given in table 6.2. As for the bars the hoop dimensions were calculated from the mould geometries accounting for the drying shrinkage. In each case the cross-sectional hoop thickness is 0.92cm and the width is 1.74cm.

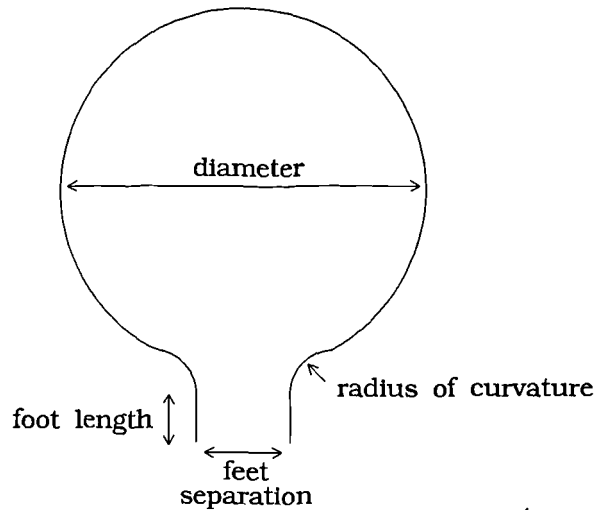


Figure 6.12 Schematic of hoop.

	hoop 1	hoop 2	hoop 3
foot length in cm	1.63	2.17	2.39
radius of curvature in cm <sup>-1</sup>	1.41	1.63	1.82
diameter in cm	12.17	13.70	15.16
feet separation in cm	3.48	3.80	4.25

Table 6.2 Pre-fired dimensions of hoops.

In the TLM routine for the hoop the viscous loading in the incident pulses takes the following form,

$$V^i = V^i + \frac{1}{2} \left( \frac{n}{2} - i \right) g \delta l \cos \theta_o(i) \delta t \quad (6.60)$$

since each foot supports half the weight of the hoop, as in the case of a simply supported beam detailed in chapter 5, and where  $\theta_0(i)$  denotes the initial angular inclination of each element.

Figure 6.13 depicts the central cross-section of the three dimensional mushroom shell, the dimensions of which being detailed in table 6.3.

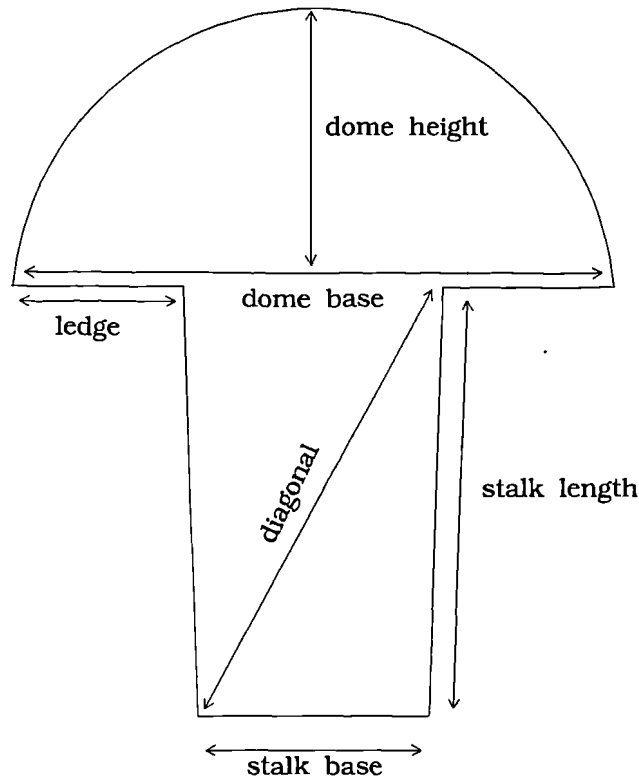


Figure 6.13 Central cross-section of mushroom shell.

stalk length in cm	18.0
diagonal in cm	20.5
stalk base in cm	9.0
dome base in cm	28.0
ledge in cm	8.0
dome height in cm	10.0
average shell thickness in cm	0.7

Table 6.3 Pre-fired dimensions of mushroom.

The elastic analytical solution for the mushroom assumed an average shell thickness of 0.7cm. In the TLM routine, however, the geometry of the mushroom could be incorporated more precisely, reflecting the variation in thickness of the dome and ledges of the mushroom shell as depicted in figure 6.14.

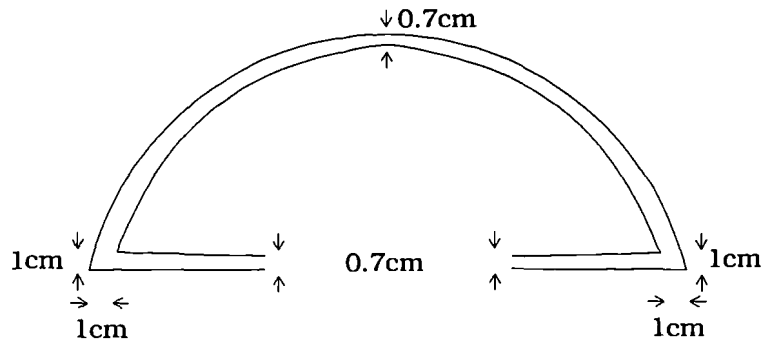


Figure 6.14 Mushroom dome and ledges in detail.

The viscous loading in the pulses of the mushroom models the total weight of the shell divided by the number of segments in the model, so that the weight is distributed evenly around the base of the stalk.

### 6.7.2 Results

Details of the parameter values used in the simulations are given at the end of this section together with the computer run times.

Figures 6.15, 6.16 and 6.17 compare the experimental deformations of the cantilevers with the simulated results from a three-component viscoelastic TLM model. The maximum angular deformations of the bars are compared in table 6.4.



Figure 6.15 Comparison of experimental results (dark outline) and three-component viscoelastic TLM model results for bar 1.

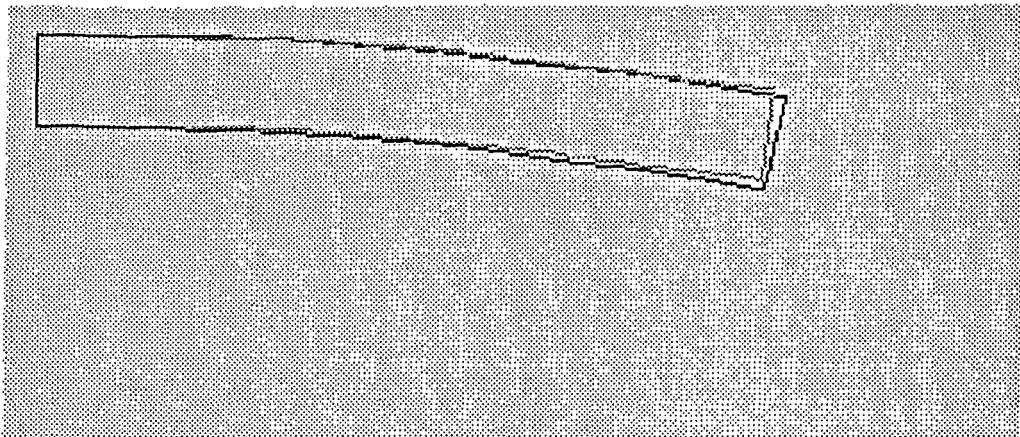


Figure 6.16 Comparison of experimental results (dark outline) and three-component viscoelastic TLM model results for bar 2.

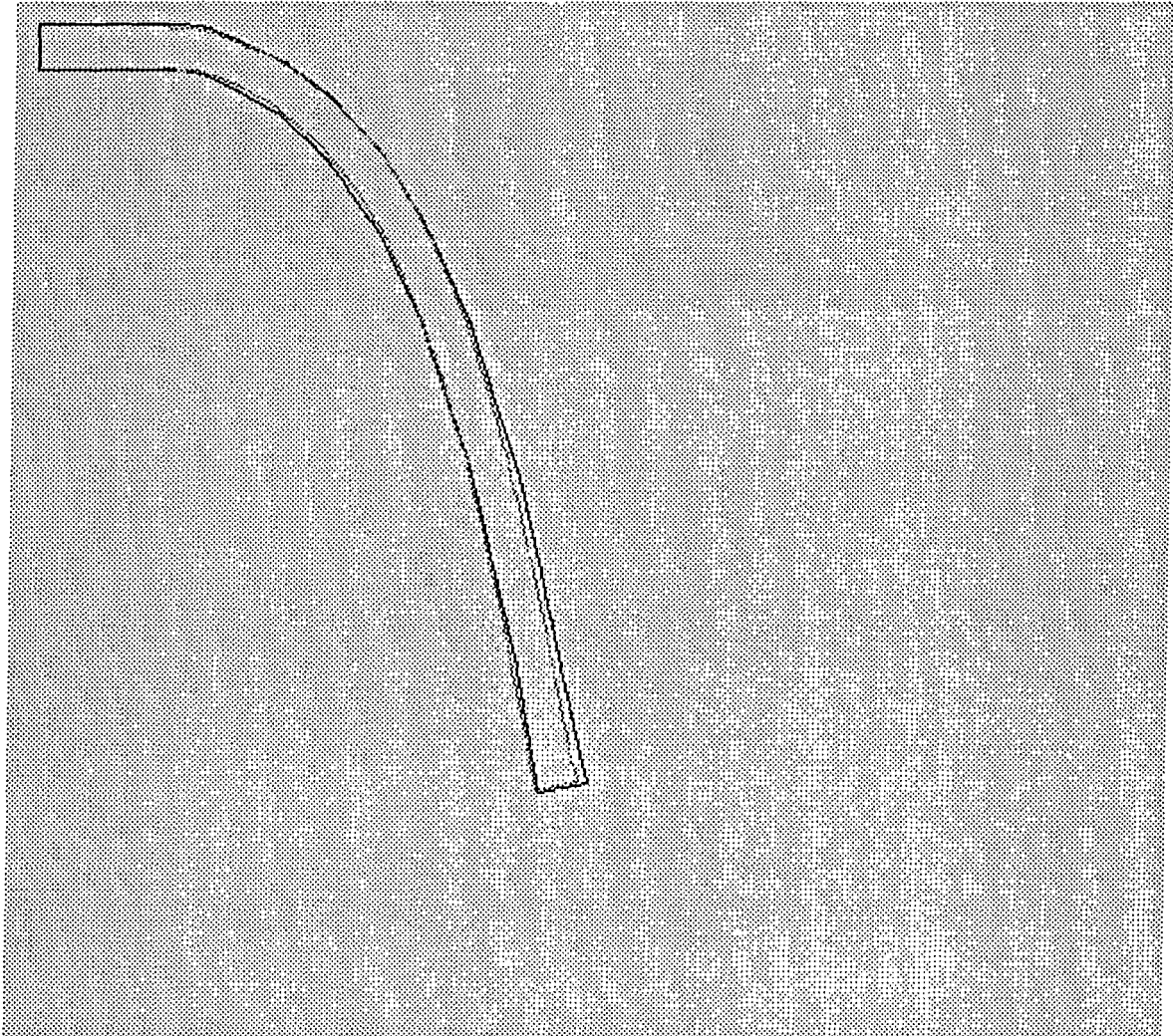


Figure 6.17 Comparison of experimental results (dark outline) and three-component viscoelastic TLM model results for bar 3.

	average measured angular deformation at end of beam in degrees	predicted angular deformation at end of beam in degrees
bar 1	21.33	21.83
bar 2	7.75	7.06
bar 3	77.75	77.70

Table 6.4 Comparison of the experimental cantilever deformations with predicted deformations using a three-component viscoelastic TLM model.

The experimental results were determined from the average deformation of three bars in each case. Each ceramic beam was placed on graph paper so that the outline of the piece could be plotted and the average angular deflection at the end of the beam could then be measured. The variation of these results was no greater than 5%. The percentage errors in the results of table 6.4 are 2.3%, 8.9% and 0.1% respectively. The cross-sectional area of bar 2 is greater than that of the other two bars so that the weight is also greater. Tighter clamping is therefore required for bar 2 which, if insufficient, will introduce error in the experimental deformation. The larger error associated with bar 2 is, therefore, possibly due to insufficient supporting conditions.

Figure 6.18 compares the experimental deformation of hoop 2 with the simulated results from a three-component viscoelastic TLM model. The maximum vertical and horizontal deformations of each of the three hoops are compared in table 6.5. The experimental values given are the average values of three hoops per geometry, the variation in each case being less than 6% .

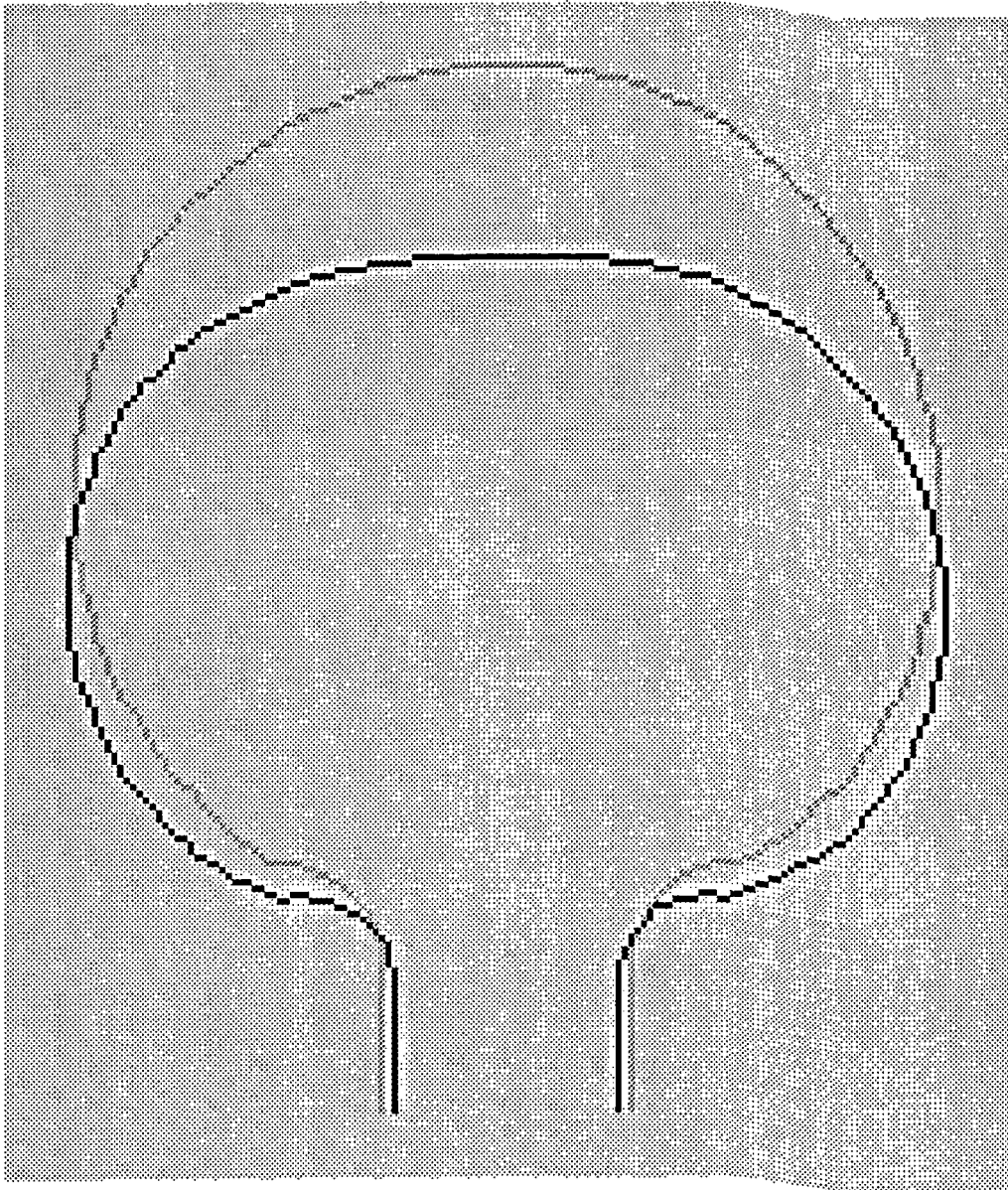


Figure 6.18 Simulated 3-component viscoelastic deformation (dark outline) overlying original pre-fired hoop geometry.

	original diameter cm	measured change in height cm	predicted change in height cm	measured maximum horizontal diameter cm	predicted maximum horizontal diameter cm
hoop 1	12.17	1.84	1.86	11.55	11.78
hoop 2	13.70	2.60	2.53	13.65	13.44
hoop 3	15.16	3.47	3.37	15.70	15.16

Table 6.5 Comparison of the average experimental hoop deformations with predicted deformations using a three-component viscoelastic TLM model.

The percentage errors in the results of table 6.5 are less than 3.5% for each of the hoops. In practice a horizontal bar connects the feet so that the hoop is a stable, upright structure throughout the firing process. However, the bar is not modelled either elastically or viscoelastically as its presence is assumed to have a negligible effect upon the main deformation of the hoop. The model assumes that the base of the feet do not bend but ensures that the feet separation experiences the correct amount of firing shrinkage by incorporation of the PID control theory of chapter 5. The boundary conditions applied in the model lead to the very slight buckling inwards of the legs of the hoop, whereas in reality the legs bend outwards due to the slight raising of the bar in between the feet.

Figure 6.19 compares the experimental deformation of a segment of the mushroom shell with the simulated results from a three-component viscoelastic TLM model. Table 6.6 compares the average experimental results of three mushroom shells with simulated results.

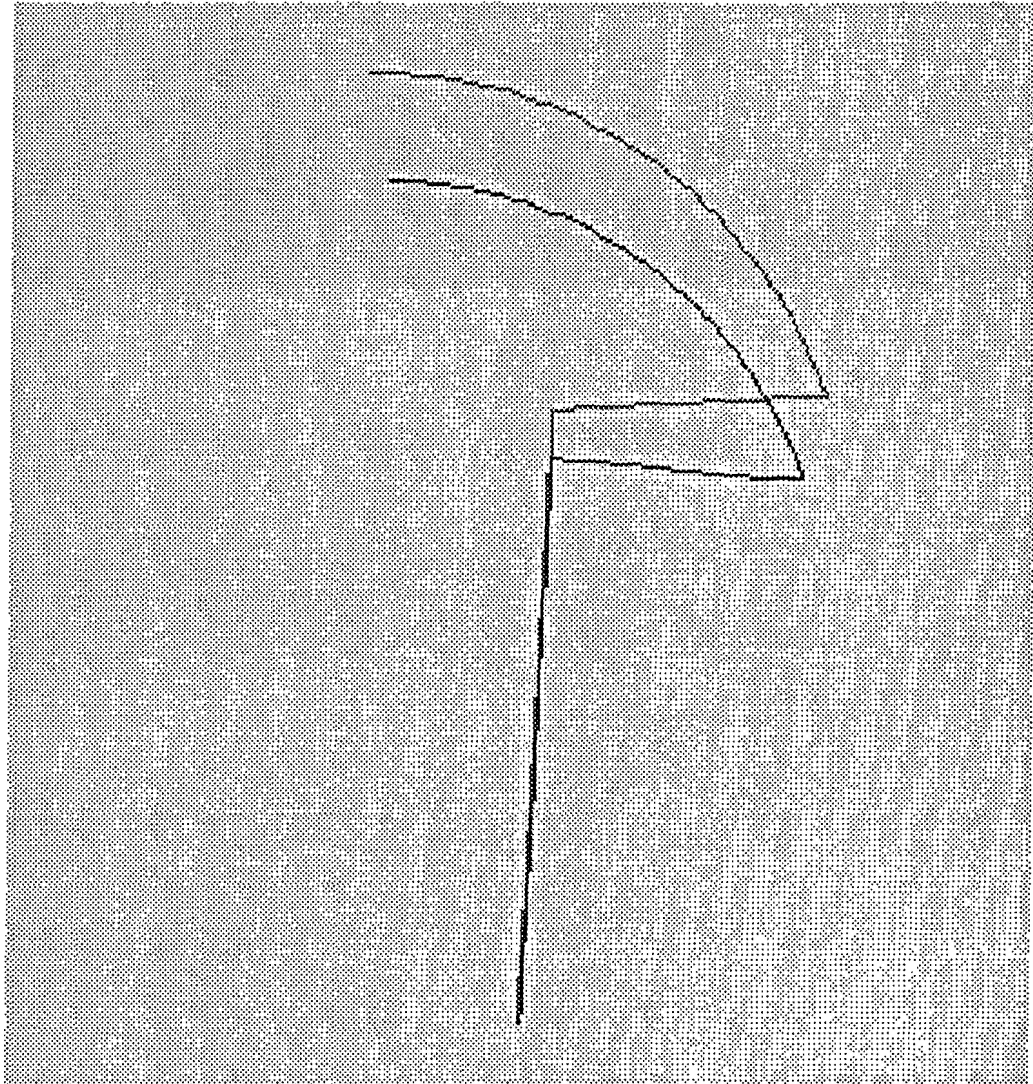


Figure 6.19 Simulated 3-component viscoelastic deformation (dark outline) overlying original pre-fired mushroom shell segment.

	measured results	predicted results
change in maximum vertical height	3.68 cm	3.34 cm
maximum angular deformation near centre of ledge	9° - 20°	8.25°
vertical height at outer ledge circumference	15.60 cm	15.86 cm

Table 6.6 Comparison of the average experimental deformation of the mushroom with the predicted deformation using a three-component viscoelastic TLM model.

The variation in the average vertical deflections of the experimental results was less than 3%, the angular deflections in the ledge however displayed a greater variation of 38%. Most errors in table 6.6 are less than 10%, although the undulation in the mushroom ledge increases the error to slightly less than 60%. The thickness of the mushroom ledges, although modelled as a constant, does vary slightly around the circumference of each mushroom. A variation in the thickness of the shell can significantly alter the amount of deformation as angular deformation is inversely proportional to the square value of the thickness. The mass of each of the fired mushrooms is also not constant, suggesting either a discrepancy in density and/or shell volume. The variation of angular deformation in the ledge could also possibly be due to an uneven temperature distribution which is not accounted for in the model.

The analytical elastic solutions used in the model only assume deformation in the ledge of the mushroom so that errors may have been introduced by the simplicity of the model. The base of the mushroom which constitutes a circular plate is not modelled either elastically or viscoelastically as it is assumed to have a negligible effect upon the deformation of the structure. As for the hoops, the model ensures that the base of the stalk

experiences the correct amount of firing shrinkage by incorporation of the PID control theory of chapter 5.

All models were run with converged values of elemental length and timestep. For the bars and hoops a viscosity of  $10^5 \text{gcm}^{-1}\text{s}^{-1}$  demanded a timestep of  $10^{-7}\text{s}$  for convergence. The model of the mushroom shell was executed with a higher viscosity of  $2 \times 10^5 \text{gcm}^{-1}\text{s}^{-1}$ , demanding a converged timestep of  $5 \times 10^{-8}\text{s}$ . Each model was run for a simulated time period of 0.017s being equivalent to approximately 4 hours over the true viscosity range. The density parameter of each body was  $2.4 \text{gcm}^{-3}$  and the linear firing shrinkage was 8%. The series elasticity parameter value used for the bars and hoops was  $3600 \times 10^4 \text{gcm}^{-1}\text{s}^{-2}$  and the parallel elasticity value  $E_{p_m}$  was  $900 \times 10^4 \text{gcm}^{-1}\text{s}^{-2}$ . The viscosity and Young's Moduli of the mushroom were determined by comparing the experimental deformation of a cantilever, having the same dimensions of bar 1, with simulated results and increasing the parameter values until good agreement was observed. The series elasticity parameter value used was  $4500 \times 10^4 \text{gcm}^{-1}\text{s}^{-2}$  and the parallel elasticity value  $E_{p_m}$  was  $900 \times 10^4 \text{gcm}^{-1}\text{s}^{-2}$ .

For each of the short bars 41 nodes were used in the model and for the long bar 81 nodes were required for convergence. Run times of these simulations were approximately 20 minutes on 486 IBM compatible PC. The run times of the hoops were approximately 40 minutes due to the increase in the number of nodes required. The mushroom shell required 174 nodes with an average nodal separation of 0.25cm along the length of each segment and was run with 12 segments. Because of the smaller timestep and the two dimensional structure of the TLM routine the run time of this model was greatly increased to 4 days and necessitated the use of a Sun Sparc 10 work station. However, due to the symmetry of the structure the mushroom could be modelled using a one dimensional routine which would reduce the run time to a couple of hours on a 486 PC.

## 6.8 References

- [1] I C McDowall and W Vose, "The Determination of the Pyroplastic Deformation in the Firing of Ceramic Bodies", Transactions of the British Ceramic Society, vol 11, pp 506-516, 1951.
- [2] D S Adcock, J E Drummond and I C McDowall, "Pyroplastic Index and Firing Deformation of Ceramic Bodies", Journal of the American Ceramic Society, vol 42, pp 525-532, 1959.
- [3] A McNabb and M E Duncan, "Firing Deformation of Ceramic Bodies", Ceramic Bulletin, vol 46, no 5, pp 515-520, 1967.
- [4] J M Gaillard, C Gault, J C Glandus and P Petrault, "Prediction of Deformation in Plates using Finite Element Analysis and the Measurement of Physical Parameters under Process Conditions", Ceramurgia, Materials Processes, vol XXI, no 6, pp 229-232, 1991.
- [5] U U Chi and R E Sosman, "Deformation of a Kaolinite Body Under Stress at High Temperatures", Ceramic Bulletin, vol 40, no 7, pp 426-431, 1961.
- [6] K Jakus and S M Wiederhorn, "Creep Deformation of Ceramics in Four-Point Bending", Journal of the American Ceramic Society, vol 71 [10], pp 832-836, 1988.

- [7] G C Padgett, J A Cox and J F Clements, "Stress/Strain Behaviour of Refractory Materials at High Temperatures", Research Paper 608, British Ceramic Research Association, also printed in January 1969 Transactions.
- [8] A R Rosenfield, W H Duckworth and D K Shetty, "Damage Analysis of Creep in Bending", Journal of the American Ceramic Society, vol 68 [9], pp 483-485, 1985.
- [9] M G McLaren, C-I Park and G W Phelps, "High Temperature Torsion Testing of Sanitary Whiteware Bodies", Ceramica, vol 24 [102], pp 245-252, 1978.
- [10] J J Mills, "The Viscoelastic Response of Glass During Forming", Glass Technology, vol 14, no 4, pp 101-105, 1973.
- [11] C-H Hsueh, "Mathematical Model of Viscosity Measurements for Viscoelastic Solids", Journal of the American Ceramic Society, vol 69 [3], pp C48-C49, 1986.
- [12] J W Weinstein, G W Phelps and M G McLaren, "Raw Material Characterisation and its Relation to Pyroplastic Behaviour in Porcelain Bodies", Ceramica, vol 28 [153], pp 357-363, 1982.
- [13] R K Wood, "Sanitary Ware - The Effect of Fast-Fire Kiln Cooling on Ware Properties", Ceramic Bulletin, vol 58, no 12, pp 1169-1171, 1979.

- [14] G Urbain, F Cambier, M Deletter and M R Anseau, "Viscosity of Silicate Melts", Transactions of the Journal of the British Ceramic Society, vol 80, pp 139-141, 1981.
- [15] N M Ghoneim, E H Sallam and D M Ebrahim, "Role of Accessory Minerals on the Vitrification of Whiteware Compositions", Ceramics International, vol 16, pp 19-24, 1990.
- [16] S Timoshenko, Strength of Materials, Part I, Elementary Theory and Problems, pp 378-381, third edition, Robert E. Krieger Publishing Company, New York, 1976.

## **CHAPTER 7**

### **DISCUSSION**

This final chapter reviews the thesis and emphasises the more significant aspects of the research. Areas for future work are also highlighted.

## 7.1 Summary of Thesis

The transmission line modelling (TLM) technique has been applied to two types of deformation, these being elongation and bending, each under the effect of gravity. Models of viscous deformation have been formulated in each case. More complex models of viscoelastic behaviour have been developed and applied to bending under gravity. The behaviours modelled are:

- a) series viscoelastic behaviour;
- b) parallel viscoelastic behaviour;
- c) three-component viscoelastic behaviour.

An elastic TLM routine which provides steady state solutions for beams bending under their own weight has also been developed. The application of the TLM modelling technique to each type of behaviour above is presented for the first time in this thesis.

Although the elastic model represents the behaviour of a damped wave it does not, in its present form, match the transient behaviour of a parallel viscoelastic mechanism as represented by the viscous based parallel viscoelastic model. From chapter 5, the damped elastic equation used to obtain elastic steady state solutions is given by

$$\frac{\partial^2 I_z \theta}{\partial x^2} + \frac{\rho b h (L - x) g \cos \theta}{E} = \frac{\rho}{E} \frac{\partial^2 I_z \theta}{\partial t^2} + \frac{\lambda}{E b h} \frac{\partial I_z \theta}{\partial t} \quad (5.69).$$

However, for the transient behaviour to match that of the viscous-based parallel viscoelastic model, the term containing the first order time derivative must take the following form,

$$\frac{\lambda}{E} \frac{\partial^2}{\partial x^2} \left( \frac{\partial I_z \theta}{\partial t} \right) \quad (7.1)$$

since the viscous-based equation is given by

$$\frac{\partial^2 I_z \omega}{\partial x^2} + \frac{\rho (n-i) \delta l b h g \cos \theta}{\lambda} \left( 1 - \frac{\theta(i)}{\theta_{\text{elastic}}(i)} \right) = \frac{\rho}{\lambda} \frac{\partial I_z \omega}{\partial t} \quad (5.57)$$

where  $\omega = \frac{\partial \theta}{\partial t}$ .

In equation (5.57) the gravitational term contains the required steady state elastic solution and therefore represents the two terms on the left hand side of equation (5.69), once this equation has been multiplied through by  $E/\lambda$ . Clearly, the angular acceleration term appears identically in both equations so that only with the modified time derivative term of (7.1) does the damped wave representation model the parallel viscoelastic mechanism. Unfortunately, a wave equation comprising the term of (7.1) is not in the required form for solution by the TLM technique so that the viscous-based approach of equation (5.57) has been adopted. Upon comparison of the time derivative of equation (5.69) and that of (7.1) it is evident that, although dimensionally identical, the first term represents damping associated with the total velocity and the second term represents damping associated with relative velocities of the body. This implies that the term of equation (5.69) models an external damping effect, such as air resistance or the damping imposed by the viscosity of an external medium, and the term of (7.1) models an internal damping effect.

## 7.2 Important Features of the Deformation Models

The viscous model of an elongating column of fluid yields solutions throughout the entire viscosity range which reveal the inherent ability of the model to reflect the associated change in physical behaviour from non-Newtonian to Newtonian. At high viscosities the model reveals a proportionality between the rate of elongation and the weight distribution in the column, whereas at low viscosities this proportionality is shown to break down. The bending model is dependent upon the shearing forces for the

loading of the network and therefore is dependent upon resultant stresses from the elongational model to represent accurately the behaviour throughout the viscosity range. The bending model, therefore, does not display the same inherent ability to distinguish correctly between highly viscous and low viscous behaviour, and is instead dependent upon the loading for this information. The necessity for coupling of the two models at low viscosity is clearly apparent, whereas at high viscosities the need for coupling is eliminated due to the viscous body stresses being directly proportional to the weight distribution.

Results from the viscous bending model illustrate the viscous/elastic analogy under constant shearing stress, which has been used by previous investigators of ceramic deformation as mentioned earlier in chapter 6. It is now apparent why results using this analogy did not yield good agreement in industrial practice as the loading neglects the angular dependency given by  $\cos\theta$  and is therefore incorrect for viscous deformation under gravity, particularly when the deformation cannot be considered to be small strain.

An unfortunate aspect of the viscous model is the relationship between rate of flow and the modelling timestep, such that highly viscous fluids, being slow moving, necessitate very small timesteps compared to those associated with fast moving fluids. However, this modelling disadvantage can be taken in hand and minimised to an extent by effectively scaling the flow, which is achieved by choosing a lower viscosity, but not so low that the proportionality of stress and strain rate is no longer satisfied, accompanied by an associated smaller time period.

In the application of the deformation models to ceramics the parameters were lumped together rather than modelled as varying throughout the transient. In this case, although the range of the parameters could be ascertained, the precise variation of the parameters was not known. Reducing the total number of parameters to the minimum possible, that is one per component, was

therefore deemed the most efficient choice and retained simplicity within the model. Clearly, in situations where the precise variation of the parameters of the transient is known the true values may be modelled directly for the associated flow periods. Time dependency of network parameters has been addressed in chapter 3 and does not in itself pose a difficulty to the TLM technique. The variation of series elastic component parameters, however, may prove to be cumbersome due to the need of obtaining each solution for a beam having initial curvature. As with any numerical model a balance must be found between computing efficiency and true parameter representation, so that in the case of continuously time varying parameters it may prove more acceptable to simplify the model and use model parameter values which, like the true parameter values and as shown for the ceramic testpieces, are consistent over a range of geometries for a given material composition. Clearly, however, modifications to the firing schedule, such as a sudden rise in temperature at a particular point during the transient, may be more easily modelled if the true parameter variations and time scale are used. The lumping of parameters, therefore, lends itself more successfully to the prediction of deformation of different geometric designs, once the firing schedule has been decided upon and the model parameters have been determined.

The simplicity of the models is highly evident throughout and is particularly apparent in the meshing of the networks. As bodies deform the TLM meshes retain their original configuration since only the loading, modelled by the pulses, is deformation dependent and therefore re-meshing is elegantly avoided.

Although, thus far, the elastic model has been applied only to cantilever beams in order to obtain steady state elastic solutions it is anticipated that the model may be equally applied to more complex structures, such as the hoop shapes and the mushroom shell, as it adopts a similar loading approach to that

of the viscous models. Due to the simplicity of the loading it is not unreasonable to expect that the elastic TLM model would significantly facilitate the calculation of these solutions when compared with the lengthy analytical approach detailed in the previous chapter.

### 7.3 General Applicability of Models

All of the models that have been developed assume either pure traction or pure bending, that is deformation occurs in one plane so that torque or in-plane shearing effects are neglected. Deformation occurring in more than one plane requires a fuller treatment that considers stresses acting in the remaining dimensions. This leads to the incorporation of the full Navier-Stokes equations which relate the velocity components in each of the three dimensions thus demanding the coupling of three velocity meshes. Clearly, in all of the examples considered and in each of the simulated results the present models have proved to yield adequate results, as the deformation in each case is predominantly in one plane due to the manner of support.

Other features of the bodies considered include geometric symmetry and constant viscosity throughout the body, which eliminate considerations of lateral yielding. Under gravity each body is subjected to a single force which, in the case of a vertical column, acts so as to produce deformation in a vertical direction. A horizontal force acting on the column, as depicted in figure 7.1, will yield deformation similar to that of a cantilever subject to a vertical force of the same magnitude and the component of the force acting on the column is therefore  $F\sin\theta$ , where  $\theta$  denotes the angle with respect to the horizontal. When this column is subject to gravity the total force on each element of the column is given by  $g\cos\theta + F\sin\theta$ .

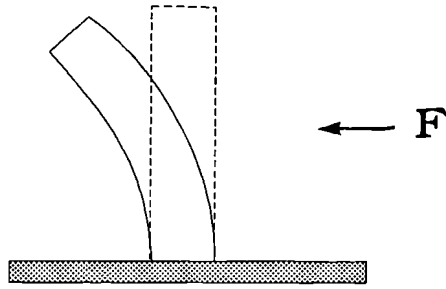


Figure 7.1 Vertical column deforming under the effect of a horizontal force.

Lateral yielding due to a variation in viscosity or an asymmetric geometry may produce an effect similar to that of figure 7.1, so that the horizontal force  $F$  arising from the asymmetry must be determined in either case. The present models do not account for such significant asymmetric effects and therefore assume symmetry through the centre of gravity of each body so that bodies standing upright are always assumed to be geometrically stable. In the sanitary ware industry although articles are asymmetric significant in plane shearing, perhaps due to a considerable variation in viscosity and resulting in geometrically unstable bodies, is undesirable and therefore avoided so that the modelling of such effects is not required.

An effect more predominant in the ware producing asymmetry is surface rippling. Rippled surfaces may arise as a result of a slight variation in the viscosity, probably due to variations in the temperature profile, and may be modelled by the implementation of a two dimensional mesh. For example, consider a 2-d plate supported along its width as in figure 7.2.

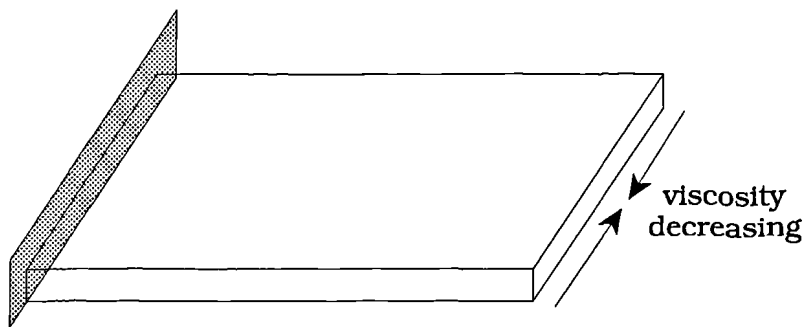


Figure 7.2 Plate supported as cantilever with varying viscosity.

Here the viscosity decreases towards the centre of the plate so that the resultant deformation yields a central dip in the plate. The simple two dimensional model that neglects deformation parallel to the width may be used to approximately model this effect provided that the viscosity variation is slight. In this approach each strip of the plate deforms as a cantilever beam of constant viscosity along its length, the central beam being of lowest viscosity. Clearly, the central beam will yield the most deformation thereby producing the central dip. However, although the variation in viscosity affects the magnitude of deformation experienced by each strip of the plate, the bending in the direction of the plate parallel to the width is unaccounted for so that strips are displaced vertically with respect to one another, as shown in figure 7.3.

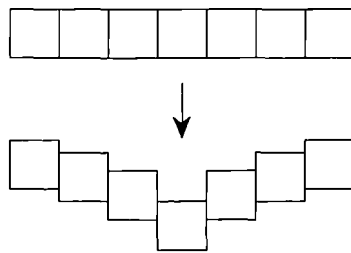


Figure 7.3 Cross-section of plate parallel to the width before and after deformation.

In a full dimensional model bending in the direction parallel to the width would be accounted for, yielding the deformation depicted in figure 7.4.

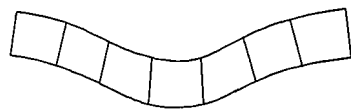


Figure 7.4 True bending of plate cross-section.

Clearly, provided that the variation in viscosity is slight the deformation of figure 7.3 may be assumed to be in close approximation to that of figure 7.4.

A viscosity variation in the height of the plate, however, cannot be represented by the present approach as it is assumed that each vertical section remains plane as the plate bends and so the area moment of inertia of each element takes into account the total height of the plate.

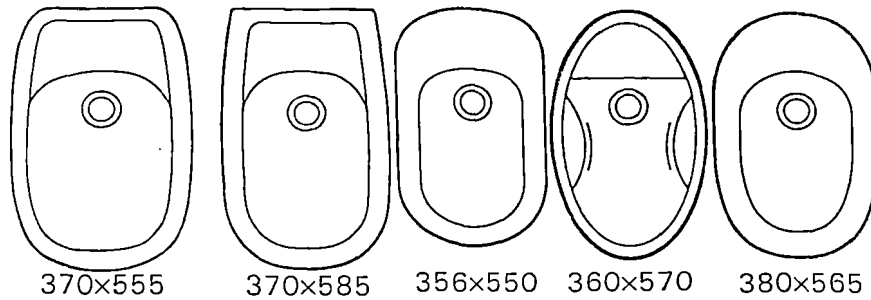


Figure 7.5 A variety of bidet designs.

The consideration of undulating surfaces leads to the consideration of geometrically asymmetric surfaces in bodies such as toilet pedestals, bidets and wash basins which, although they have a plane of symmetry, do not exhibit rotational symmetry. Figure 7.5 illustrates a variety of bidet designs, each having only one plane of symmetry. Each basin is slightly oval shaped so that every segment of a particular bidet, stretching from the base to the top of the article, is inclined at a slightly different angle to the vertical. Therefore, the body exhibits a variation in curvature both radially and along the length of each segment. However, if the variation in radial curvature is very gradual and less defined than the variation along a segment then again the basic two dimensional equation, considering deformation in only one direction, may be considered to give an accurate representation of the deformation.

The three dimensional bodies considered so far have single walls and the models therefore may be applied to a variety of ware including vases, lamp bases and bowls. Close inspection of sanitary ware pedestals and wash basins, however, reveals that these bodies are double walled, as depicted in figure 7.6.

It is anticipated, therefore, that hoop-shaped shell structures may be required for the representation of such geometries.

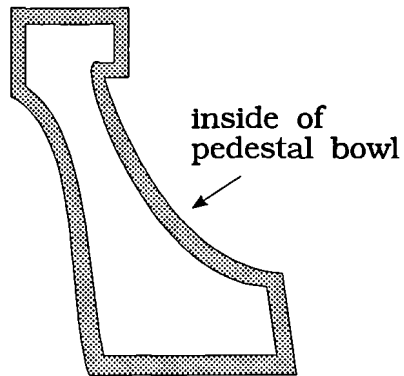


Figure 7.6 Cross-section of the front part of a pedestal.

#### 7.4 Conclusion

Models of deformation for viscous, elastic and viscoelastic behaviour have been developed using the transmission line modelling technique. The models represent elongation and bending under the effect of gravity and in the latter case have been validated theoretically. Three-component viscoelastic models simulating the behaviour during firing of a range of vitreous china testpieces have been shown to yield good experimental agreement. The application of the models to the sanitary ware industry has also been discussed.

## Appendix I: Thevenin's Theorem Applied to a Node

The equivalent electrical circuit for an n-dimensional node consisting of both resistors and transmission lines is depicted in figure I.1, where the subscript m denotes the number of branches such that  $m=2n$ . The stub transmission line is represented by the branch having subscript 0, the resistor  $R_0$  only being included for completeness. Each branch terminates in an open circuit so that the incident voltage pulses are perfectly reflected. The resulting superposition of pulses is represented at the end of each branch by a voltage source.

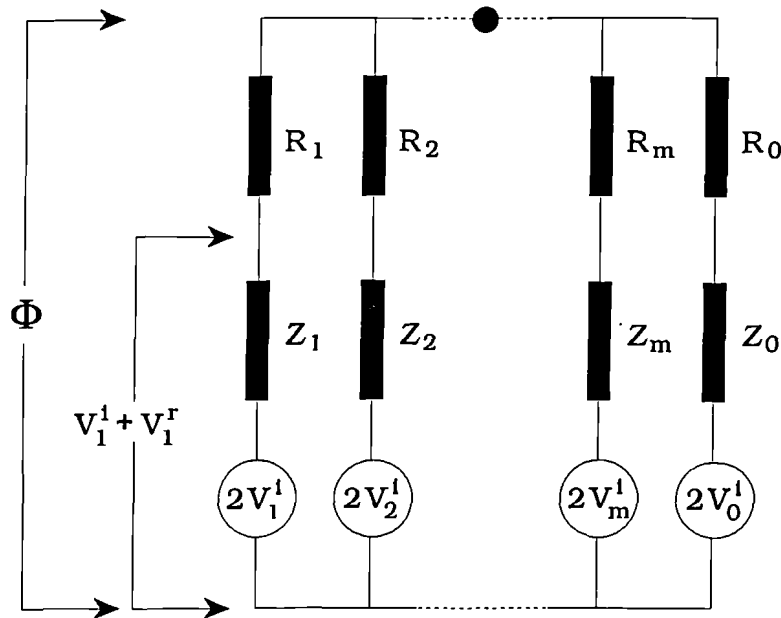


Figure I.1 Equivalent electrical circuit of an n-dimensional TLM node.

Kirchoff's Law states that the net current flow at the nodal junction is zero, yielding

$$\frac{2 V_0^i - \Phi}{R_0 + Z_0} + \frac{2 V_1^i - \Phi}{R_1 + Z_1} + \frac{2 V_2^i - \Phi}{R_2 + Z_2} + \dots + \frac{2 V_m^i - \Phi}{R_m + Z_m} = 0 \quad (I.1).$$

Rearranging (I.1) gives

$$\Phi \left( \sum_{l=0}^m \frac{1}{R_1 + Z_1} \right) = \left( \sum_{l=0}^m \frac{2V_1^i}{(R_1 + Z_1)} \right)$$

and solving for  $\Phi$  leads to

$$\Phi = \left( \sum_{l=0}^{2n} \frac{2V_1^i}{(R_1 + Z_1)} \right) \frac{1}{Y} \quad \text{where, } Y = \left( \sum_{l=0}^{2n} \frac{1}{R_1 + Z_1} \right) \quad (\text{I.2}).$$

The expression for the reflected pulse values may be determined by consideration of current flow along branch 1. The potential drop across the resistor is given by  $\Phi - (V_1^i + V_1^r)$  and the difference in potential across the transmission line is given by  $V_1^i + V_1^r - 2V_1^i$ . The current flow through the resistor must equal that through the transmission line, so that

$$\frac{\Phi - (V_1^i + V_1^r)}{R_1} = \frac{V_1^i + V_1^r - 2V_1^i}{Z_1} \quad (\text{I.3}).$$

Rearrangement of (I.3) yields the following general expression for the reflected pulses,

$$V_1^r = \frac{Z_1}{(R_1 + Z_1)} \Phi + \frac{(R_1 - Z_1)}{(R_1 + Z_1)} V_1^i \quad (\text{I.4}).$$